UNIVERSITY OF CALIFORNIA,
IRVINE

Structural and Biophysical Analysis of Post-Translationally Modified γ-Crystallin

DISSERTATION

submitted in partial satisfaction of the requirements
for the degree of

DOCTOR OF PHILOSOPHY

in Chemistry

by

Brenna Norton-Baker

Dissertation Committee:
Professor Rachel W. Martin, Chair
Professor Suzanne A. Blum
Assistant Professor Elizabeth N. Bess

2022

DEDICATION

To my family, for their love and support.

TABLE OF CONTENTS

LIST OF FIGURES

LIST OF TABLES

ACKNOWLEDGMENTS

I would first like to thank Professor Rachel Martin, for admitting me as a latecomer into her group and supporting me in many ways, including a year fellowship in Germany. Also for giving me the freedom to pursue many interesting projects and always offering invaluable insight and mentorship.

Many thanks to all the members of the Martin lab, especially:

Kyle - for the patience to answer many questions and the support getting started in lab

Marc and Jan - for much-needed advice when things didn't make sense

Ashley - for the exceptional work you accomplished and often keeping me on track when I tried to do too many things

Megan - for being not only a hardworking and supportive labmate, but also a great friend, with all the coffee, lunches, hikes, and happy hours.

To my colleagues and friends in Hamburg, thank you, especially to Pedram Mehrabi, Lindsey Bultema, and Eike Schulz.

For managing excellent instruments and providing constant advice, thank you to Ben Katz and Dmitry Fishman.

This research was supported by NSF GRFP, the Fulbright Program in partnership with the Germanistic Society of America, the UCI Graduate LEAD fellowship, and NIH grants EY021514, 2R01EY021514, and S10OD021594.

Chapter 2 adapted with permission from: Brenna Norton-Baker, Pedram Mehrabi, Ashley O. Kwok, Kyle W. Roskamp, Megan A. Rocha, Marc A. Sprague-Piercy, David von Stetten, R.J. Dwayne Miller, and Rachel W. Martin* "Deamidation of the human eye lens protein γS-crystallin accelerates oxidative aging" *Structure* **2022**, *in press.*

Chapter 3 adapted with permission from: Brenna Norton-Baker†, Megan A. Rocha†, (†contributed equally) Jessica Granger-Jones, Dmitry Fishman, and Rachel W. Martin* "Human γS-crystallin resists unfolding despite extensive chemical modification from exposure to ionizing radiation" *J. Phys. Chem. B* **2022**, 126, 679–690.

Chapter 4 adapted with permission from: Brenna Norton-Baker, Pedram Mehrabi, Juliane Boger, Robert Schönherr, David von Stetten, Hendrik Schikora, Ashley O. Kwok, Rachel W. Martin, R.J. Dwayne Miller, Lars Redecke and Eike C. Schulz* "A simple vapor diffusion method enables protein crystallization inside the HARE serial crystallography chip" *Acta Crystallographica Section D* **2021**, D77, 820–834.

VITA

Brenna Norton-Baker

EDUCATION

Doctor of Philosophy in Chemistry **2022**
University of California, Irvine *Irvine, CA*

Bachelor of Science in Biochemistry **2015**
College of Charleston *Charleston, SC*

Bachelor of Arts in Chemistry **2015**
College of Charleston *Charleston, SC*

RESEARCH EXPERIENCE

Graduate Research Assistant **2016–2022**
University of California, Irvine *Irvine, CA*

Undergraduate Research Assistant **2012–2015**
College of Charleston *Charleston, SC*

TEACHING EXPERIENCE

Teaching Assistant **2016–2017**
University of California, Irvine *Irvine, CA*

PUBLICATIONS

13. **Brenna Norton-Baker**, Pedram Mehrabi, Ashley O. Kwok, Kyle W. Roskamp, Megan A. Rocha, Marc A. Sprague-Piercy, David von Stetten, R.J. Dwayne Miller, and Rachel W. Martin* "Deamidation of the human eye lens protein γS-crystallin accelerates oxidative aging" *Structure* **2022**, *in press.*

12. Jessica I. Kelz, Gemma R. Takahashi, Fatemeh Safizadeh, Vesta Farahmand, Marquise G. Crosby, Jose L. Uribe, Suhn H. Kim, Marc A. Sprague-Piercy, Elizabeth M. Diessner, **Brenna Norton-Baker**, Steven M. Damo, Rachel W. Martin* "Active learning module for protein structure analysis using protein structure prediction of uncharacterized, research-relevant enzymes" *The Biophysicist* **2022**, *in press.*

11. **Brenna Norton-Baker**†, Megan A. Rocha†, (†contributed equally) Jessica Granger-Jones, Dmitry Fishman, and Rachel W. Martin* "Human γS-crystallin resists unfolding despite extensive chemical modification from exposure to ionizing radiation" *J. Phys. Chem.*

B **2022**, 126, 679–690.

10. Noah J. Stanton, Rachelle Ihly, **Brenna Norton-Baker**, Andrew J. Ferguson, and Jeffrey L. Blackburn* "Solution-phase p-type doping of highly enriched semiconducting single-walled carbon nanotubes for thermoelectric thin films" *Appl. Phys. Lett.* **2021**, 199, 023302.

9. Eric O. Potma, David Knez, Yong Chen, Yulia Davydova, Amanda Durkin, Alexander Fast, Mihaela Balu, **Brenna Norton-Baker**, Rachel W. Martin, Tommaso Baldacchini, and Dmitry A. Fishman* "Rapid chemically selective 3D imaging in the mid-infrared" *Optica* **2021**, 7, 995–1002.

8. **Brenna Norton-Baker**, Pedram Mehrabi, Juliane Boger, Robert Schönherr, David von Stetten, Hendrik Schikora, Ashley O. Kwok, Rachel W. Martin, R.J. Dwayne Miller, Lars Redecke and Eike C. Schulz* "A simple vapor diffusion method enables protein crystallization inside the HARE serial crystallography chip" *Acta Crystallographica Section D* **2021**, D77, 820–834.

7. Nadide Altincekic, Sophie Marianne Korn, Nusrat Shahin Qureshi, Marie Dujardin, Martí Ninot-Pedrosa, [*et al.*, including **Brenna Norton-Baker**], Martin Hengesbach* and Andreas Schlundt* "Large-scale recombinant production of the SARS-CoV-2 proteome for high-throughput and structural biology applications" *Front. Mol. Biosci.* **2021**, 8, 653148.

6. Sebastian Günther, Patrick Y. A. Reinke, [*et al.*,, including **Brenna Norton-Baker**], and Alke Meents* "X-ray screening identifies active site and allosteric inhibitors of SARS-CoV-2 main protease" *Science* **2021**, 372, 642–646.

5. Mehran J. Umerani, Preeta Pratakshya, Atrouli Chatterjee, Juana A. Cerna Sanchez, Ho Shin Kim, Gregor Ilc, Matic Kovačič, Christophe Magnan, Benedetta Marmiroli, Barbara Sartori, Albert L. Kwansa, Helen Orins, Andrew W. Bartlett, Erica M. Leung, Zhijing Feng, Kyle L. Naughton, **Brenna Norton-Baker**, Long Phan, James Long, Alex Allevato, Jessica E. Leal-Cruz, Qiyin Lin, Pierre Baldi, Sigrid Bernstorff, Janez Plavec, Yaroslava G. Yingling, and Alon A. Gorodetsky* "Structure, self-assembly, and properties of a truncated reflectin variant" *PNAS* **2020**, 117, 32891–32901.

4. Kyle W. Roskamp, Sana Azim, Günther Kassier, **Brenna Norton-Baker**, Marc A. Sprague-Piercy, R. J. Dwyane Miller, and Rachel W. Martin* "Human γS-crystallin copper binding helps buffer against aggregation caused by oxidative damage" *Biochemistry* **2020**, 59, 2371–2385.

3. Jeffrey L. Blackburn,* Stephen D. Kang, Michael J. Roos, **Brenna Norton-Baker**, Elisa M. Miller, and Andrew J. Ferguson* "Intrinsic and extrinsically limited thermoelectric transport within semiconducting single-walled carbon nanotube networks" *Advanced Electronic Materials* **2019**, 1800910.

2. Atrouli Chatterjee, **Brenna Norton-Baker**, Laura E. Bagge, Priyam Patel, and Alon A. Gorodetsky* "An introduction to color-changing systems from the cephalopod protein

reflectin" *Bioinspiration & Biomimetics* **2018**, 13, 045001.

1. **Brenna Norton-Baker**, Rachelle Ihly, Isaac E. Gould, Azure D. Avery, Zbyslaw R. Owczarczyk, Andrew J. Ferguson,* and Jeffrey L. Blackburn* "Polymer-free carbon nanotube thermoelectrics with improved charge carrier transport and power factor" *ACS Energy Letters* **2016**, 1, 1212–1220.

PRESENTATIONS

"Accelerated oxidative aging in deamidated variants of the human eye lens protein γS-crystallin" *Biophysical Society Annual Meeting* (San Francisco, CA), Oral presentation, February 2022

"Protein crystallization inside a serial crystallography chip" *Chemistry Seminar Series* (College of Charleston, SC), Invited oral presentation, September 2021

"Protein crystallization inside the HARE serial crystallography chip" *American Crystallographic Association Meeting* (Virtual), Poster presentation, August 2021

"Effects of Deamidation on Human Eye Lens Protein, γS-crystallin" *Synthetic and Chemical Biology Club* (UC Irvine), Oral presentation, March 2021

"Crystal Structures of Human γS-crystallin and Deamidated Mutants" *Crystallin Club* (Virtual), Oral presentation, February 2021

"Introduction of FT-IR and ^{19}FNMR probes in proteins via S_NAr" *Southeastern Regional Meeting of the American Chemical Society* (Nashville, TN), Oral presentation, October 2014

"Synthesis and biological evaluation of a series of potential anticancer phthalazinone agents designed utilizing a novel 2D-QSAR model" *Southeastern Regional Meeting of the American Chemical Society* (Atlanta, GA), Oral presentation, November 2013

"Design and synthesis of dual active derivatives of novel antibiotic Cytosporone E" *Southeastern Regional Meeting of the American Chemical Society* (Raleigh, NC), Poster presentation, November 2012

ABSTRACT OF THE DISSERTATION

Structural and Biophysical Analysis of Post-Translationally Modified γ-Crystallin

By

Brenna Norton-Baker

Doctor of Philosophy in Chemistry

University of California, Irvine, 2022

Professor Rachel W. Martin, Chair

Crystallins are structural proteins that serve as a medium for lens refraction to aid in the formation of vision. These highly soluble and stable proteins persist for decades without aggregation. Over the course of aging and exposure to degrading agents, such as reactive oxygen species, ultraviolet light, metal ions, or ionizing radiation, the eye lens crystallins accumulate post-translational modifications (PTMs) that can result in a loss of structural stability and thereby aggregation. These aggregates eventually form light-scattering masses and a diseased state of the eye lens known as cataract. Cataract is the leading cause of blindness in the world with millions affected every year. My research aims to evaluate the effects of PTMs on the structure and aggregation propensity of a specific human crystallin, γS-crystallin (γS). Two of the most common PTMs in aged and cataractous lenses are deamidation and oxidation. A series of deamidated variants of γS were studied via X-ray crystallography and biophysical characterization, revealing that the overall fold of γS is maintained among variants but these variants are structurally destabilized and more prone to disulfide bond formation. Additionally, the chemical modifications and stability of γS after exposure to ionizing radiation were evaluated. After high doses of γ radiation, γS accumulated a large number of modifications but largely resists unfolding. Both of these studies demonstrate the resilience of γS in spite of significant deamidation and oxidation modification, an adaptation advantageous for a long-lived protein. Lastly, a novel method of

protein crystallization within the wells of a serial crystallography chip was developed. This technique lowers samples consumption and physical handling of potentially delicate crystals, expanding the scope of systems available to study via serial and time-resolved crystallography. A novel structure of a γS deamidation variant was solved via serial crystallography on microcrystals grown in-chip.

Chapter 1

Introduction

1.1 Crystallins: long-lived eye lens proteins

1.1.1 The eye lens

The human eye lens is a transparent organ devoid of nerves and blood vessels, making it a unique tissue in the human body. A disk-shaped encapsulated structure that lies behind the iris, the eye lens serves to help refract light, forming a clear image upon the retina (Figure 1.1A). The lens changes shape through the contraction of the ciliary muscles in a process known as accommodation, which allows for the adjustment of focal length [1]. Vertebrate eye lens development begins in the fourth week of gestation, as the surface ectoderm over the optic vesicle thickens, eventually invaginating to form the lens pit [2]. After closure to form the lens vesicle, cellular differentiation begins with the cells lining the posterior wall rapidly elongating to form the initial lens fiber cells. These cells elongate up to several hundred times and begin to express significant amounts of highly refractive proteins known as crystallins, eventually reaching up to 400 mg/mL [3]. Secondary lens fiber cells form throughout the

human lifetime from the lens epithelial cells, layering onto older fiber cells. The older fiber cells are pushed to the nucleus of the lens and, compressed by the new growth, the nuclear lens cells lose water and refractive index is increased. A gradient of refractive index in the lens, higher in the central layers to lower towards the cortex, reduces optical aberrations [4]. Lens transparency is enabled by several factors. As the lens fiber cells mature, cellular organelles are lost via targeted destruction involving a multitude of degradative pathways and enzymes, a process currently still under investigation [5]. Additionally, light scattering is reduced by ordered arrangement of the fiber cells as well as the crystallin proteins within the cells. Upon cross sectioning, the fiber cells show a hexagonal packing pattern [2] and crystallin proteins have been demonstrated to have a short-range ordered spatial arrangement [6].

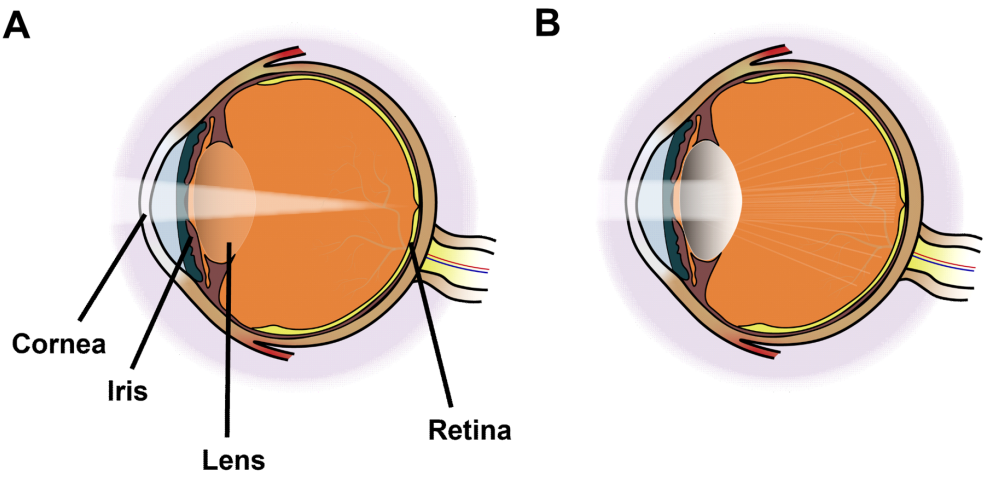

Figure 1.1: Schematic representation of the human eye with (A) normal lens and (B) cataract lens.

The lens undergoes significant changes with aging. The lens becomes stiffer and the power to accommodate decreases, a condition known as presbyopia [7]. Additionally, crystallin proteins can begin to degrade. Due to the loss of cellular machinery, the lens fiber cells are metabolically inert and protein turnover is minimal [8]. The exchange of ions and small metabolites may still occur through the complex system of gap junctions between cells [9]. As proteins cannot be recycled, the lens nucleus of an adult contains protein synthesized in

embryonic development. Over time, modifications to the crystallins accumulate and eventually lead to the formation of light-scattering aggregates [10]. This opacification of the lens may eventually lead to cataract blindness (Figure 1.1B), the leading cause of blindness worldwide [11].

1.1.2 Crystallin superfamilies: α and $\beta\gamma$

The eye lens crystallins can be divided into two structurally and evolutionarily distinct superfamilies: the α- and $\beta\gamma$-crystallins. The α-crystallins serve as a major refractive element in the lens as well as holdase chaperones. They function to bind, but not refold, damaged proteins in order to maintain solubility by suppressing non-specific protein aggregation [12]. α-crystallins are thought to mainly target the $\beta\gamma$-crystallins, with water-insoluble fractions of aged lenses showing the major component to be α-crystallin and γS- and γD-crystallin [13]. Two α-crystallins are produced in the human lens: αA and αB. They are present in a molar ratio of $\sim$3:1 of αA to αB and together comprise approximately 40% of the human lens protein [14]. αB is also found outside the lens and is overexpressed in many neurological diseases, including Alzheimer's and Parkinson's [15]. Both αA and αB can form dimers (both hetero- and homodimers) that further serve to build heterogenous multimeric assemblies, reaching up to 50 subunits [15]. As in other small heat-shock proteins, the structure of α-crystallin contains the 'α-crystallin domain' that is rich in β-sheets, while the N- and C-terminal regions are less structured [16]. Polydispersity appears to be an innate property of the lens α-crystallins and likely contributes to lens function. The formation of heterogenous oligomers may aid in maintaining the transparent state of the lens by deterring crystallization as well as binding a diverse set of client proteins with varying sizes and properties [12].

$\beta\gamma$-crystallins are considered structural proteins with high solubility and stability [17]. They increase the refractive power of the lens and are able to maintain lens transparency for

decades. Both the β- and γ-crystallins are composed of domains containing a double Greek key motif, which confers high thermodynamic and kinetic stability [18]. Human lens β-crystallins can be divided into two groups based on their net charge: the acidic β-crystallins are βA1, βA2, βA3, and βA4 and the basic β-crystallins are βB1, βB2, and βB3 [19]. The β-crystallins have long interdomain linker regions which enable oliogomerization. They have been observed to form domain-swapped dimers and higher molecular weight hetero- and homooligomers up to 200 kDa [19, 20]. γ-crystallins, however, are typically monomeric [21]. Most mammalian genomes encode for eight γ-crystallins: γA—F, γS, and γN; however, γE, γF, and γN commonly appear as pseudogenes and are not expressed [22]. The most abundantly produced γ-crystallins in the human lens are γC, γD, and γS [4].

The focus of this research is on γS-crystallin, which is the exception among highly expressed γ-crystallins in the human lens as it is synthesized primarily postnatally in the cortex, while γC and γD are found predominantly in the nucleus and are mostly expressed before birth [4]. As with other γ-crystallins, its two domains are structurally very similar, forming a highly symmetric protein. However, γS-crystallin differs in that it contains an extra N-terminal tail and a slightly longer interdomain linker. γS has been linked to heritable cataracts with single site variants including V42M, G57W, D26G, S39C, and G18V [4]. Subtle changes in structure have been demonstrated to significantly affect stability and aggregation as well as α-crystallin chaperone activity [23, 24].

1.1.3 Crystallin aggregation

Many factors have been linked to an increased propensity for aggregation in crystallins, from congenital site mutations to post-translational modifications (PTMs) resultant from age and exposure to damaging elements. Due to the long-lived nature of these proteins, even small changes that appear to minorly perturb protein structural stability, dynamics, or

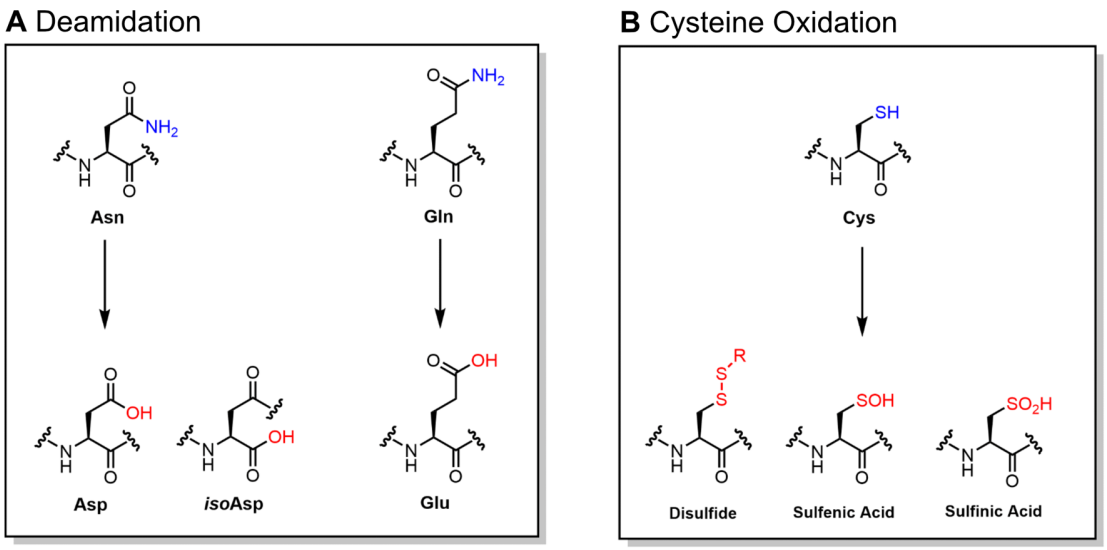

Figure 1.2: Common post-translational modifications reported in crystallins, deamidation (A) and oxidation of cysteine (B).

protein-protein interactions may contribute to cataract formation. Of the genetic mutations associated with hereditary cataract in γ-crystallins, a theme emerges as reviewed by Vendra *et al.* [4]. Many of the single site mutations appear not to alter the overall protein fold, but disrupt surface properties and protein-protein interactions. Mutations of surface arginines (7 out of the 30 reported congenital cataract variants in γ-crystallins) exemplify this trend, as very little change is observed in the tertiary structure of the protein; however, the onset of cataract, including crystal-forming cataract, is observed with reported changes in protein surface properties.

Structural changes from PTMs are the more common route to cataract [25]. A wide variety of PTMs have been reported in aged and catartous lenses including deamidation, oxidation, glycation, and truncation [26]. Two commonly reported PTMs in crystallins, and the focus of this thesis, are deamidation and oxidation. Deamidation is a stochastic process that converts asparagine to aspartic acid or *iso*aspartic acid and glutamine to glutamic acid or, less commonly, *iso*glutamic acid (Figure 1.2A) [27–30]. Additionally, deamidation may also lead to racemization [31, 32]. Oxidation can occur on many residues, with methionine, cysteine, tryptophan, and histidine observed to be particularly vulnerable [10, 33]. This thesis focuses

on cysteine oxidation, which can result in the formation of a disulfide bond between two cysteines as well as sulfenic and sulfinic acid derivatives (Figure 1.2B) [34]. Cysteine oxidation is especially significant in the study of γS-crystallin, with its higher number of solvent-exposed cysteines compared to other crystallins, predisposing it to oxidative modification [35].

Overall, this thesis demonstrates the use of biophysical characterization of proteins as well as protein X-ray crystallography to investigate the effects of PTMs on the structure and stability of γS-crystallin. Additionally, the development of a novel method of *in situ* protein crystallization is detailed, which expands the toolkit available to crystallographers for the collection of serial datasets on challenging crystallization targets, such as the highly soluble and crystallization-recalcitrant eye lens proteins.

Chapter 2

Deamidation of the human eye lens protein γS-crystallin accelerates oxidative aging

2.1 Introduction

The eye lens is a unique environment in the human body, hosting some of the most long-lived proteins at extremely high concentrations [36]. In order to establish and maintain transparency, the lens fiber cells lose much of their cellular machinery during early development via a combination of autophagy and lipase-mediated destruction of organelles [37, 38]. In adulthood, the lens undergoes very little protein turnover [8]. Crystallins are the predominant protein species in the lens, comprising over 90% of dry mass and reaching concentrations above 400 mg/mL [4, 39, 40]. Crystallins were originally characterized by their transparency and presence in the "crystalline lens" and are divided into two superfamilies, α-crystallins and $\beta\gamma$-crystallins [41]. The α-crystallins are related to small heat shock proteins and serve

as molecular chaperones that offset aggregation [15]. The $\beta\gamma$-crystallins are considered structural proteins; they form short-range ordered arrangements and increase the refractive index of the lens, focusing light onto the retina [17]. In order to maintain lens transparency, crystallins need to remain stable over the entire human lifetime. During aging, however, modifications accumulate in the eye lens proteins from exposure to reactive oxygen species, ultraviolet light, and lens contamination with non-native molecules and metal ions [26]. Due to the presumed loss of structural stability concomitant with these modifications, eye lens proteins aggregate and form large, light-scattering masses in the lens, leading to cataract. Cataract is a leading cause of blindness worldwide, especially in middle- and low-income countries, where surgical intervention is often less accessible [11, 42].

Post-translational modifications (PTMs) of crystallins in the form of deamidation, oxidation, methylation, and truncation have all been observed in aged lenses, with deamidation reported to be one of the most prevalent [43–46]. Deamidation replaces an amide with a carboxylic acid, transforming glutamine or asparagine to glutamic acid/*iso*-glutamic acid or aspartic acid/*iso*-aspartic acid, respectively, with the possibility of racemization at each site [27, 28]. To date, studies have focused on the Asp and Glu products, rather than any isomers or epimers. Although these additional products have been detected in long-lived proteins in the lens and brain [30–32, 47], detection techniques are still under development and studies on these variants are impeded due to the difficulty of producing proteins with these modifications. Even for surface-exposed residues, deamidation can lead to changes in conformational dynamics and an increase in aggregation propensity [48–54]. Additionally, PTMs appear to be interdependent; Vetter *et al.* found that increased deamidation results in an increase in aggregation induced by oxidation [54]. It is hypothesized that an increase in conformational flexibility in structurally destabilized proteins can lead to solvent exposure of key modifiable residues. Deamidation and disulfide crosslinking are both reported with higher prevalence in cataractous lenses than normal lenses [46, 55–58].

Deamidation has been studied in both β- and γ-crystallins. In β-crystallins, deamidation appeared to alter the dimer structure and led to a less compact fold in βB1 and βA3 [50, 59]. Similar results were found with βB2, with the dimer destabilized by deamidation [60]. In the γ-crystallins, γD was destabilized by deamidations at the interface between the two domains of the monomer, although the prevalence of naturally-occurring deamidation at these buried sites *in vivo* is not clear [48, 55, 61]. However, a number of single-site deamidation variants of surface asparagines on γD did not show any significant changes in structure or stability [62]. In contrast, deamidated variants of γS have been reported to have attractive protein-protein interactions, leading to increased propensity for dimerization and aggregation [49, 51, 52, 54]. Although Vetter *et al.* and Pande *et al.* investigated 3- and 4-site deamidation variants [51, 54], respectively, most of the previous studies have focused on crystallin variants with only one or two deamidation sites. This study explores the effects of progressive accumulation of deamidations, evaluating both the moderate deamidation that likely occurs in highly aged lenses as well as more extreme deamidation as a means of assessing the tolerance of γS to major surface charge modification.

Due to the long-lived nature of the crystallins, the lens requires mechanisms of protection and repair to cope with decades of stress. Anti-oxidant compounds, notably glutathione, play vital roles in balancing the redox state of the lens [1]. Crystallin proteins themselves also display adaptations that aid in longevity. Although they have historically been considered purely structural proteins, it has recently been suggested that members of the $\beta\gamma$-crystallin family have chemical functionality in metal binding and disulfide exchange in the lens [35, 63]. In particular, γS-crystallin (Figure 2.1A), with its high cysteine content compared to other γ-crystallins, has been proposed to fulfill an oxidoreductase-like role [35]. γS-crystallin contains a cysteine tetrad (C23, C25, C27, C83) in its N-terminal domain (Figure 2.1B), with C23, C25, and C27 exhibiting unusually high solvent exposure. Solvent-exposed cysteines would appear to be disadvantageous for a long-lived protein. Indeed, the dimer of γS-crystallin, formed by the intermolecular disulfide linkage of C25 and C25 of

two γS-crystallin monomers, is less stable and more aggregation-prone than the monomer [64]. The functional advantage of these solvent-accessible cysteines in γS-crystallin is still under investigation, although they have been demonstrated to play a critical role in metal interactions. A number of divalent cations, including Zn^{2+}, Ni^{2+}, Co^{2+} and Cu^{2+}, cause aggregation of γS, and the mutation of C23/25/27 dramatically affects this metal-induced aggregation. For Zn^{2+}, Ni^{2+}, Co^{2+}, the mutation of these cysteines to serines prevented aggregation [65]. However, for Cu^{2+}, the removal of C23/25/27 increased the susceptibility of γS to Cu^{2+}-induced oxidation and aggregation, suggesting that these residues buffer against Cu^{2+}-induced oxidative damage [35, 65]. Similarly, the cysteines of γD-crystallin have also been implicated in metal-induced aggregation [66, 67]. Furthermore, similar solvent-exposed cysteines in γD-crystallin have been shown to undergo dynamic disulfide exchange, transferring disulfide bonds in an oxidoreductase-like role [63].

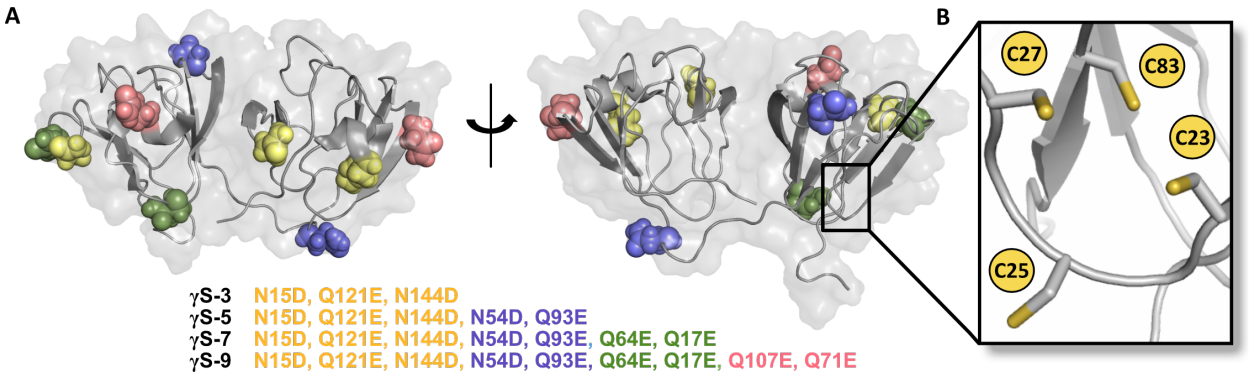

Figure 2.1: (A) Sites of mutagenesis in the 3-site (γS-3, yellow), 5-site (γS-5, blue), 7-site (γS-7, green), and 9-site deamidation variants (γS-9, pink). (Structure from PDB: 2M3T) (B) Magnified view of the cysteine tetrad located in the N-terminal domain.

In this study, we investigated the relationship between deamidation and disulfide bond formation in γS-crystallin. Crystallins have been shown to collect multiple PTMs; in order to mimic this natural aging process on a compressed timescale, we expressed four deamidated γS-crystallin variants that emulate moderate-to-extreme examples of deamidation, with 3, 5, 7, and 9 sites of deamidation at surface residues. (Figure 2.1A). With each addition of more

deamidated sites, the variants demonstrated lower structural stability. Furthermore, the deamidated variants showed an increased aggregation propensity compared to wild-type γS-crystallin (γS-wt). Estimation of the second osmotic virial coefficient from small angle X-ray scattering data showed an increase in repulsive interaction forces with increasing deamidation, suggesting aggregation propensity is governed by competing effects from hydrophobic exposure during unfolding and protein-protein interactions. Crystal structures were determined for the full-length, monomeric γS-wt as well as the deamidated variants at different time points in sample age. Although the deamidation mutations did not cause significant changes to the overall protein fold, these structures revealed that increased deamidation does lead to an increased propensity for disulfide bond formation, indicating accelerated oxidative aging compared to the wild type. An intramolecular disulfide bond between C23 and C27 formed first, with a second dimerizing bond at C25 occurring in increasingly aged samples. Additionally, the structural changes after sample aging give evidence of the role of γS-crystallin as a mediator of oxidation in the eye lens, exchanging deleterious cross-linking disulfide bonds for stable internal disulfide bonds.

2.2 Materials and methods

2.2.1 Expression and purification

Sites for deamidation were selected based on mass spectrometry data reported by Lapko *et al.* [57], prioritizing sites with the highest reported incidence of deamidation and those with the highest calculated solvent-accessible surface area. Progressively more sites were mutated, starting with N15D, Q121E, N144D (3-site variant, γS-3), then N54D and Q93E (5-site variant, γS-5), then Q64E and Q17E (7-site variant, γS-7), and finally Q107E and Q71E (9-site variant, γS-9). Site-specific mutagenesis PCR was used to create the deamidated variants

from the wild-type construct with an N-terminal 6x-His tag and a tobacco etch virus (TEV) protease cleavage sequence. The oligonucleotides used in the mutagenesis are listed in Table A.1. Expression and purification of wild-type γS-crystallin (γS-wt) and the deamidated variants was performed as described previously [68]. The constructs in pET28a(+) vector were used to transform *Escherichia coli* Rosetta (DE3) cells. Overexpression was achieved using Studier's autoinduction method (ZYM-5052 media) for 1 h at 37 °C followed by 20-24 h at 25 °C incubation [69]. The cells were lysed by sonication and the supernatant loaded onto a Ni-NTA column. An imidazole gradient was used to elute the tagged protein, then TEV protease (produced in-house) was added to cleave the 6x-His tag. Reapplication to the Ni-NTA column separated the TEV protease. The samples were reduced with 10 mM dithiothreitol (DTT), concentrated, and loaded on to a HiLoad 16/600 Superdex 75 pg column. The purified proteins were lyophilized for storage at -80 ℃.

2.2.2 Differential scanning fluorimetry (DSF)

Differential scanning fluorimetry (DSF) analysis was performed in a Stratagene Mx3005P RT-PCR instrument (Agilent, Santa Clara, CA, USA) in thin-walled 96-well PCR plates with transparent Microseal B seals. The temperature ramp was between 25 ℃ and 94 ℃ with a 0.5 ℃ increase per cycle for 140 cycles and a cycle duration of 30 seconds. Midpoint of the unfolding temperatures (T_m) were calculated as described by Wright et al [70]. Each well contained 0.5 mg/ml protein and 2.5× SYPRO orange dye in 10 mM HEPES pH 7.0, 50 mM NaCl, 0.05% sodium azide.

2.2.3 Dynamic light scattering (DLS)

Thermally-induced aggregation was assessed with dynamic light scattering (DLS) using a Zetasizer Nano-ZS (Malvern Analytical, Malvern, United Kingdom). Protein concentration

was 1 mg/ml in 10 mM HEPES pH 7.0, 50 mM NaCl, 0.05% sodium azide. At each temperature, the sample was equilibrated for 120 seconds before the scattering measurements were performed in triplicate. Data was processed using the Zetasizer software. The autocorrelation function was used to derive the intensity of scattering as a function of particle size. A number distribution is then calculated to estimate the relative concentrations of particles of different sizes, accounting for their proportional light scattering. The reported apparent size is the number mean.

2.2.4 Small angle X-ray scattering (SAXS) data collection

Samples in 10 mM HEPES pH 7.0, 50 mM NaCl, 0.05% sodium azide, 2 mM DTT were concentrated to ∼40 mg/mL in 0.5 mL Amicon-Ultra centrifugal concentrators and the flow through used as a buffer blank. A dilution series was prepared and the concentrations measured in triplicate on a Thermo Scientific™ NanoDrop™ OneC Microvolume UV-Vis Spectrophotometer (Fisher Scientific, Waltham, MA, USA). Data were collected at the SIBYLS beamline (12.3.1) at the Advanced Light Source in Berkeley, California using the high throughput mail-in SAXS service [71]. The concentration series for each protein was collected in triplicate. For each sample, a dose series was collected with a total exposure time of 10 s, framed at 0.3 s for a total for 33 frames. The sample oscillated during the exposure to reduce radiation damage. Data were collected using a PILATUS 2M detector. The monochromatic X-ray energy was 10 keV and detector distance was 2 m, resulting in scattering vectors, q, ranging from 0.0094 $Å^{-1}$ to 0.4354 $Å^{-1}$. Samples were at 20 °C during data collection. Data were initially processed as described [72]. Additional processing was performed using BioXTAS RAW [73].

2.2.5 Calculation of the second virial coefficient (A_2)

Static structure factor of a monodisperse solution at the origin S(c,0) related to the osmotic pressure Π is described by:

$$S(c,0) = \frac{RT}{M}\left(\frac{\partial \Pi}{\partial c}\right)^{-1}$$

R is the gas constant 8.31 J mol^{-1} K^{-1}. M is the molecular mass of the solute in g/mol. c is the concentration in g/mL. The osmotic pressure can be approximated by the series expansion:

$$\frac{\Pi}{cRT} = \frac{1}{M} + A_2 c + A_3 c^2 + ...$$

For weakly interacting molecules at relatively low concentrations, $2MA_2c << 1$, the structure factor at the origin can be expressed as:

$$S(c,0) = \frac{I(c,0)}{I(0,0)} = \frac{1}{1 + 2MA_2c + ...}$$

S(c,0) is evaluated by:

$$S(c,0) = \frac{\lim_{q\to 0} I(c,q)}{\lim_{c\to 0} I(c,0)}$$

The slope of the linear fit from following gives $2MA_2$:

$$\frac{1}{S(c,0)} = 1 + 2MA_2c$$

In an ideal solution, S(c,0) = 1. If A_2 is positive, the osmotic pressure is higher and the interactions are repulsive, leading to particles that are evenly distributed. If A_2 is negative, the osmotic pressure is lower and attractive interactions cause fluctuations in particle

distribution [74, 75].

2.2.6 Ellman's assay

The lyophilized powders for γS-wt and the deamidation variants were reconstituted from the same stock of buffer and aged at room temperature stored out of direct light. Prior to each measurement, samples were vortexed and an aliquot was diluted in 2% SDS, 100 mM TRIS pH 8.0 to reach a final protein concentration 0.125 mg/mL and 5,5-dithiobis(2-nitrobenzoic acid) (DTNB) was added to reach a final concentration of 0.1 mM. Absorbance measurements were collected in an Epoch™ Microplate Spectrophotometer (BioTek, Winooski, VT, USA) at 412 nm in a 96-well plate. Each sample was made in triplicate and measurements taken in 5-minute intervals over 2 hours. The maximum value was used to calculate the thiol content. An extinction coefficient of 12968 $M^{-1}cm^{-1}$ was calculated from the calibration curve in 2% SDS, 100 mM TRIS pH 8.0 buffer using DTT as the thiol source (Figure A.2) and used for all thiol concentration calculations.

2.2.7 Size-exclusion chromatography multi-angle light scattering (SEC-MALS)

SEC-MALS was performed on a Viskotek 305 TDA system (Malvern Analytical, Malvern, United Kingdom) equipped with a P2500 column. The running buffer used was 10 mM HEPES pH 7.0, 200 mM NaCl, 0.05% sodium azide.

2.2.8 Mass spectrometry

Proteins samples were denatured in 8 M urea, 1 M ammonium bicarbonate pH 8.0 for 1 h then iodoacetamide (IAM) was added to reach 50 mM. The reaction progressed at room temperature away from light for 2.5 h. DTT was added to reach 100 mM and incubated for 1 h. Mass spectra were collected on a Waters Xevo XS-QToF equipped with a phenyl column. Buffer A was 0.1% formic acid in water. Buffer B was 100% acetonitrile. For the protein intact mass spectra, the flow rate was 0.2 mL/min with a gradient of 0% to 97% B over 1.5 min then 97% B for 0.5 min. Spectra were processed using MassLynx. Deconvolution was performed by MaxEnt1.

2.2.9 γS-crystallin crystallization, data collection, and structure refinement

Crystallization conditions were found via sparse matrix screening. Crystallization occurred at 20 ℃ and the protein:precipitant ratio was 1:1. For all protein samples, the lyophilized powder was resolubilized and buffer exchanged into 50 mM HEPES pH 6.8 with 5 mM DTT. The addition of DTT allowed for a uniform starting condition for all samples with cysteines reduced. For γS-wt, γS-3, and γS-5, the samples were aged overnight at 4 ℃ before crystallization. For γS-wt, crystals were grown in the Morpheus screen G5 (0.1 M Carboxylic Acids Mix, 0.1 M Buffer System 2 pH 7.5, 30% v/v Precipitant Mix 1). The Carboxylic Acids Mix contains 0.2 M sodium formate, 0.2 M ammonium acetate, 0.2 M trisodium citrate, 0.2 M sodium potassium l-tartrate, and 0.2 M sodium oxamate. Buffer system 3 contains 0.1 M MOPS/HEPES-Na pH 7.5. Precipitant Mix 1 contains 20% w/v PEG 20 000 and 40% v/v PEG MME 550 [76]. Protein concentration was 12 mg/mL. Crystals appeared between 14-28 days and were harvested after 1.5 months. For γS-3 and γS-5, crystals were grown in the Hampton Index screen condition G10 (0.2 M $MgCl_2$, 0.1 M BIS-

TRIS pH 5.5, 25% w/v Polyethylene glycol 3350). Protein concentration was 18 mg/mL. Crystals appeared between 14-28 days and were harvested after 2 months. For γS-7, the protein sample was aged at 4 ℃ for 1-2 weeks before being crystallized in 0.1 M sodium acetate pH 5.0, 0.1 M ammonium sulfate, 28% PEG 3350. Crystals appeared after 1 day and were harvested after 1 week. For γS-9A, the protein sample was aged overnight at 4 ℃ before being crystallized in 0.1 M sodium acetate pH 5.45, 21% PEG 3350. Crystals appeared after 1 day and were harvested after 2-3 days. For γS-9B, the protein sample was aged at 4 ℃ for 1-2 weeks before being crystallized in 0.1 M sodium acetate pH 5.45, 0.1 M ammonium sulfate, 21% PEG 3350. Crystals appeared after 1 day and were harvested after 1 week. Crystals were cryoprotected with Paratone-N and flash-frozen by plunging into liquid nitrogen. X-ray diffraction data were collected at both the P13 or P14 beamline operated by the European Molecular Biology Laboratory (EMBL) at the PETRA-III synchrotron at DESY, Hamburg, Germany (https://www.embl-hamburg.de/services/mx/P13/ or https://www.embl-hamburg.de/services/mx/P14/). Diffraction was recorded on a PILATUS 6M or EIGER 16M detector. Diffraction data was processed using XDS [77]. Phasing was performed using Phaser molecular replacement with chain A of PDB model 6FD8 as a search model [78]. Refinement was performed using the Phenix software suite with iterative manual improvement in Coot [79, 80]. Structure images were generated in PyMOL (Schrödinger).

2.3 Results

2.3.1 γS deamidated variants are less stable and more aggregation prone than wild-type

We investigated the stability and aggregation propensity of the deamidated variants compared to γS wild-type (γS-wt). Thermal unfolding curves were determined by differential scanning fluorimetry (DSF), and the midpoint of the unfolding temperatures (T_m) were calculated for each variant (Figure 2.2A). The percent unfolded was calculated via fitting of the averaged fluorescence intensity data (Figure A.3) to a Boltzmann function as described by Wright *et al.* [70]. The thermal stability progressively decreased with cumulative deamidations from a T_m of 76.79 ± 0.06 ℃ for γS-wt to 73.91 ± 0.07 ℃, 72.26 ± 0.01 ℃, 71.62 ± 0.02 ℃ and 70.45 ± 0.04 ℃ for γS-3, γS-5, γS-7, and γS-9, respectively (Figure 2.2B). A linear relationship emerges from the comparison of the T_m and the calculated net charge at neutral pH for each variant, with increased charge leading to decreased stability in these variants. Calculations of net charge were performed with the Prot pi protein tool (https://www.protpi.ch/Calculator/ProteinTool).

Thermally induced aggregation was monitored with dynamic light scattering (DLS). All proteins appeared monomeric at 25 ℃ with diameters of 2-4 nm and remained monomeric until the rapid formation of large, insoluble aggregates at the aggregation onset temperature, T_{agg} (Figure 2.2C). The values of T_{agg} were 63 ℃ for γS-wt and 60 ℃, 58 ℃, 61 ℃, and 62 ℃ for γS-3, γS-5, γS-7, and γS-9, respectively. All deamidated variants showed a lower T_{agg} compared to γS-wt; however, while T_{agg} for γS-3 and γS-5 decreases with successive deamidations, for γS-7 and γS-9, the trend reverses (Figure 2.2D). We hypothesized that the repulsive effects from the high net charge of γS-7 and γS-9 begin to offset the minor destabilization produced by deamidations, resisting aggregation.

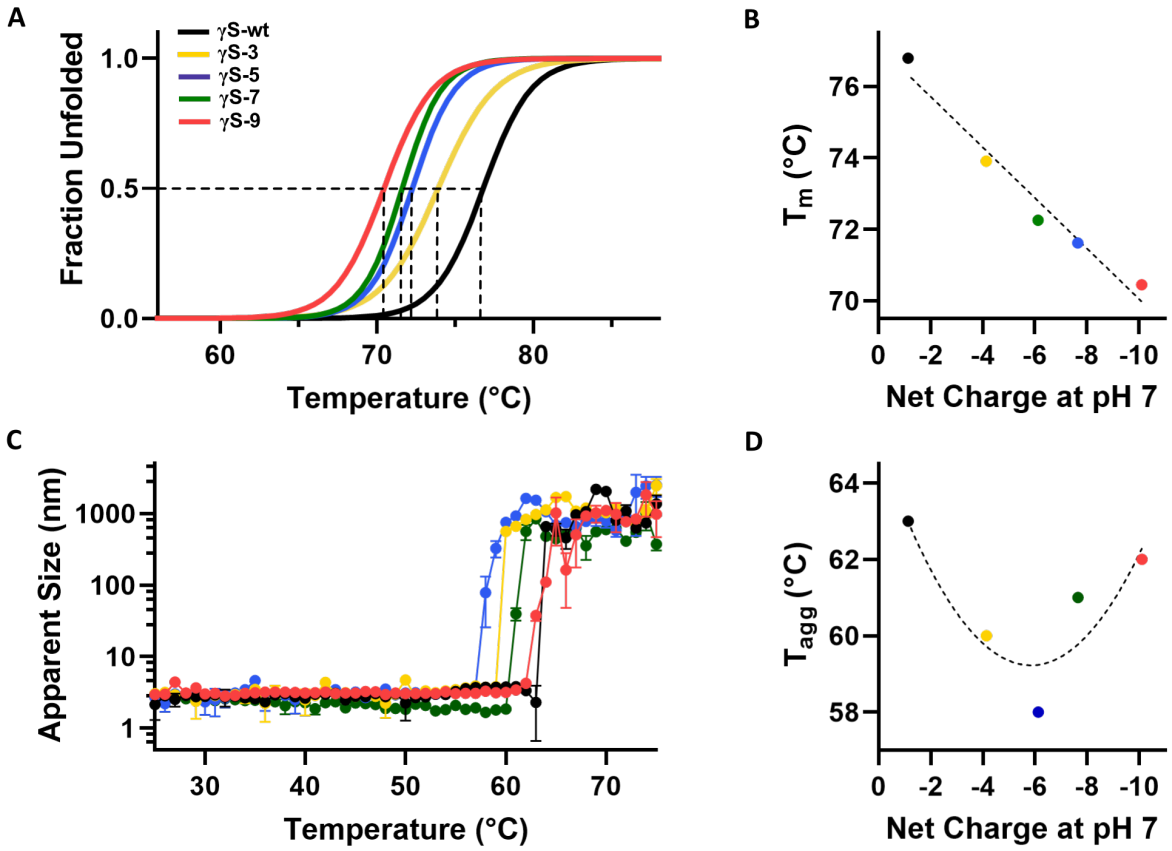

Figure 2.2: The stability and thermal aggregation of γS-crystallin wild-type (γS-wt, black), 3-site (γS-3, yellow), 5-site (γS-5, blue), 7-site (γS-7, green), and 9-site deamidation variant (γS-9, pink). (A) Differential scanning fluorimetry (DSF) was used to determine the percent unfolded as a function of temperature for γS wild-type and each variant. (B) The mid-point temperature of the thermal unfolding (T_m) of γS wild-type and each variant plotted against the net charge of the protein at neutral pH. (C) Dynamic light scattering (DLS) measurements of γS wild-type and each variant to monitor thermally induced aggregation of γS wild-type and each variant. (D) The temperature of aggregation onset (T_{agg}) plotted against the net charge of the protein at neutral pH.

2.3.2 Increasing repulsive interactions from deamidation

In order to assess interprotein interactions, we aimed to determine the osmotic second virial coefficient (A_2). A_2 characterizes the resultant force of individual interparticle interactions and has been used as a predictive measure for protein solubility, crystallization, aggregation, and liquid-liquid phase separation [81]. We used small angle X-ray scattering (SAXS), which yields information on protein size and shape (form factor) as well as interprotein interactions (structure factor). The SAXS profiles show, in agreement with the crystal structures, that the overall fold of the protein is maintained among the variants (Figure 2.3A). The form factor stays consistent among variants as well as among concentrations, with the profile showing no shifts from concentration effects up to 40 mg/mL (Figure A.4). However, at low scattering vectors, q, deviations from ideality are seen that reflect the interprotein interactions (Figure 2.3B). The Guinier plot for an ideal, non-interacting particle is linear at low q. Deviations from linearity are observed as positive for the γS-wt and γS-3 and negative for γS-7 and γS-9. Solving for the structure factor at q=0 as a function of concentration allows for the calculation of A_2 from the slope of the linear regression (Figure 2.3C). We found in the low ionic strength buffer used in these studies, the A_2 values for γS-wt and γS-3 were in the attractive regime at -0.59 and -0.56 $\times 10^{-4}$ mol mL g^{-2}, within the estimated error of each other. For γS-5, the value approaches ideality, with a value of +0.15 $\times 10^{-4}$ mol mL g^{-2}. For γS-7 and γS-9, repulsive forces are observed with positive A_2 values of +1.45 and +2.40 $\times 10^{-4}$ mol mL g^{-2}, respectively (Figure 2.3C). Despite the increased repulsive forces, thermally-induced aggregation (Figure 2.2D) was still enhanced for all deamidated variants, indicating aggregation propensity is influenced by both protein-protein interactions and structure destabilization (Figure 2.2B).

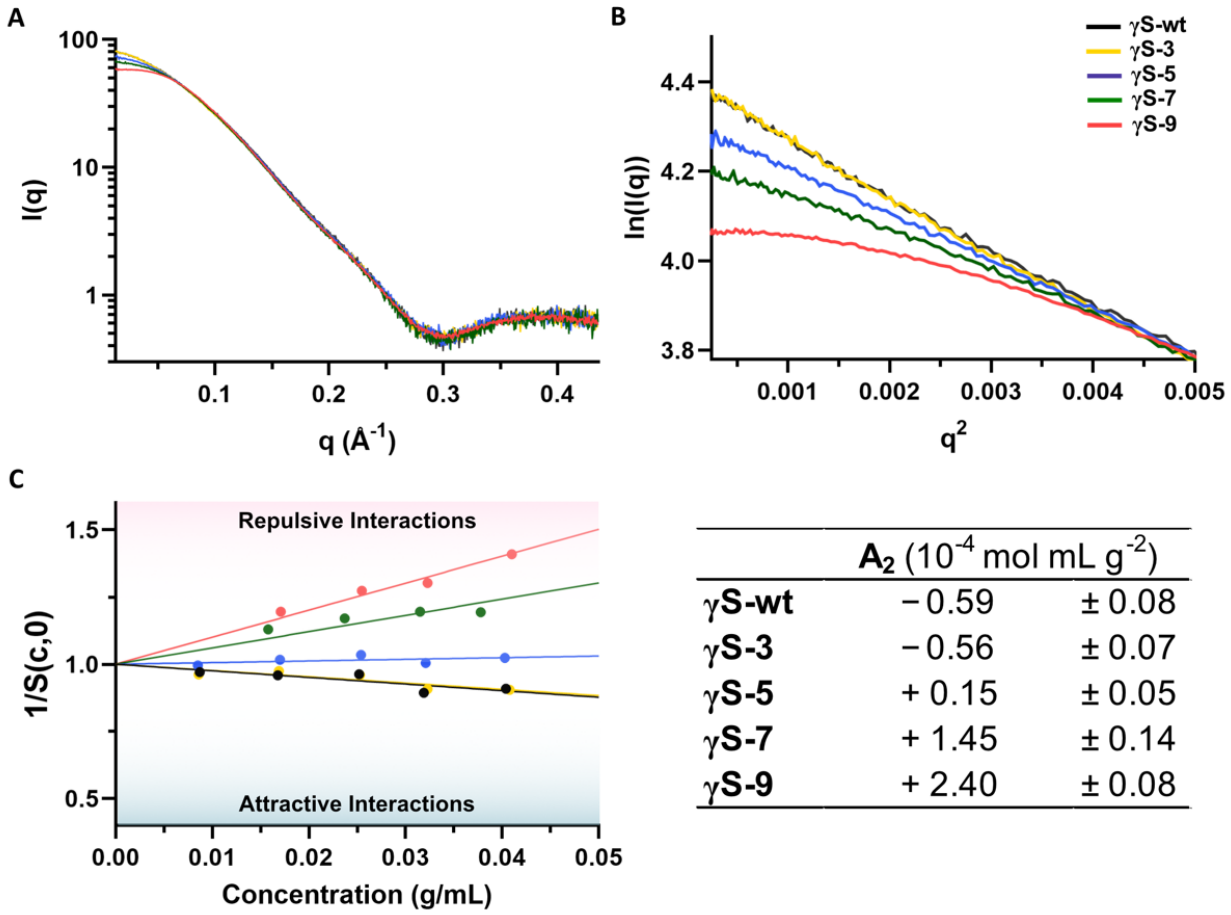

	A_2 (10^{-4} mol mL g^{-2})	
γS-wt	− 0.59	± 0.08
γS-3	− 0.56	± 0.07
γS-5	+ 0.15	± 0.05
γS-7	+ 1.45	± 0.14
γS-9	+ 2.40	± 0.08

Figure 2.3: (A) Small angle X-ray scattering (SAXS) profiles for γS-crystallin wild-type (γS-wt, black), 3-site (γS-3, yellow), 5-site (γS-5, blue), 7-site (γS-7, green), and 9-site deamidation variant (γS-9, pink) at approximately 40 mg/mL. (B) Guinier plot of the scattering profiles of each variant at approximately 40 mg/mL. For both (A) and (B), the profile for γS-7 was scaled to normalize for concentration. (C) Left: The reciprocal of the structure factor at q = 0 as a function of concentration. Right: Second virial coefficient (A_2) values calculated from the slope of the linear regressions.

2.3.3 Crystal structure of monomeric wild-type γS-crystallin

We report the first crystal structure of full-length, monomeric wild-type human γS-crystallin. Descriptive and crystallographic parameters for the structures discussed in this paper are summarized in Table 2.1. The space group was found to be $P2_1$ with an asymmetric unit containing two γS-crystallin monomers. In contrast to the previously reported disulfide-bonded dimeric structure, these monomers interact only through non-covalent contacts between the N-terminal domains [64]. The structure was solved at a resolution of 2.0 Å and the coordinates have been deposited in the PDB (PDB ID: 7N36). As with other reported γS-crystallin structures, it shows two highly symmetric domains comprising the two double Greek key motifs characteristic of the $\beta\gamma$-crystallins (Figure 2.4A). Structural alignments of the Cα atoms show this novel structure has high similarity with both the γS-wt NMR structure (PDB: 2M3T) and the crystal structure of the C-terminal domain of γS-wt (PDB: 1HA4), with RMSDs of 1.78 and 1.03 Å, respectively. These RMSDs were derived by the alignment of chain A of 7N36 with the entire 2M3T structure using the lowest energy state in the ensemble and chain A of 1HA4 [82, 83]. The regions of structural difference between 2M3T and 7N36 are mostly localized to the C-terminal domain, with the loop containing K154 and K155 as well as the linker region between the domains showing the maximum difference (Figure A.5). Notably, in all the crystal structures reported here, these are regions that show extensive dynamics, with high B-factors and/or multiple conformations. Likewise, in comparison to disulfide dimerized γS-crystallin structure (PDB: 6FD8), we observe very little structural difference in protein fold, consistent with the analysis by Thorn *et al.*, with a Cα RMSD of 0.59 Å, derived from the alignment of chain A of 7N36 and chain A of 6FD8. In both the NMR structure (2M3T) and this novel structure, no disulfide bonds, either intra- or intermolecular, are observed (Figure 2.4B).

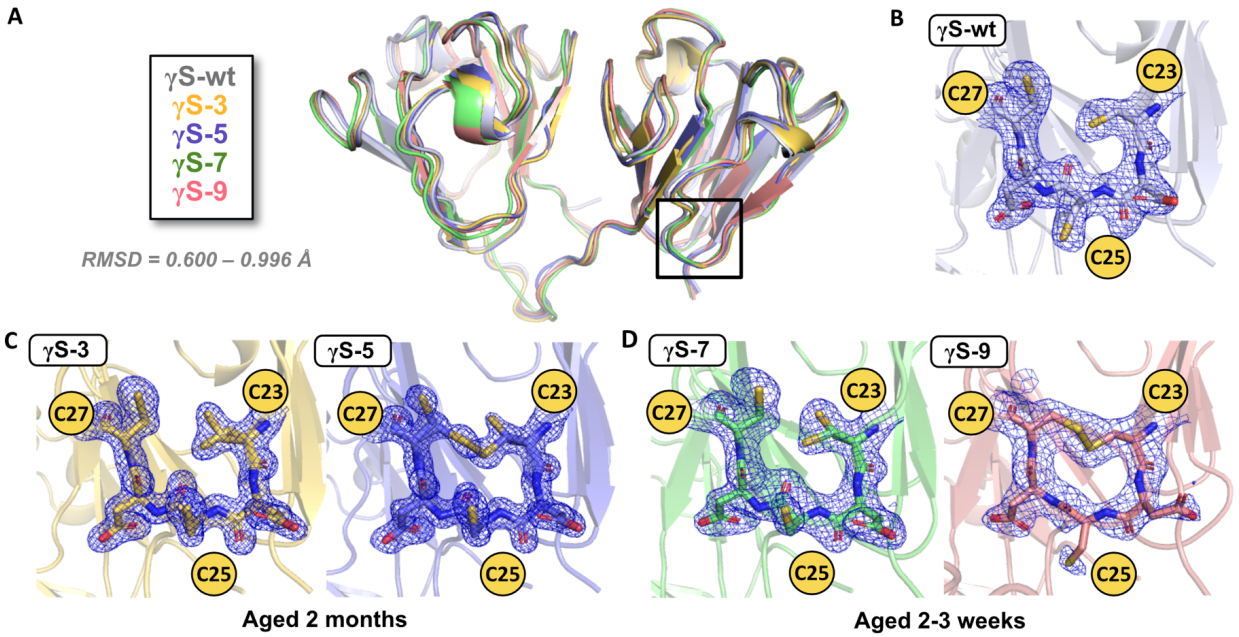

Figure 2.4: (A) Alignment of the novel structures of γS-crystallin wild-type (γS-wt, PDB: 7N36, gray), 3-site deamidation variant (γS-3, PDB: 7N37, yellow), 5-site deamidation variant (γS-5, PDB: 7N38, blue), 7-site deamidation variant (γS-7, PDB: 7N39, green), and 9-site deamidation variant (γS-9B, PDB: 7N3B, pink). All structures have Cα RMSDs less than 1 Å compared to γS-wt, PDB: 7N36. Magnified views of the cysteine loop region with $2F_o$-F_c (contoured at 1σ) electron density maps for (B) γS-wt aged 1.5 months, (C) γS-3 and γS-5 aged 2 months and (D) γS-7 and γS-9B aged 2-3 weeks.

2.3.4 Crystal structures of γS-crystallin deamidated variants

Five novel crystal structures have been determined for deamidated variants of γS-crystallin at various stages of sample aging. Sample age is the combined time of storage at 4 ℃ after resolubilization and time spent in the crystallization plate until the crystals were frozen for diffraction data collection. All samples were reduced with dithiothreitol (DTT) to establish a fully reduced starting point prior to aging and crystallization. We have confirmed with Ellman's assay, mass spectrometry, and size-exclusion chromatography that this treatment reduces the disulfide bonds in all variants (data not shown). Given the short half-life of DTT [84], we suspect very little reducing agent remains active during crystallization after several weeks, allowing the progression of cysteine oxidation. The γS deamidation variants crystallized in a variety of space groups (Table 2.1). The 3-site deamidation variant (γS-3)

and the 5-site deamidation variant (γS-5), both aged for 2 months and grown in the same crystallization solution, were found in space group $P2_12_12_1$ with a single monomer in the asymmetric unit. The structures for γS-3 and γS-5 were solved at resolution of 1.30 and 1.22 Å, respectively. The refined structures have been deposited in the PDB (PDB ID: 7N37 and 7N38). In both structures, a Mg^{2+} ion was identified, although in different locations. There were no direct interactions between the Mg^{2+} and any residues; interactions occurred through hydrogen bonding with Mg^{2+}-coordinated waters. γS-crystallin has shown binding and aggregation in the presence of other divalent cations, including Cu^{2+}, Zn^{2+}, Ni^{2+}, and Co^{2+}, but shows no such interactions with Mg^{2+} [35, 65].

The structures for γS-7 and γS-9B, both aged for 2 – 3 weeks and grown in similar crystallization conditions to each other, were solved at a resolution of 1.56 and 2.09 Å, respectively. They were both found to be in space group $P22_12_1$ with two monomers in the asymmetric unit. The refined structures have been deposited in the PDB (PDB ID: 7N39 and 7N3B). An additional structure was solved of γS-9 from protein aged for 4 – 5 days (γS-9A). γS-9A crystallized in space group $P2_1$ with one monomer in the asymmetric unit and was solved at a resolution of 1.50 Å (PDB ID: 7N3A). In general, the deamidated variants grew crystals more readily, in multiple different conditions in the sparse screens, and more reproducibly than γS-wt. Other mutations in crystallins have been shown to enhance crystallization, notably R58H and R36S in γD-crystallin, which lead to the formation of crystal cataract [85].

2.3.5 γS-crystallin deamidation is not significantly detrimental to protein fold

Despite the enhanced crystallization propensity of the variants, the fold of γS-crystallin is remarkably resistant to change after extensive deamidation. Relative to the new γS-wt

Table 2.1: X-ray data collection and refinement statistics for γS and deamidated variants

	γS-wt	**γS-3**	**γS-5**	**γS-7**	**γS-9A**	**γS-9B**
PDB	7N36	7N37	7N38	7N39	7N3A	7N3B
Wavelength (Å)	0.9762	0.9763	0.9763	0.9763	0.9762	0.9763
Space group	$P2_1$	$P2_12_12_1$	$P2_12_12_1$	$P22_12_1$	$P2_1$	$P22_12_1$
a, b, c (Å)	52.8, 60.6, 56.0	29.5, 62.6, 79.6	29.3, 62.7, 79.8	49.2, 76.6, 94.7	29.8, 57.7, 44.9	48.7, 75.8, 93.4
α, β, γ ()	90.0, 117.5, 90.0	90.0, 90.0, 90.0	90.0, 90.0, 90.0	90.0, 90.0, 90.0	90.0, 103.3, 90.0	90.0, 90.0, 90.0
Total reflections	146421 (14703)	473244 (46020)	528084 (20734)	682592 (67123)	160193 (16077)	270089 (26342)
Unique reflections	20807 (2056)	36161 (3477)	41328 (2350)	51461 (5051)	23517 (2292)	20969 (2008)
Multiplicity	7.0 (7.2)	13.1 (13.2)	12.8 (8.8)	13.3 (13.3)	6.8 (6.9)	12.9 (13.1)
Completeness (%)	97.42 (97.07)	97.57 (95.18)	93.52 (54.14)	99.61 (99.00)	98.40 (97.03)	99.73 (98.14)
Mean I/sigma(I)	16.29 (2.37)	27.64 (2.00)	30.24 (2.32)	27.17 (1.76)	13.85 (1.24)	13.98 (1.43)
Wilson B-factor	39.6	17	15.6	26.2	25.4	39
R_{merge}	0.06225 (0.7879)	0.04061 (1.275)	0.03872 (0.8968)	0.04674 (1.609)	0.05397 (1.855)	0.1236 (1.642)
R_{meas}	0.06731 (0.8493)	0.04234 (1.325)	0.04035 (0.9517)	0.04869 (1.674)	0.05855 (2.004)	0.1288 (1.708)
$CC_{\frac{1}{2}}$	0.999 (0.782)	1.000 (0.795)	1.000 (0.715)	0.999 (0.753)	0.999 (0.734)	0.998 (0.674)
CC*	1.000 (0.937)	1.000 (0.941)	1.000 (0.913)	1.000 (0.927)	1.000 (0.920)	1.000 (0.898)
Reflections used in refinement	20797 (2056)	36160 (3478)	41328 (2348)	51460 (5048)	23388 (2286)	20969 (2008)
Reflections used for R-free	962 (101)	1811 (172)	2077 (108)	2650 (256)	1147 (108)	1083 (99)
R_{work}	0.1891 (0.2478)	0.1451 (0.2398)	0.1464 (0.2219)	0.1934 (0.3036)	0.1953 (0.4619)	0.1884 (0.2879)
R_{free}	0.2199 (0.3105)	0.1793 (0.3169)	0.1792 (0.2817)	0.2127 (0.3241)	0.2237 (0.5012)	0.2396 (0.3641)
Number of non-hydrogen atoms	3030	1731	1830	3442	1578	3058
macromolecules	2912	1521	1588	3130	1468	2935
ligands	-	29	15	5	-	-
solvent	118	181	227	307	110	123
Protein residues	348	174	174	348	173	348
RMS bonds (Å)	0.006	0.014	0.01	0.006	0.008	0.007
RMS angles ()	0.88	1.3	1.07	0.81	0.99	0.94
Ramachandran						
favored (%)	96.8	98.84	98.26	96.51	95.91	95.06
allowed (%)	3.2	1.16	1.74	3.49	3.51	3.49
outliers (%)	0	0	0	0	0.58	1.45
Rotamer outliers (%)	0.98	1.83	1.76	3.02	3.21	3.25
Clashscore	5.67	3.62	5.43	4.26	6	6.9
Average B-factor	43.59	24.73	20.92	35.75	36.02	45.7
macromolecules	43.52	23.09	19.06	34.81	35.41	45.69
ligands	-	54.04	29.52	72.73	-	-
solvent	45.35	33.9	33.35	44.68	44.25	46.06

crystal structure (PDB: 7N36), the backbone fold is maintained in all deamidation variants, even for the highly deamidated γS-9. The Cα RMSD relative to the wild-type structure does not exceed 1 Å for any deamidated variant (Figure 2.4A). Additionally, the intramolecular disulfide bond observed in the γS-9B crystal structure does not seem to significantly affect protein fold, with a Cα RMSD of 1.19 Å in comparison to chain A of γS-9B to the γS-9A structure.

2.3.6 Deamidated γS-crystallin variants have a higher propensity for disulfide formation

Comparisons of different crystal structures can be challenging, as many factors related to crystallization or diffraction data collection, rather than the protein structure, can have substantial effects. Additionally, the rate of oxidation may be affected by the crystallization conditions. To this end, we limit our direct comparisons of crystal structures to γS-3 vs. γS-5 and γS-7 vs. γS-9B. These structures were determined from protein samples that were grown in identical or highly similar crystallization conditions and formed crystals in the same space group, with similar unit cells, and of comparable sizes. The data collection strategies were kept uniform so that radiation dose would also be consistent between samples.

Comparing crystal structures from samples aged for similar periods, we observe an increase in disulfide bond formation in variants with more deamidation. After aging for 2 months, the γS-3 structure has fully reduced cysteines (Figure 2.4C). In contrast, the γS-5 structure shows a mixed state for C23 and C27, with both reduced and disulfide-bonded species present (Figure 2.4C). Occupancy refinement in Phenix suggests that the disulfide-bonded configuration accounts for ∼50-70%, with a range estimated due to the different occupancy calculation for the two cysteines, C23 and C27. The same trend is observed in samples aged 2-3 weeks, γS-7 and γS-9B. The γS-7 structure shows the cysteines to be fully reduced,

while the γS-9B structure shows C23 and C27 are fully oxidized, forming an intramolecular disulfide bond (Figure 2.4D). The fourth cysteine in the tetrad, C83, is not shown in these maps, but in all cases it appears to be fully reduced. This may indicate that C83 is not amenable to disulfide bonding or that the C83 disulfide-bonded structure is unfavorable for crystallization, possibly due to large structural disruption from this bond.

To support these observations of the crystal structures, we also conducted a biochemical assay to evaluate free thiol content over the course of sample aging at room temperature. Ellman's assay is a colorimetric method used to estimate sulfhydryl content in a sample using 5,5-dithio-bis-(2-nitrobenzoic acid) (DTNB). DTNB reacts with free thiols and releases TNB, which absorbs at 412 nm. In order to get a full understanding of the thiol content, including buried cysteines, the samples were denatured with 2% SDS prior to reaction with DTNB. The extinction coefficient of TNB in the buffer used was calibrated using DTT and was calculated to be 12968 $M^{-1}cm^{-1}$ (Figure A.2). The rate of the reaction differed for each deamidation variant, with more deamidated sites leading to longer reaction times (Figure A.6). All samples showed initial thiol content after purification was between 6.2 – 6.6 free thiols per protein molecule, consistent with the known 7 cysteines in γS (Figure A.7). Measurements of thiol content were then collected over 18 days (Figure 2.5A) of aging at room temperature. In the first two days of aging, the free thiol content of the samples decreased more rapidly with more deamidated sites, with the thiol content decreasing to 98%, 96%, 93%, 92% and 84%, for γS-wt, γS-3, γS-5, γS-7, and γS-9, respectively. After the first 6 days of aging at room temperature, the rate of thiol loss slowed. After 18 days, the oxidation of the samples reached 60-70% of their starting thiol content. It should be noted that the rate of oxidation was observed to depend significantly on buffer aeration. Samples stored in degassed buffer after size-exclusion chromatography showed very little oxidation over several months, while samples stored in dialysis in stirring buffer oxidized extremely rapidly. In order to age samples in an equivalent manner, during purification the samples for these experiments were reduced with DTT, the DTT was removed via buffer exchange, then the

samples were lyophilized. The lyophilized powders were resuspended in buffer from the same stock, achieving the same aeration for all samples.

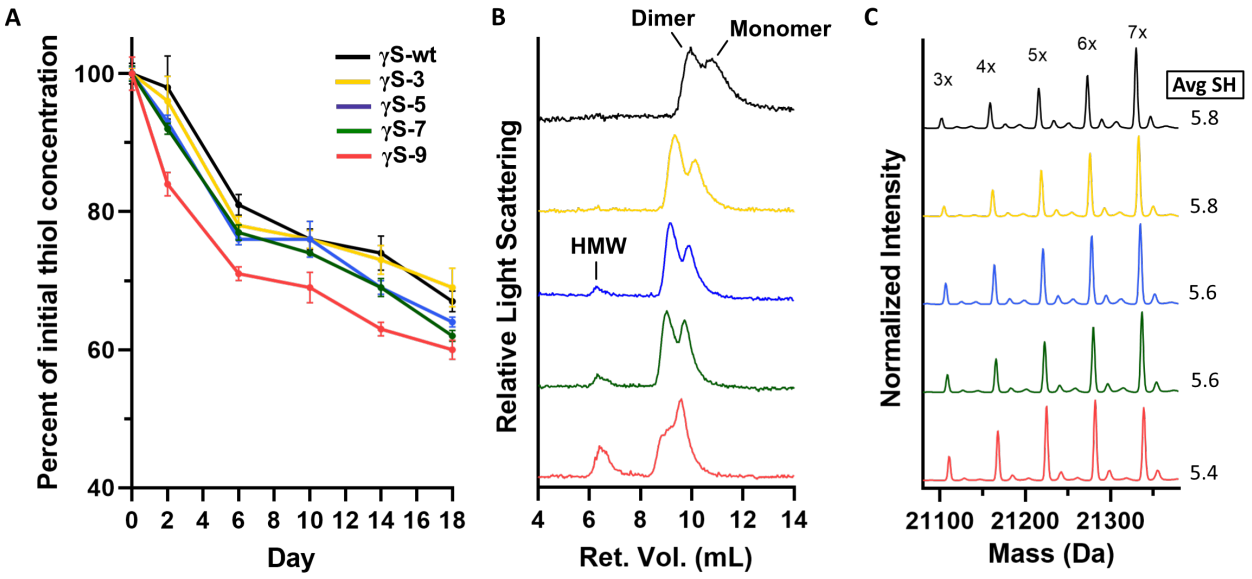

Figure 2.5: (A) Assessment of the decrease in free thiol content over time using Ellman's assay for γS-crystallin wild-type (γS-wt, black), 3-site (γS-3, yellow), 5-site (γS-5, blue), 7-site (γS-7, green), and 9-site deamidation variant (γS-9, pink). (B) Size-exclusion chromatography in line with multiangle light scattering (SEC-MALS) conducted on each variant after aging for 1 month. High molecular weight (HMW) peaks are seen in γS-5, γS-7, γS-9. (C) Intact mass spectra of each aged variant after reaction with iodoacetamide (IAM) and subsequent reduction with dithiothreitol (DTT). The average free thiol content per protein molecule weighted by the peak intensity decreases with increasing deamidation.

The decrease in free thiol content as evaluated by Ellman's assay may arise from the oxidation of cysteines, but also from the protein aggregation reducing the accessibility of thiol groups. We therefore conducted size-exclusion chromatography multi-angle light scattering (SEC-MALS) experiments to evaluate the formation of disulfide bonded dimers as well as the formation of high molecular weight aggregates. Figure 2.5B shows the results of SEC-MALS studies on γS-wt and the deamidation variants after aging for 1 month at room temperature. All samples contained both monomer and dimer, with the γS-3 and γS-5 appearing to form more dimer than γS-wt. These data suggest that deamidation promotes the formation of dimers. These dimers were confirmed to be disulfide bonded, as they were reduced by

treatment with DTT (data not shown). However, for the γS-7 and γS-9, less dimer is present than in the γS-3 and γS-5 samples. Dimerization may be inhibited by their higher surface charge and the repulsive forces between molecules. Additionally, the dimer form of γS-wt is known to be less stable [64], therefore the already deamidation-destabilized γS-7 and γS-9 upon dimerization may form high molecular weight HMW oligomers/aggregates. The increased propensity of deamidated variants to aggregation induced by oxidation has previously been shown [54]. We also detected HMW peaks in the γS-5, γS-7, γS-9 (Figure 2.5B). For γS-9, the SEC-MALS experiment also shows a shoulder of the monomer peak blending into the dimer peak, unlike the other traces. We hypothesize this peak shape arises from a partially unfolded state.

We next aimed for a more detailed understanding of the disulfide state of aged samples. Samples aged for 1.5 months were denatured in 8 M urea to solubilize HMW aggregates. The denatured samples were then reacted with iodoacetamide (IAM), which modifies free thiol groups and imparts a mass shift of +57 for each addition. The samples were subsequently treated with DTT to reduce the dimer and any internal disulfide bonds. Figure 2.5C shows the deconvoluted intact mass spectra for aged γS-wt and the deamidated variants. All samples show a distribution of IAM mass additions, from 3 up to 7 additions, with 7 being the total number of cysteines present in γS. As IAM adds to free thiols and not to disulfide-bonded sulfurs, the number of IAM additions indicates the number of thiols per protein molecule. A calculation of the weighted average for each variant reveals a decrease in the number of thiols with increasing deamidation, with 5.8, 5.8, 5.6, 5.6, and 5.4 for γS-wt, γS-3, γS-5, γS-7, and γS-9, respectively.

2.3.7 Disulfide bonding in the cysteine loop during sample aging

Because no significant structural disruption to the protein fold is observed in the deamidated variants, we propose that they may serve as more crystallizable models for the wild-type protein to gain atomic and near-atomic resolution structures at varying time points. Structural changes over time in the deamidated variants may give insight into the aging behavior of the wild-type protein, but in an accelerated timeframe. In this study, γS-9 was crystallized at two time points of sample age: several days and several weeks. Recently, we reported another crystal structure of γS-9 that was aged for several months prior to crystallization in a silicon chip. That structure was solved via a fixed-target serial crystallographic approach using microcrystals to a resolution of 3.0 Å (referred to here as γS-9C, PDB: 7NJE) [86]. The comparison of these three structures allows us to observe the change in cysteine oxidation over time (Figure 2.6). In the earliest time point structure, γS-9A, the protein is monomeric and all three cysteines appear to be mostly reduced, with minor partial occupancy of a C23-C27 disulfide bond (Figure 2.6A). After several weeks, as discussed above, γS-9B has a full intramolecular disulfide between C23 and C27 and the protein remains monomeric (Figure 2.6B). After several months, γS-9C contains a second disulfide bond between C25 and C25 of another γS-9, forming a dimer (Figure 2.6C). Interestingly, the orientation of C25 shifts after the formation of the C23-C27 disulfide bond. In γS-9A, the side chain of C25 projects out from the ring and has a high calculated solvent exposed surface area (SASA) of 85 Å2. Similarly, γS-wt shows fully reduced cysteines with a SASA of 82 $Å^2$ calculated for C25. In γS-9B, after the formation of the C23-C27 disulfide, C25 flips and the SASA is lowered to 30 $Å^2$. SASA values were calculated by AREAIMOL in the CCP4 package [87, 88].

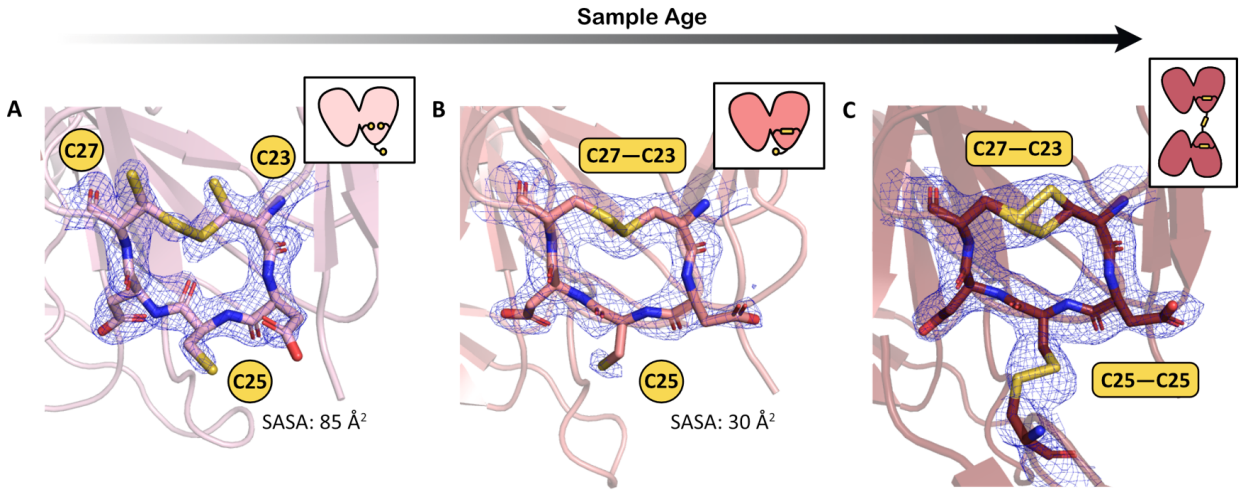

Figure 2.6: Magnified views of the cysteine loop region with $2F_o$-F_c (contoured at 1σ) electron density maps for (A) γS-9 aged for several days (γS-9A, PDB: 7N3A), (B) γS-9 aged for several weeks (γS-9B, PDB: 7N3B), and (C) γS-9 aged for several months (γS-9C, PDB: 7NJE). Insets show a cartoon depiction of the γS-9 structures indicating their oligomeric states (either monomeric or dimeric) with intramolecular and intermolecular disulfide bonds in the cysteine loop shown. The solvent accessible surface area (SASA) for C25 is lower after disulfide bond formation between C23 and C27.

2.4 Discussion

2.4.1 Deamidation accelerates oxidative aging

In comparing structures of samples of γS-wt and deamidation variants aged for time periods ranging from several days to several months, we observe an increased propensity for disulfide bonding with increased deamidation. The duration of sample aging of γS-wt, γS-3 and γS-5 was similar, between 1.5 – 2 months; however, only γS-5 shows partial occupancy of disulfide bonded C23-C27. At an earlier aging timepoint, γS-7 and γS-9 can be compared after several weeks aging; γS-7 remains fully reduced, while γS-9 shows a full disulfide bond between C23-C27. Based on this trend, we propose that deamidation accelerates the process of oxidative aging, possibly by increasing conformational flexibility, which then increases solvent exposure of the cysteine residues. Additional experiments using Ellman's assay and mass

spectrometry after thiol blocking with iodoacetamide (IAM) on aged samples also supported the trend of increased oxidation with increased deamidation (Figure 2.5). Other studies have linked deamidation with an increase in conformational dynamics and oxidation, even in regions distant from the sites of deamidation. Forsythe *et al.* showed that deamidation of two surface Asn residues in the N-terminal domain of γS caused long-range disruption of conformational dynamics in the C-terminal domain [49]. Their work suggested that deamidation induced both local and global transient unfolding and that thermally-induced aggregation was enhanced for the deamidation variants in the presence of oxidized glutathione. Vetter *et al.* followed up on this study, demonstrating that with three deamidation mutations, γS again became more susceptible to oxidation-induced aggregation [54]. These previous studies and the results described here support allosteric conformational effects that destabilize protein structure and increase conformational dynamics, leading to increased susceptibility to oxidation.

The mutated residues (glutamine to glutamic acid and asparagine to aspartic acid) are structurally highly similar; therefore, the difference in charge after mutation is the likely basis for the altered structural dynamics. Upon deamidation, a negative charge is introduced at each deamidated site as the carboxylic acid moiety is ionized at the relevant pH values. These charges not only lower the pI of the protein significantly, but also induce regions of high negative charge on the surface of the protein (Figure A.8). At neutral pH, γS-wt has an expected net charge of -1. With each additional deamidation mutation, the net charge decreases, reaching -10 for γS-9. A complex picture emerges from the evaluation of the benefits and drawbacks of introducing negative charges. Chong *et al.* proposed that additional negative charges increase the solubility for proteins that already have a net negative charge [89]. However, the introduction of charged sites can also lead to an increase in fluctuating conformational transitions, or transient misfolding, which can drive aggregation through exposure of hydrophobic portions of the protein [90]. Particularly for γ-crystallins, the drastic changes to surface charge might cause further disruption in the lens via the

impairment of α-crystallin chaperone activity, as demonstrated previously for a deamidated variant of γS [54].

Our findings support the hypothesis of the competing role between net charge and conformational dynamics in governing aggregation propensity. As the deamidated variants gained negative charge, their structural stability decreased, as indicated by the observed unfolding temperatures (Figure 2.2B). Lower stability likely promotes transient misfolding, prompting an earlier onset of thermally induced aggregation in moderately charged variants (γS-3 and γS-5); however, as the proteins reached high negative charge (γS-7 and γS-9), the greater electrostatic repulsion, as evidenced by their A_2 values, between molecules raises the energic barrier to aggregation (Figure 2.2D). Further studies into the local and global dynamic effects of charged residues are warranted.

2.4.2 γS serves as an oxidation sink in the lens

Previously, disulfide bonding in γS was thought to be solely a detrimental byproduct of oxidation. Recent work and the results of this study suggest that it may also be a functional adaptation that helps to sustain the redox balance in the lens [35, 63]. Here, we demonstrate that deamidation accelerates the oxidation of the C23, C25, and C27. Due to the unchanged global fold across the variants characterized in this study, we propose that we may extrapolate the behavior of the deamidated variants to the wild-type protein observed over a longer time period.

We suggest that the positioning of a highly solvent-exposed cysteine, C25, may be advantageous in γS due to its proximity to other cysteines that can form a stable internal disulfide bond. A possible mechanism for γS oxidoreductase activity emerges from the observations of the crystal structures determined in this study (Figure 2.7). Fully reduced, monomeric γS (**1**) contains the highly solvent-exposed C25, predisposing it to dimerization with a sec-

ond molecule of γS. Although this schematic diagrams the proposed in vitro process with only γS available for crosslinking, in the lens this may also occur with a different crystallin species. We propose a transient dimer (**2**) forms with a crosslinking disulfide bond between C25 and a C25 of another crystallin monomer. We hypothesize this intermediate with only a single dimerizing disulfide forms preferentially due to the high solvent exposure of C25 and its known propensity for dimerization at this site but suggest that this intermediate is quickly lost to disulfide exchange. This dimerizing bond exchanges with other nearby cysteines, forming an intramolecular disulfide bond between C23-C27 (**3**). This process removes a crosslinking disulfide bond and releases a recovered, reduced monomer of crystallin. After the formation of the C23-C27 bond, C25 occupies an orientation with reduced solvent exposure, as evidenced by the crystal structure of γS-9B. Further oxidation eventually leads to the formation of a fully oxidized and aggregation-prone dimer (**4**) [64], but this conversion may be slowed by the reduced solvent exposure of C25. The C23-C27 bond is apparently not highly disruptive to the protein fold in this region, indicating that this bond might serve to rescue γS or other crystallins from other, more deleterious disulfide bonds. If this hypothesis is correct, γS plays not only a structural role, but also a chemical role in the lens, acting as a final buffer against oxidative damage, even after depletion of glutathione.

In other proteins with disulfide reactivity, a CXXC motif has been reported, notably in thioredoxins and disulfide isomerases. The XX is often proline and glycine, both of which support a tight turn and the formation of a disulfide between the two cysteines [91]. The same activity is recapitulated with the CXC motif, where X is usually glycine [92]. The activity of a CXC motif has been previously reported for human γD-crystallin, in a study showing disulfide exchange between wild-type γD and an aggregation prone variant, W42Q [63]. In this case, X is serine, a highly flexible amino acid that is often present in flexible linker regions [93, 94]; however, the disulfide bond was still postulated to cause conformational strain in the C-terminal domain. Upon disulfide exchange between the wild-type and W42Q variant, γS-W42Q was more destabilized by the disulfide and more rapidly aggregated out of solution

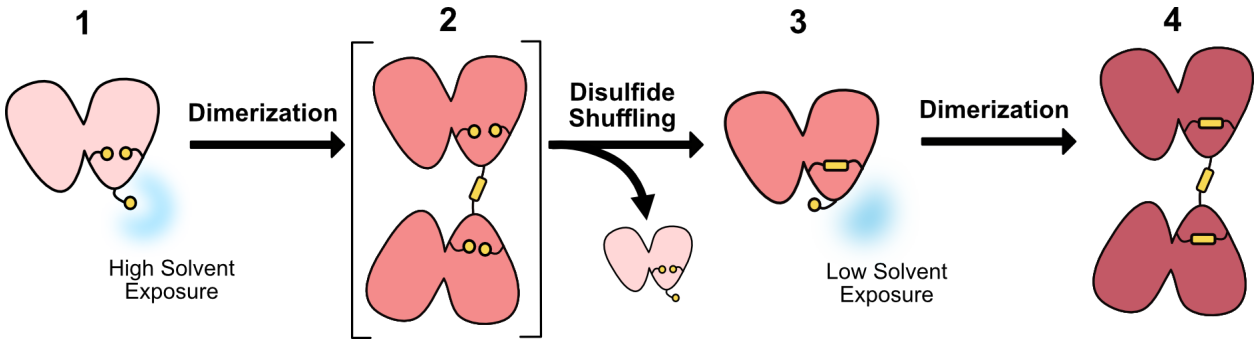

Figure 2.7: Potential mechanism for the role of γS-crystallin as an oxidation sink in the eye lens. Monomeric, reduced γS-crystallin (**1**) with a highly solvent exposed C25 accepts an intermolecular disulfide bond from another γS-crystallin or another oxidized crystallin in the eye lens. This partially oxidized dimer (**2**) undergoes disulfide shuffling and the disulfide bond exchanges to C23-C27 forming an intramolecular disulfide bonded monomer (**3**) and releasing a recovered, reduced crystallin monomer. The reduced solvent exposure of C25 in the single disulfide bond intermediate (**3**) slows the formation of the fully oxidized disulfide-bonded dimer (**4**) that has been shown to be prone to aggregation.

[63]. γS contains a similar, extended CXCXC motif. However, instead of glycine or proline that allow for tight turns, here the cysteines are separated by aspartic acid residues. As the structures reported here show, the favored disulfide forms between the first and last C in the motif (C23 and C27); the 3 separating residues likely allow for a less strained disulfide bond formation. Aspartic acid is, however, among the most flexible amino acids [93], lessening any structural disruption as well as supporting disulfide exchange between C25 and C23/27. The presence of aspartic acid in this motif raises additional questions; is there a fitness benefit from proximal acidic residues? Repulsive electrostatic interactions between deprotonated cysteine and neighboring negatively charged residues have been suggested to destabilize the thiolate state and thereby raise cysteine pK_a [95]. As thiolate is a much stronger nucleophile than the protonated thiol, an increase in cysteine pK_a would likely be inhibitory to thiol-disulfide exchange [96, 97]. Free cysteine in solution has a reported thiol pK_a of 8.6 and most noncatalytic cysteine pK_a's fall within 7.4 – 9.1 [95]; however, dramatic shifts can been seen for catalytic cysteines, with pK_a values as low as 2.88 reported [98]. The predicted pK_a for C25 in γS is 9.35, calculated with PROPKA using the γS-wt crystal structure, 7N36 [99, 100]. C25 is therefore predicted to be slightly more basic than glutathione, the major

antioxidant in the lens with a reported thiol pK_a of 8.92 [101]. In addition to similar pK_a values, C25 in the CDCDC motif of γS and the structure of glutathione also share structural similarities. Glutathione is a tripeptide (L-γ-glutamyl-L-cysteinyl-glycine) with the amide bond formed with the γ-carboxyl rather than the α-carboxyl of glutamic acid. Like C25 in γS, the cysteine in glutathione is flanked by adjacent carboxylates. We plan to further investigate the role of γS and its interplay with glutathione in maintaining redox homeostasis in the eye lens.

2.4.3 Deamidation as a basis for rational mutagenesis for crystallization

On a more methodological note, deamidation may serve as a new target for rational mutagenesis to promote crystallization. Excellent work has been done in this area, with much of the effort focused on surface entropy reduction (SER) [102]. In SER, surface residues with high conformational energy, such as Lys and Glu, are mutated to Ala or other small amino acids. This method is often successful but may sometimes lead to undesired structural changes. The deamidated variants reported here did not appear to change the overall fold of the protein but did more readily and reproducibly form crystals. For challenging crystallization targets, deamidation of surface Gln and Asn to Glu and Asp may provide less disruption to protein fold than other mutations, as the side chains are highly similar in size.

2.5 Conclusion

In conclusion, crystallins are among a unique class of extremely long-lived proteins (ELLPs). The half-lives of ELLPs far exceed those of average proteins, persisting for years or even the entire lifetime of an organism [103]. In metabolically inactive cells such as the eye lens, the

cells' resources to safeguard against protein degradation and aggregation are finite. Multiple and redundant mechanisms for maintaining lens transparency are likely necessary and the γ-crystallins appear to have a multidimensional role in the lens. γS-crystallin demonstrates resistance to significant structural change from deamidation mutations; however, these mutations predispose the protein to accumulate oxidative modifications. Furthermore, although glutathione is the main species responsible for maintaining redox balance in the lens, here we provide further evidence that γS-crystallin may also aid in reducing oxidized species by shuffling disulfide bonds internally to non-crosslinking positions. By this mechanism, γS may act as a last line of defense against oxidation. The proteins of the eye lens appear to employ methods to both counteract and exploit PTMs; the full role of crystallins and other lens molecules in slowing the irreversible aggregation that leads to cataract remains to be fully explored.

2.6 Author contributions

B.N.-B, K.W.R, and R.W.M designed the protein constructs and planned the biophysical experiments. B.N-B., P.M, R.J.D.M., and R.W.M. designed the crystallographic studies. B.N.-B, A.O.K, and M.A.S.-P prepared the protein. B.N.-B, P.M., and D.v.S. collected and processed crystallography data. B.N.-B performed the DSF, DLS, SAXS, and mass spectrometry experiments. B.N.-B and M.A.R. performed the SEC-MALS experiments. B.N.-B and R.W.M. wrote the manuscript. All authors edited the manuscript.

Chapter 3

Human γS-crystallin resists unfolding despite extensive chemical modification from exposure to ionizing radiation

3.1 Introduction

Protein stability and aggregation resistance are intimately connected with solvent interactions. Hydrophobic hydration in general is more complicated than the traditional "oil and water" picture suggests, as the balance between attractive and repulsive interactions depends on molecular size and geometry as well as solute polarity [104]. Vibrational spectroscopy has established that at low to moderate temperatures, water assumes a structure with more tetrahedral order and fewer weak hydrogen bonds around hydrophobic solutes than the bulk solution [105], although dangling O-H bonds are also observed near solvated hydrocarbons

[106]. Exposed hydrophobic functional groups can also form highly flexible π-hydrogen bonds, where the donor is a water and the acceptor is the π-system of the aromatic amino acid side chain [107]. Microscopic interactions between water and the heterogeneous functional groups of protein surfaces impact many protein properties beyond solubility, including diffusion of water near the protein surface [108–110], the compressibility [111] and even the refractive index increment [112].

Water is not just a passive solvent within cells, but is a key participant in many biochemical reactions [113]. Water facilitates electron transfer in enzymes, mediating tunneling between adjacent molecules [114] or stabilizing radical intermediates in the active site [115] via hydrogen bonding. In the type of radiation damage investigated here, water acts as a transmission medium for oxidative damage: direct damage of proteins by γ rays is a minor effect, with most of the deleterious modifications coming from reactions with reactive oxygen species (ROS) derived from water, primarily hydroxyl radical, although hydrogen peroxide is also significant [116]. Inside the cell, OH radical is particularly damaging, as it is highly reactive and cannot be neutralized enzymatically, unlike H_2O_2 [117]. Although DNA damage is often emphasized in studies of radiation toxicity, proteins are oxidized by hydroxyl radical before DNA or lipids [118]. The resulting protein hydroperoxide species can last for several hours and have the capacity to damage other molecules and deplete the cellular supply of antioxidants [119]. Assessing the impact of radiation damage is important for understanding the mechanisms of radiation tolerance in extremophiles [120, 121], the cellular damage caused by radiation therapy for cancer [122], and the potential for cataract formation as a consequence of ionizing radiation absorbed by the eye.

Exposure to ionizing radiation has been shown to cause cataract in humans and model organisms [123]. Populations susceptible to radiation cataract include radiological technicians [124], astronauts [125] and others who have accidental, occupational, or war-related exposure to ionizing radiation [126–128]. The upper dose limits of γ irradiation to the lens

suggested to prevent the onset of cataract are as low as 0.05 Gy over 5 years [129, 130]. These findings raise the question of whether radiation-induced cataract is a direct consequence of protein modification and aggregation or whether more complicated cellular damage is involved. The majority of the lens protein content comprises α-, β-, and γ- crystallins [131]. β- and γ- crystallins are structural proteins, whereas α-crystallins act as molecular chaperones. Studies on α-crystallins have shown that γ irradiation forms oxidation products, generates extensive cross-linking, damages the overall fold, and reduces chaperone activity. A previous investigation showed that rat lenses dosed with 5 Gy of γ radiation formed site-specific oxidations on γ- crystallins, particularly on cysteines, tryptophans, and methionines [132, 133]. Antioxidants such as vitamin E [134, 135] and melatonin [136] have delayed the onset of radiation-induced cataract in model organisms, further supporting an important mechanistic role for ROS.

Here we investigate resistance to unfolding of human γS-crystallin (HγS), a major structural protein of the eye lens, upon exposure to γ radiation. Structural crystallins such as HγS are extremely stable and soluble, in keeping with their biological role. The vertebrate eye lens is primarily composed of enucleated lens fiber cells that undergo degradation of internal organelles during early development, in part due to lipase activity [137] and the ubiquitin-proteasome system [138]. The loss of most cellular components leaves behind a highly concentrated ($>$ 400 mg/mL) solution of proteins, mostly crystallins [131]. Crystallin solubility persists despite damage caused by aging, exposure to ultraviolet (UV) radiation, modification by reactive oxygen species (ROS), and other deleterious chemical reactions [10, 46]. Glutathione and other antioxidants provide some protection from ROS [139], however many post-translational modifications (PTMs) have been observed in aged lenses, including deamidation and oxidation [28, 140].

The aggregation resistance of the proteins themselves is partly due to fluorescence quenching mechanisms that quickly relax excited states via thermal motion before photochemistry

can occur [141–143]. This wealth of information about aggregation resistance in structural crystallins leads to questions about the response of these highly soluble proteins to radiation damage, which has been shown to cause cataract: are structural crystallins such as HγS resistant to aggregation upon exposure to ionizing radiation? If they are, is it a result of increased resistance to oxidative damage or because the proteins are able to tolerate a high level of chemical modification while remaining soluble? Our results indicate that HγS is unusually robust to unfolding even when treated with high levels of γ radiation and that this resistance is due to its high tolerance for modification rather than resistance to oxidative damage. We also investigate the identity of the PTMs caused by irradiation of HγS and discuss future directions for investigation.

3.2 Materials and methods

3.2.1 Protein expression and purification

Human γS-crystallin (HγS) was produced using a construct containing an N-terminal 6× His tag and a TEV cleavage sequence (ENLFQG), which leaves a glycine in place of the initiator methionine. This gene was cloned into a pET28a(+) vector (Novagen, Darmstadt, Germany) and overexpressed in Rosetta (DE3) *E. coli* cells using Studier's autoinduction protocol [69]. Cell pellets were collected via centrifugation at 4,000 rpm for 30 minutes, resuspended, lysed, and respun at 14,000 rpm for 60 minutes. The protein was purified via nickel affinity chromatography, digestion with TEV protease (produced in-house), a second round of nickel affinity chromatography (to remove the cleaved His tag), and finally, size exclusion chromatography (SEC) on a GE Superdex 75 10/300 (GE Healthcare, Pittsburgh, PA). All samples were dialyzed into H_2O, lyophilized for storage at -80 °C, and resuspended in H_2O unless otherwise stated.

3.2.2 γ irradiation

Protein solutions at 5 mg/mL in water (100 μL) in glass vials were irradiated with a ^{137}Cs source (^{137}Cs Irradiator Mark-I, Model 68, JL Shepherd & Associates, San Fernando, California, USA). Sample concentration was determined from the absorbance at 280 nm using an extinction coefficient of 42,860 M^{-1} cm^{-1}. Post-exposure concentrations were calculated from the final volume after sample dilution or concentration using 5 mg/mL as the known starting concentration. A metal sample holder was used to maintain consistent sample distance from the source. The dose rate has been previously calibrated with Fricke dosimetry [144, 145]. Fricke dosimetry was used to confirm the expected dose for our sample position, volume, and vials [146]. Solutions of 0.4 M sulfuric acid, 6 mM ammonium ferrous sulfate and 1 mM potassium chloride were well-agitated for aeration and irradiated for 5 and 10 minutes. The absorbance at 304 nm was measured and the dose was calculated using a G-value of 15.5 mol/100 eV, extinction coefficient of 2022 M^{-1} cm^{-1}, a density of 1.024 g mL^{-1} and a path length of 1 cm [147]. The calculated dose rate at our sample position was 1.54 kGy/hr, matching the expected dose rate. Unless otherwise noted, all data were collected within 12 h of removal from the γ irradiation source.

3.2.3 Ultraviolet (UV) irradiation

For both UVA and UVB exposure, protein solutions were 6 mg/mL in 10 mM HEPES, 50 mM NaCl, pH 7. Sample volume was 2.5 mL in a 1 cm $\times$ 1 cm quartz cuvette. Samples were continuously stirred and temperature controlled at 22 °C using a Quantum Northwest Luma 40/Eclipse with a Peltier element and recirculator (Quantum Northwest Inc., Liberty Lake, WA, USA). For UVA exposure, a 10 Hz Nd:YAG laser (Continuum Surelite II; Surelite, San Jose, CA, USA) was coupled to a Surelite Separation Package (SSP) 2A (Surelite) to change the pump laser wavelength (1064 nm) to 355 nm via third harmonic generation. The laser

flux was 29 mJ/cm^2 at 10 Hz. Samples were exposed for 180 min. For UVB exposure, a 70 mW light emitting diode (LEUVA66H70HF00, Seoul, Korea) at 5 mm distance (120 degree view angle) was used, yielding a mean power density of 58 mW/cm^2. Samples were exposed for 90 min.

3.2.4 SDS-PAGE

20 μL of protein was mixed with 20 μL of loading dye (62.5 mM Tris-HCl, 2% sodium dodecyl sulfate (SDS), 25% glycerol, 0.01% bromophenyl blue, pH 6.8). For reduced samples, 1 μL β-mercaptoethanol was added and samples were heated at 70 °C for 90 seconds. Samples were run on a 15% polyacrylamide gel at 180 V for 60 minutes and stained using Coomassie blue dye.

3.2.5 Ellman's assay

To evaluate the amount of solvent-exposed thiols in solution, the non-irradiated and irradiated protein solutions were diluted to 0.5 mg/mL in 100 mM Tris pH 8.0. 5,5′-dithiobis(2-nitrobenzoic acid) (DTNB) was added to reach a final concentration of 0.1 mM. The solutions were incubated at room temperature for 30 minutes before collection of spectra on a Jasco V-730 spectrophotometer (JASCO, Easton, MD). A molar extinction coefficient for thiobis(2-nitrobenzoic acid) (TNB) of 14150 M^{-1} cm^{-1} was used to calculate the concentration of sulfhydryl groups [148, 149].

3.2.6 Circular dichroism (CD)

Circular dichroism (CD) spectra were collected using a J-810 spectropolarimeter (JASCO, Easton, MD). Spectral bandwidth was set to 2 nm. All samples were diluted to 0.1 mg/mL.

3.2.7 Intrinsic fluorescence

Fluorescence spectra were measured using an Agilent Cary Eclipse fluorescence spectrophotometer with excitation at 295 nm. All samples were diluted to 0.1 mg/mL.

3.2.8 Raman

Raman studies were perform using a Raman microscope system based on a Renishaw InVia microscope. The sample was excited with a 532 nm laser (>3 mW) and spectra were collected using grating of 2400 gr/mm and under 20 s exposure time. Sample concentration was 100 mg/mL. 4 μL of sample was deposited on a glass slide and a spacer and glass coverslip was added to prevent dehydration.

3.2.9 Fourier-transform infrared spectroscopy (FTIR)

FTIR spectra of lyophilized protein samples were measured using a Jasco FT/IR-4700 (JASCO, Easton, MD) equipped with .in attenuated total reflection geometry fashion using ATR PRO ONE over the 400-4000 cm^{-1} range with 2 cm^{-1} resolution.

3.2.10 Proteolytic digestion

For samples exposed to γ-irradiation for 1 hour, digestion was performed on an aliquot of the water-soluble portion of the irradiated samples, as no significant pellet was observed upon centrifugation. For samples exposed to γ-irradiation for 5 hours as well as for the UV irradiated samples, the samples were centrifuged at 13,000 x g for 15 min and the water-insoluble fractions resolubilized in 8 M urea, 1 M ammonium bicarbonate pH 8.0. For trypsin digestion, the protein samples were denatured in 8 M urea, 1 M ammonium bicarbonate pH 8.0 for 1 h at 37 °C. The buffer was diluted or buffer exchanged to 1.6 M urea and trypsin was added in a 1:20 ratio. The digest was carried out overnight at 37 °C. Immediately prior to analysis, DTT was added to 10 mM and the sample was heated at 80 °C for 3 minutes. For pepsin digestion, the sample was exchanged into approximately 1% formic acid (pH 1.6) and pepsin was added in a 1:20 ratio. Samples were incubated at 37 °C for 2 hours.

3.2.11 Liquid chromatography - mass spectrometry (LC-MS)

Mass spectra were collected on a Waters Xevo XS-QTof using either a phenyl column for intact protein mass spectra or a C4 column for peptide digests. Buffer A was 0.1% formic acid in water. Buffer B was 100% acetonitrile. For the protein intact mass spectra, the flow rate was 0.2 mL/min with a gradient of 0% to 97% B over 1.5 min then 97% B for 0.5 min. For the peptide digest mass spectra, the flow rate was 0.3 mL/min with a gradient of 3% to 27% B over 24.0 min, a gradient of 27% to 90% B over 3.0 min, then 90% B for 0.5 min. Intact mass spectra were analyzed using MassLynx with MaxEnt1 used to deconvolute the spectra. Peptide digests were analyzed with BioPharmaLynx.

3.3 Results and discussion

HγS was irradiated in a ^{137}Cs γ source at 5 mg/mL in glass vials (Figure B.1). The samples are positioned equidistant in a ring around the sample source and the dose rate at this distance has been previously calibrated [145]. We confirmed our samples were receiving the expected dose using Fricke dosimetry (Figure B.1).

3.3.1 HγS resists unfolding after high doses of γ irradiation

We used circular dichroism (CD) spectroscopy and intrinsic tryptophan fluorescence to assess the extent of unfolding in irradiated HγS. We aimed to determine whether HγS undergoes structural changes after irradiation that may be linked to radiation-induced cataract. Both the CD and fluorescence measurements indicate that HγS is remarkably resistant to unfolding upon even prolonged γ irradiation.

The CD spectra of proteins exhibit characteristic bands that report on secondary structure [150]. Here we compare the CD spectra of non-irradiated HγS to irradiated samples to detect partial or complete unfolding. In previous studies of HγS, even small changes in secondary structure due to mutation or partial unfolding were observable, i.e. as frequency shifts and shoulders on the major peaks [85, 151]. For γ irradiated HγS, the CD spectra of all samples up to 10.8 kGy show a strong negative peak at 218 nm, which is characteristic of the primarily β-sheet structure of this protein (Figure 3.1A). At 33.9 kGy there is a loss of negative intensity at this position and broadening of the negative band toward 204 nm, where there is a new peak minimum. Similar shifting and broadening of the CD minimum at 218 nm was previously observed for γ-crystallins denatured with guanidine hydrochloride. [152] The same trend was observed for HγS that was aggregated through incubation with copper and resolubilized [35], as well as for UV-C irradiated, aggregated, and resolubilized HγD [153].

In a previous study of human αA- and αB- crystallin, molecular chaperone proteins that are also abundant in the lens, CD was used to monitor secondary structure as these proteins were subjected to increasing doses of γ irradiation. The secondary structures of αA- and αB-crystallin were disrupted at a dose of 3.0 kGy and 1.0 kGy of irradiation, respectively [154]. In contrast, here we show that the solubility and secondary structure of HγS is preserved up to at least 10.8 kGy.

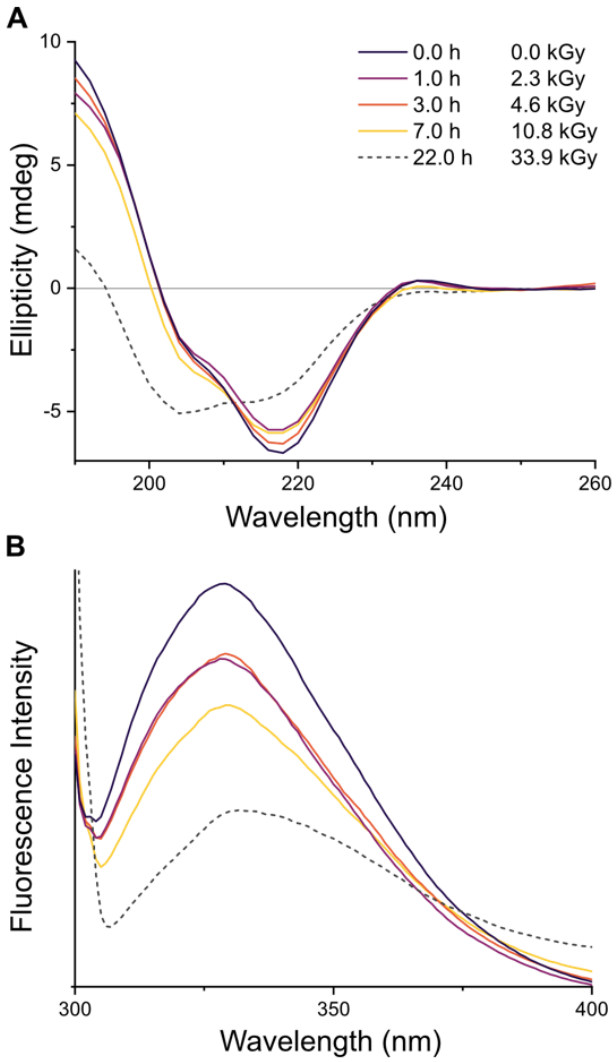

Figure 3.1: The structure of HγS was monitored using circular dichroism (CD) and intrinsic tryptophan fluorescence spectroscopy. (A) CD and (B) fluorescence spectra of HγS irradiated from 0 kGy (black), 2.3 kGy (purple) 4.6 kGy (orange), 10.8 kGy (yellow), 33.9 kGy (grey, dashed). HγS resists significant secondary structural rearrangement past 10.8 kGy.

For γ-crystallins in particular, intrinsic tryptophan fluorescence provides a nuanced view of the protein's folding state. Here we corroborated the CD results with fluorescence spectra collected over the same time course. The most obvious change in these spectra is the decrease in fluorescence intensity as irradiation increases. The arrangement of the buried tryptophans in the core of HγS has a powerful quenching effect on fluorescence; therefore, full denaturation typically increases the fluorescence signal [143]. However, other effects can alter tryptophan fluorescence intensity in the absence of full unfolding, such as transient contact with solvent molecules as a result of secondary structure destabilization [155] or modifications that alter the chemical structure of tryptophan such as conversion of tryptophan to kynurenine or other oxidation products [156].

The position of the emission maximum is more straightforward to interpret: previous work has shown shown that the fluorescence emission maximum of β- and γ-crystallins shifts from approximately 325 nm to 340 nm when the protein is fully denatured [157, 158]. Displacement of the typically buried tryptophans through denaturation exposes the residues to the more polar solvent, causing a redshift in fluorescence emission maxima upon excitation at 295 nm [159]. Partial unfolding or increased molecular motions increase the solvent accessibility of the tryptophans, leading to shifts in the spectra of a few nm [85]. The fluorescence maximum of HγS remains at 329 nm, consistent with a fully folded protein, through 10.8 kGy of irradiation (Figure 3.1B). After 33.9 kGy, the peak shifts from 329 to 332 nm. The CD spectra and fluorescence data both indicate that the structure of HγS is unperturbed past 10.8 kGy of γ irradiation.

3.3.2 Human γS-crystallin accumulates mass modifications after γ irradiation

Chemical alteration of crystallins has previously been observed after aging as well as exposure to UV light and lens contaminants such as metal cations. The best-characterized PTM of structural crystallins is deamidation [44, 46], which lowers stability and alters dynamics, potentially generating aggregation-prone transient conformations [54, 160]. Oxidation is another common PTM, particularly in aged lenses that have reduced antioxidant levels. Residues that are particularly vulnerable to oxidation include cysteine, methionine, histidine, and tryptophan [10, 33]. ROS formation in the lens can result from exposure to light in the UVA [161] or UVB [162] parts of the solar spectrum. Damage to biomolecules can also be caused by Fenton chemistry, where hydrogen peroxide induces redox cycling of certain metal ions (canonically, Fe^{2+} to Fe^{3+}, but also Cu^{+} to Cu^{2+}), forming hydroxyl radical and other highly reactive species [163–166].

Despite its remarkable resistance to unfolding, HγS accumulates many mass modifications from γ irradiation. Intact mass spectra were obtained to determine if any modifications to the protein mass occurred during irradiation (Figure 3.2). HγS has an expected intact mass of 20932 Da, which appeared in the purified protein spectrum shown in Figure 3.2 (top). During irradiation, a number of mass modifications accumulated that led to both increases and losses in mass. Mass increases appear to be mostly due to oxidations, with successive increases of +16 Da, consistent with multiple oxidations on the same protein molecule.

Specific amino acids have been shown to be highly susceptible to oxidation in the presence of ROS. The sulfur-containing amino acids cysteine and methionine are known to form various oxidation states including sulfenic, sulfinic and sulfonic acids for cysteines and methionine sulphoxide for methionine [34, 167]. Disulfide bonds are also likely to form under oxidizing conditions [34]. To detect the presence of free thiols in non-irradiated and irradiated samples,

we performed Ellman's assay. Ellman's assay utilizes the reaction of cysteines with 5,5'-dithiobis-(2-nitrobenzoic acid) (DTNB) to quantify the free thiols [148, 149]. This assay was performed under nondenaturing conditions to assess the amounts of solvent-exposed thiols in solution. Figure 3.3 shows the non-irradiated sample, which has a free thiol content of 41 μM. This corresponds to 3.4 solvent-exposed thiols per protein molecule, consistent with structural analysis of the NMR and crystal structures of HγS that indicate 3 out of the 7 cysteines are highly solvent-exposed [64, 82]. With increasing γ irradiation dose, the solvent-exposed thiol concentration decreased to 16, 13 and 9 μM after 1.5, 3.0, and 7.0 h, respectively. These concentrations correspond to 1.4, 1.1 and 0.7 solvent-exposed thiols per protein molecule for the 1.5, 3.0, and 7.0 h irradiated samples, respectively.

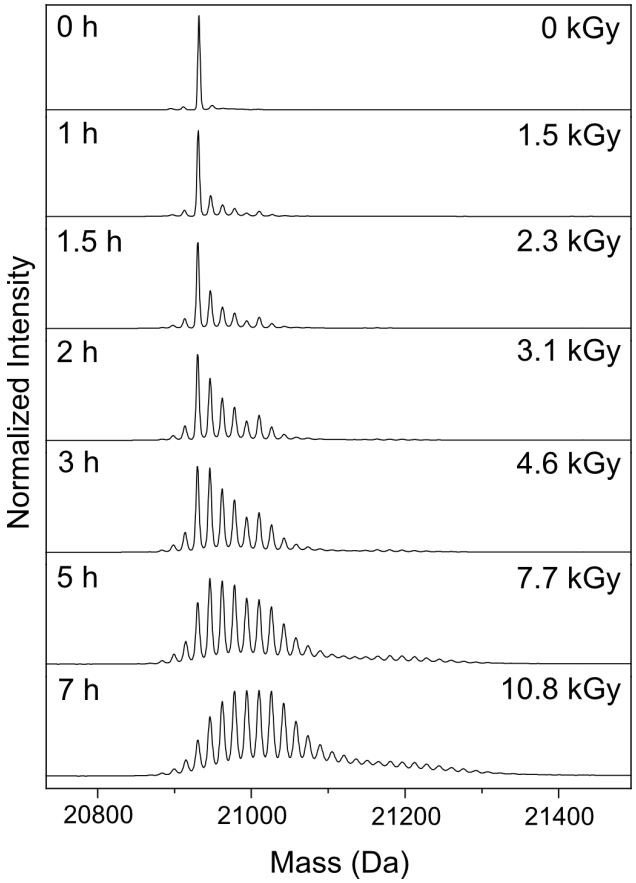

Figure 3.2: Deconvoluted intact mass spectra HγS samples irradiated with doses (0, 1.5, 2.3, 3.1, 4.6, 7.7, and 10.8 kGy) of γ radiation. HγS accumulates successive +16 Da and -16/-17 Da modifications over the course of irradiation.

In general, protein oxidation via ROS has been extensively reviewed [168]. The side chains of lysine, histidine, tyrosine, tryptophan, and phenylalanine are likely targets for addition reactions: lysine residues oxidize to aminoadipic semialdehydes [169]; histidine oxidizes to asparagine, aspartic acid, and oxo-histidine [169, 170]; tryptophan converts to 2-,4-,5-,6-, and 7-hydroxy-tryptophan, formylkynurenine, 3- hydroxykynurenine, and kynurenine [171]; tyrosine forms 3,4-dihydroxyphenylalanine or dityrosine crosslinks [171]; and the oxidation products of phenylalanine are 2-,3-, and 4-hydroxyphenylalanine and 3,4- dihydroxyphenylalanine [171]. Oxidation patterns induced by hydroxyl radicals are well-characterized and predictable, leading to their use in oxidative-based footprinting methods [172]. This technique exposes proteins to hydroxyl radicals that oxidize amino acid side chains at a rate determined by solvent exposure. Side chains that are buried or involved in protein-protein interactions can be identified by their resistance to oxidation [173]. This type of footprinting is particularly useful when fast, laser-induced hydroxyl radical production is combined with modern mass spectrometry detection methods [174], a strategy that has been used to characterize protein-peptide [175] and antibody-epitope binding [176], among others. We expected to observe similar patterns of oxidation as γ irradiation produces hydroxyl radicals.

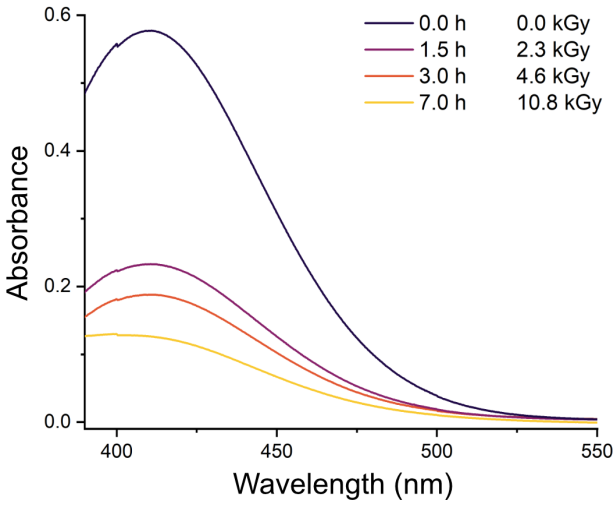

Figure 3.3: Absorbance spectra of non-irradiated and irradiated samples after reaction with Ellman's reagent, DTNB. The absorbance at 412 nm was used to calculate the concentration of free thiols.

In addition to the expected oxidations, the intact mass spectra of the γ irradiated protein also indicate the presence of other modifications. We noted a spike at the 5× oxidation state (+80); we hypothesize that an additional mass change may add +80 Da that overlaps with the 5× oxidation state. Another possibility suggested by other known PTMs is O-sulfation on serine, threonine, or tyrosine residues, although the source of SO_3 is unknown in that case [177, 178]. We also observed mass losses in the irradiated samples. The resolution of the intact mass spectra makes it difficult to determine within 1 Da the exact mass of this shift; however, it appears to fall between -16 to -17 Da. There appears to be a succession of mass losses, with an apparent 1× mass loss at -16/-17 and 2× mass loss at -33/34. The loss of 17 Da may correspond to the formation of succinimide via a sidechain nucleophilic attack on the protein backbone. Succinimide formation is readily achieved by aspartic acid which can then racemize to D-aspartic acid [179], a common PTM in aged lenses [180]. Succinimide formation has been shown to increase in UVC irradiated α-crystallins [181]. The amount of β-linked aspartic acid, which is also formed through a succinimide intermediate, has been shown to increase in γ irradiated α-crystallins [182]. However, other modifications may overlap as well. For example, dehydroalanine formation from cysteine generates a -34 Da mass loss from the conversion of the thiol group to an olefin and has been detected as a product of protein-ROS interaction using MS/MS [183].

In this study, we focused on the short-term mass changes and structural stability of HγS by analyzing all samples within hours of removal from the γ-irradiation source. However, intact mass spectra collected from later time points (immediately after irradiation compared to 4 hours after irradiation and 1 week after irradiation) show an increase in the amount of modified protein (Figure B.2). We hypothesize that γ radiation generated ROS continue to react with the protein after removal from the energy source, consistent with previous reports that these intermediates last hours to days [168, 184].

3.3.3 Oxidative damage was identified on Lys, Met, Trp, Leu, and Cys

To identify the modifications, samples irradiated for 1 h/1.5 kGy were digested and analyzed with liquid chromatography tandem mass spectrometry (LC-MS/MS). This type of data-independent acquisition (DIA) allows for a less biased approach as all peptides are included in the analysis. Protein digestion was performed by proteolysis with both trypsin and pepsin on the 1.5 kGy dose samples. Trypsin digestion was performed under denaturing conditions, with the protein first incubated in 8 M urea for 1 h then diluted to 1.6 M urea for an overnight incubation with trypsin. A pepsin digest was added to increase coverage [185]. Both the trypsin and pepsin digests from 1.5 kGy samples mostly lacked distinct, identifiable peptides in the irradiated sample. This result was unexpected based on the modifications observed in the intact mass spectra of the irradiated samples. One modification was identified from the pepsin digest of the 1.5 kGy irradiated sample, the peptide GSKTGTKIF showing a -1 Da loss (Table 3.1). The b and y ion plots show that the location of the mass shift is in the first three residues (Figure B.3). Of the three residues, lysine is the mostly likely target of oxidation. Aminoadipic semialdehyde derivatives of lysine resides are known oxidation products of lysine that yield a -1 Da loss [186]. This modification has been reported in crystallins in aged human eye lens, where its concentration increased with age and in the presence of diabetes, both conditions which increase cataract susceptibility [187]. The semialdehyde has been reported to further oxidize to the carboxylic acid derivative, 2-aminoadipic acid [187].

The lack of unique peptides in the 1.5 kGy irradiated sample digest suggested that the modifications to HγS as a result of γ irradiation were so heterogeneous that each modified peptide has a very low individual signal, making identification of any particular species by mass spectrometry difficult. We therefore looked to increase the signal for the modified peptides by analyzing samples with longer irradiation times, 5 hours with a dose of 7.7 kGy. Addition-

ally, we analyzed the precipitated fraction (which was not evident in the 1.5 kGy samples) in order to observe an increased fraction of modified peptides. The water-insoluble fraction was resolubilized in denaturing buffer and subsequently digested with trypsin. Enriching the sample for modified proteins aided in identifying the sites of oxidation from radiation exposure. It should be noted that accurately measuring concentration post-exposure using UV absorption is challenging, as the UV absorption profile can change significantly due to the oxidation of the aromatic amino acids. Therefore, a direct comparison of ion count of the modified peptides between samples is not feasible as the total sample concentration may vary. In order to give an approximation of the relative amount of modified peptides between samples, we estimated the percent abundance as the ion count of the modified peptide over the total ion count of all the modified and unmodified forms of the peptide.

Table 3.1 summarizes the sites of oxidation identified in 7.7 kGy irradiated HγS. We found evidence of oxidation on all methionine residues and one of the four tryptophan residues. We also identified oxidation of one cysteine, C25, consistent with the high solvent exposure of this residue. The b and y ion plots supporting the identified oxidation sites are shown in the Supplementary Information. The methionine residues and W163 each show a single oxidation, with b and/or y ions demonstrating the specific position of the +16 mass addition (Figure B.4-B.9). We also found evidence of oxidation of leucine, with +16 mass addition to L142 (Figure B.10). L133 may also be oxidized, however the b and y ions were not definitive to that position, as the +16 may also added to V132 (Figure B.11). Both leucine and valine have previously been reported to form hydroperoxides and hydroxides in the presence of hydroxyl radicals and oxygen [167]. γ irradiation on a leucine-containing small peptide resulted in the formation of 4-hydroxyleucine with a +16 mass addition as a major product [188]. In contrast to the single oxidations identified for the other residues, C25 was identified as a doubly oxidized species, forming the sulfinic acid derivative. The b and y ions definitively identified C25 as doubly oxidized, rather than a single oxidation of C25 and a neighboring cysteine (Figure B.12). Oxidation of methionine, tryptophan, and cysteine

residues is consistent with the oxidation sites found in γE and γF in rat lenses exposed to γ irradiation [132].

For comparison, we additionally irradiated HγS with ultraviolet (UV) radiation to determine whether similar products formed. UV radiation has been shown to directly photo-oxidize proteins via absorption by the major chromophoric side chains (Trp, Tyr, Phe, His, and Cys), which in turn may generate ROS and subsequently oxidize other side chains [189, 190]. UV irradiation of bovine α-crystallin [181, 191] and human γD (HγD) crystallin [153, 192] showed oxidation of methionine, tryptophan, and cysteine residues. UVA and UVB irradiation of HγS-crystallin has previously been shown to lead to rapid formation of light-scattering, amorphous aggregates *in vitro* [35]. We performed trypsin digests on the insoluble fractions after UVA and UVB irradiation. The UV-irradiated samples show a similar pattern of oxidized amino acids, with methionines, tryptophans, and cysteines identified as oxidized products (Table 3.1). UV irradiated samples additionally showed that C23 and C27 formed sulfinic acid derivatives with +32 mass shifts (Figure B.13 and B.14). Previous studies on UV irradiated HγD report the formation of double and triple oxidized cysteines, rather than the single oxidation product [192].

3.3.4 Vibrational spectroscopy reveals chemical signatures of oxidation

Infrared (IR) and Raman spectroscopy were used to gain further insight into the types of PTMs arising from γ irradiation. Both techniques are powerful approaches for directly probing vibrational signatures, and hence chemical content, of the molecules. IR spectra were collected on the non-irradiated and irradiated samples in the mid-IR region on lyophilized protein to minimize the background signal from water. Several distinct features appeared in irradiated samples (Figure 3.4). We noted that a peak appears at a wavelength of 2835 cm^{-1}

Table 3.1: Oxidation sites identified in γ and UV irradiated HγS. Peptides from pepsin and trypsin digests were separated and identified via LC-MS/MS. The percent abundance is calculated from the ion count of the modified peptide over the total ion count of all modified and unmodified forms of the peptide. No data is available on the presence of the $K3^{-1}$ modification of GSKTGTKIF as pepsin digests were not performed for the 7.7 kGy γ irradiated or UV irradiated samples. The unmodified form of GSKTGTKIF was not detected; therefore, percent abundance is not reported.

nd = not detected
[a]percentage not reported as unmodified peptide not detected
[b]assignment of oxidation to specific residue not definitive

Residue	**Peptide**	**Modification**	**Nonirradiated**	**γ-rays**		**UV**	
				1.5 kGy	7.7 kGy	UVA	UVB
1-10	GSKTGTKITF	$K3^{-1}$	nd	detected[a,b]	-	-	-
42-72	VEGGTWAVYERPNFAGYMYILPQGEYPEYQR	$M59^{+16}$	nd	nd	16%	8%	14%
73-79	WMGLNDR	$M74^{+16}$	nd	nd	3%	2%	3%
102-125	GDFSGQMYETTEDCPSIMEQFHMR	$M108^{+16}$	nd	nd	5%	7%	10%
		$M119^{+16}$	nd	nd	8%	11%	11%
		$M124^{+16}$	nd	nd	2%	6%	9%
132-146	VLEGVWIFYELPNYR	$V132^{+16}$ or $L133^{+16}$	nd	nd	1%[b]	nd	nd
		$L142^{+16}$	nd	nd	< 1%	nd	nd
159-174	KPIDWGAASPAVQSFR	$W163^{+16}$	nd	nd	< 1%	< 1%	< 1%
20-36	RYDCDCDCADFHTYLSR	$C23^{+32}$	nd	nd	nd	2%	3%
		$C25^{+32}$	nd	nd	1%	4%	8%
		$C27^{+32}$	nd	nd	nd	< 1%	1%

after long irradiation times. This peak was preliminarily assigned to the C–H stretch mode of aldehydes [193]. The increase in this region in irradiated samples is consistent with the modified peptide with an aldehyde derivative of lysine identified from the mass spectrometry data. New peaks also appeared at 1373 and 1258 cm^{-1} in the spectra of irradiated samples, consistent with double bonds between sulfur and oxygen, which have a stretching mode in the 1372-1335 cm^{-1} range [193]. These data support the presence of oxidized cysteines and methionines identified via mass spectrometry (Table 3.1). The peak at 1258 cm^{-1} may arise from the C–O stretching mode of carbonyl-containing functional groups [193]. Carbonyl derivatives are commonly reported in oxidized proteins and carbonyl content has been used as an indicator of oxidative stress [194, 195].

Raman spectroscopy was also performed on a custom-modified Raman microscopy system [196]. Protein lines of particular interest are not strong in intensity compared to other signals within the molecular fingerprint region. To clearly observe the associated lines and changes, high concentration samples deposited on glass slides were used [197]. Due to the high protein concentration required, we first evaluated the effects of protein concentration on the modification rate from γ irradiation. We used a commercially available protein, hen egg white lysozyme, due to the significant sample consumption for high concentration samples. We obtained a non-irradiated intact mass spectrum for lysozyme, which is shown in Figure B.15. We then irradiated lysozyme samples both at 5 mg/mL and 100 mg/mL for 1 h to a dose of 1.5 kGy and collected intact mass spectra. Figure B.15 shows the lower concentration sample contains a much higher percentage of modified protein, consistent with ROS derived from water rather than direct irradiation of the protein causing most of the damage. We therefore chose to irradiate the HγS sample at 5 mg/mL then concentrate to 100 mg/mL for Raman data collection to maintain sample consistency between techniques.

Other reports suggest that γ irradiation may form protein peroxides, which are detectable in Raman spectra [198, 199]. The HγS samples were irradiated at 5 mg/mL then concentrated

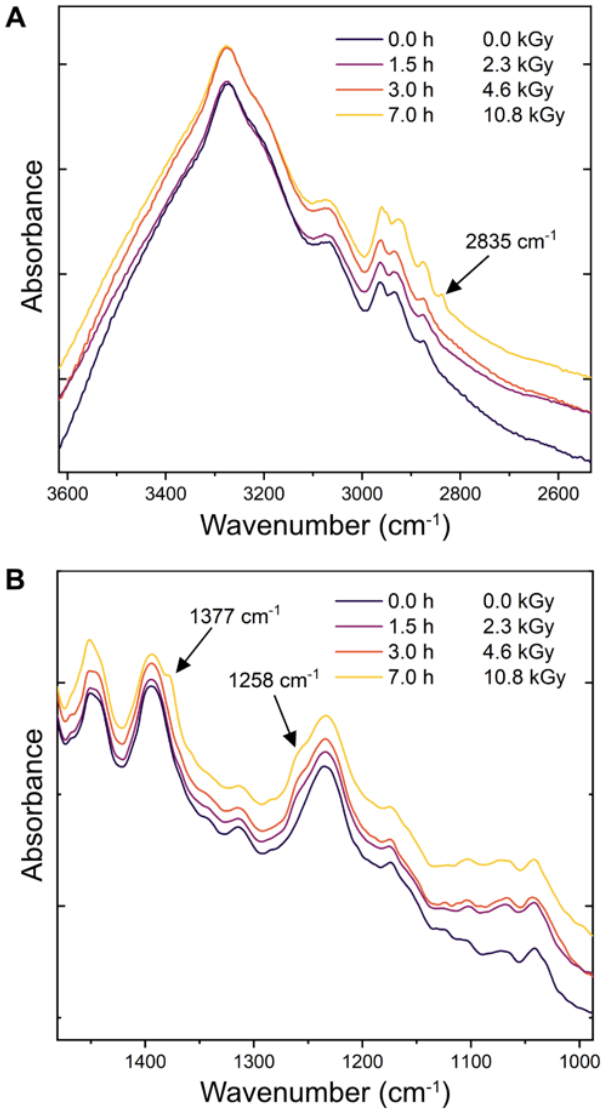

Figure 3.4: IR spectra for samples irradiated from 0.0 to 10.8 kGy from (A) 3655 to 2520 cm^{-1} and (B) 1480 to 990 cm^{-1}. Traces are offset for clarity. Unique peaks that appear after irradiation are indicated with an arrow.

with centrifugal concentrators immediately after irradiation to reach 100 mg/mL for spectra measurement. The spectra of non-irradiated sample and sample irradiated for 1.5 h/2.3 kGy is shown in Figure 3.5. No significant spectral changes were noted at this dose. However, we were unable to collect Raman spectra from samples with longer irradiation times due to an increase in background fluorescence. We measured this fluorescence signal at the excitation wavelength of 532 nm to determine the emission profile for the unknown fluorophore (Figure

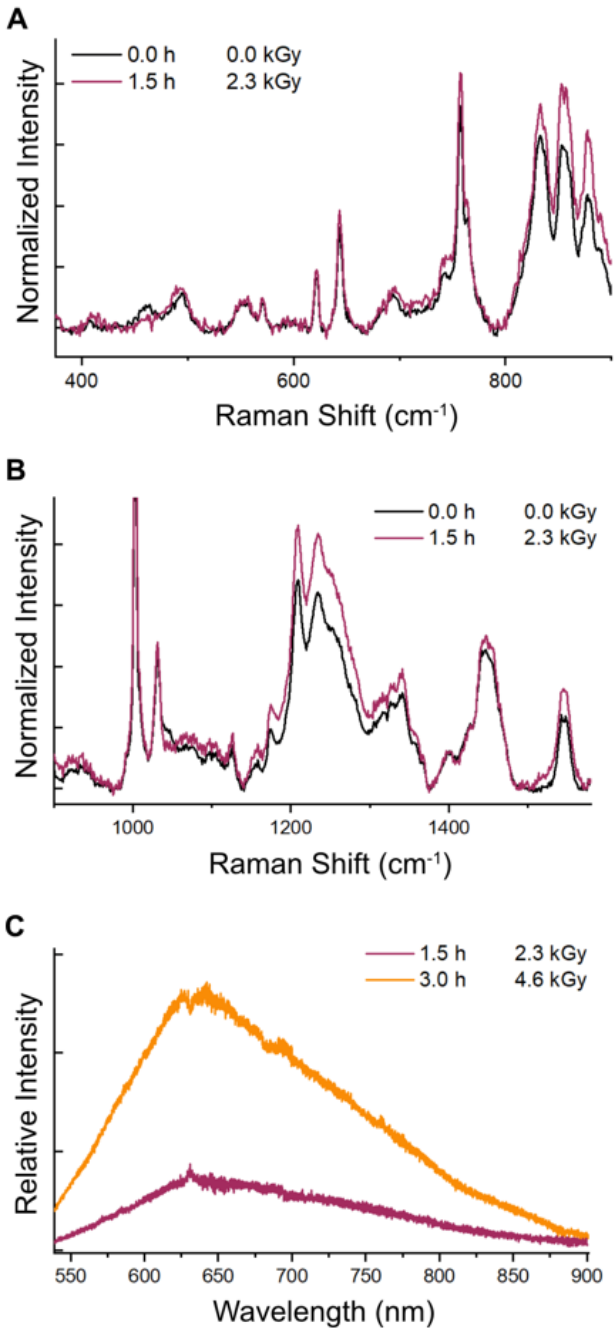

Figure 3.5: Raman spectra of non-irradiated and irradiated HγS from (A) 375 to 900 cm^{-1} and (B) 900 to 1580 cm^{-1}. No significant spectral changes are observed from 1 h/1.5 kGy dose. (C) Fluorescence spectra of irradiated HγS with an excitation wavelength of 532 nm.

3.5) To our knowledge, an amino acid derivative with this excitation-emission profile has not been reported. We aim to identify the unknown fluorescent product via further mass spectrometry analysis.

3.3.5 γ irradiation causes non-disulfide covalent cross-linking

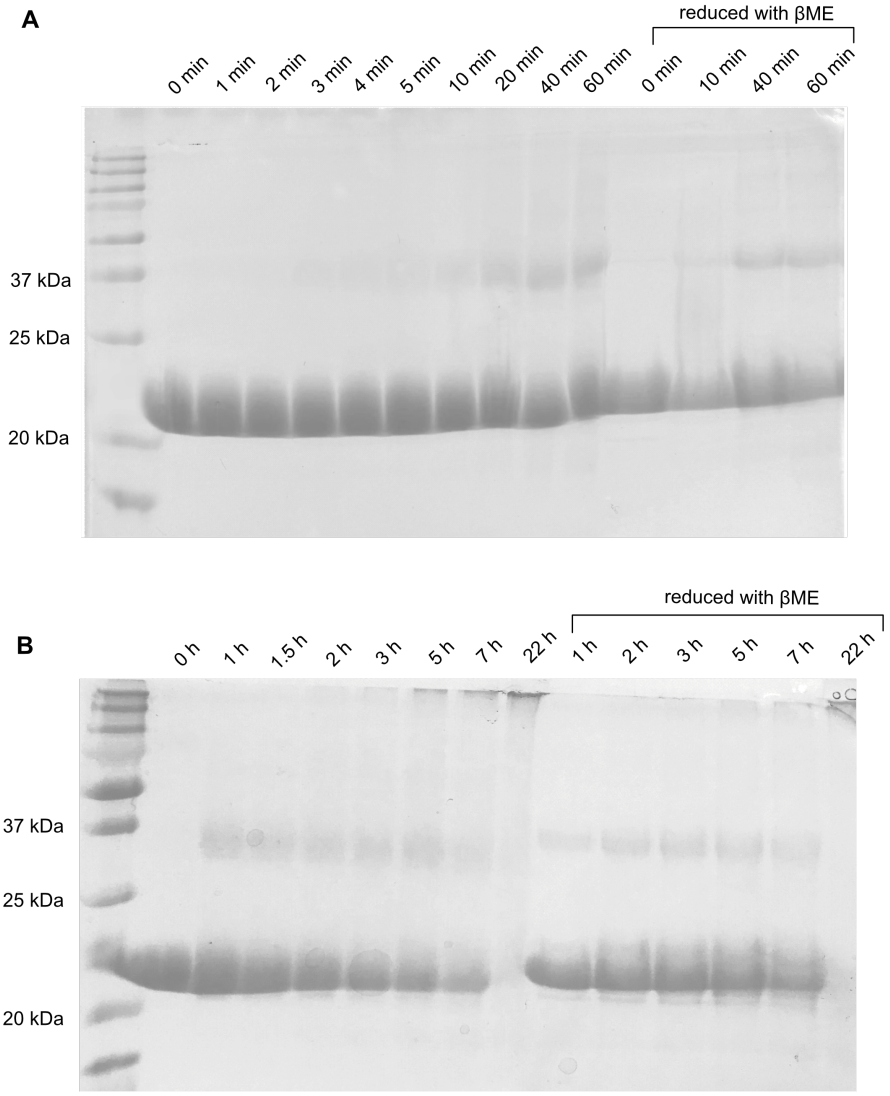

Figure 3.6: SDS-PAGE analysis of non-irradiated and irradiated HγS. (A) Short γ irradiation exposures from 0 to 60 min, up to 1.5 kGy. A dimer of HγS forms that resists reduction with βME. (B) Longer γ irradiation exposures from 0 to 22 h, up to 33.9 kGy. Aggregation appears to increase with longer irradiation times with no remaining monomer or dimer visible at 22 h.

In addition to the side-chain modifications noted in the previous section, γ irradiation appears to lead to chemical cross-linking between protein molecules. Figure 3.6 shows an SDS-PAGE of non-irradiated HγS as well as up to 1 h of irradiation or 1.5 kGy. The gels

were intentionally overloaded to increase the visibility of the dimer band. During the course of irradiation, a dimer forms corresponding to approximately 40 kDa. The dimer mass is also seen in the intact mass spectra (Figure B.16). HγS is known to form disulfide-bonded dimers, usually between the solvent exposed C25s in two HγS molecules. However, the dimers formed after γ irradiation resisted reduction with β-mercaptoethanol (βME), suggesting that these dimers were formed via an alternative cross-linking mechanism. Several crosslinks have been identified in aged and cataractous lenses [200]. Asp/Asn-Lys [201], dityrosine [202], Glu/Gln-Lys [47] have all been identified in human lenses. Dityrosine cross-linking proceeds through a radical mechanism [203] that could be promoted by irradiation and interaction with hydroxyl radical.

Longer irradiation times led to protein aggregation; however, fragmentation was not noted in either the SDS-PAGE analysis or the intact mass spectra. Figure 3.6 shows the SDS-PAGE of the non-irradiated protein and the irradiated protein from 1 h to 22 h. The bands for both the monomer and dimer decrease in intensity over the course of irradiation, while the band at the loading well grows more intense, suggesting that full-length protein is aggregating and no longer able to travel down the gel. By 22 h, no bands are visible in the expected mass ranges for either monomer or dimer. Neither the dimer bands nor the aggregation bands in the loading well are disrupted by reduction with βME, confirming that disulfide bonding is not the main mechanism of crosslink formation.

3.4 Conclusion

Long-lived proteins such as lens crystallins, which have evolved to maintain a stable structure for decades, are particularly vulnerable to the accumulation of detrimental modifications because they are not replenished during the human lifetime. Exposure to ionizing radiation would be expected to cause rapid protein aggregation via the large number of diverse

PTMs. Remarkably, despite acquiring many modifications from exposure to γ radiation, HγS-crystallin appears to be resistant to denaturation up to very high doses. Our results clearly confirm the high tolerance for chemical modification of the γ-crystallins, highlighting their evolutionary adaptation as resilient proteins. The present study was mainly focused on the short-term structural stability of irradiated HγS. However, because cataracts often manifest many years after damage occurs, future studies should also focus on long-term structural stability.

Chapter 4

A simple vapor-diffusion method enables protein crystallization inside the HARE serial crystallography chip

4.1 Introduction

X-ray crystallography has contributed dramatically to our current understanding of biomolecular processes. The obtained protein structures, however, only capture one static moment in a dynamic system as most data were collected at cryogenic temperatures. While this technique limits radiation damage, experiments on non-frozen samples with native ligands are essential for a deeper understanding of protein structural dynamics and chemical activity. Exploiting this opportunity, recent developments in serial crystallography now allow the study of structural changes during a reaction cycle [204]. In serial crystallography, diffraction patterns are collected from many crystals, often thousands, and data are indexed and merged for protein structure solution [205]. These developments have been triggered by increased

source brightness at X-ray free electron lasers (XFELs) and 3rd/4th generation synchrotrons, as well as advances in beam micro-focusing, allowing the X-ray exposure time per crystal to be drastically reduced and experiments to be carried out on smaller crystals. With serial data collection strategies, dose accumulation is mitigated, and room temperature measurements become viable. In addition to time-resolved applications, serial crystallography promises to be particularly useful for systems for which the growth of a large single crystal remains difficult, such as many membrane proteins or intracellularly grown protein crystals [206, 207]. Serial data-collection has enabled significant developments in time-resolved crystallography using both XFELs [208–211] and synchrotron sources [212–215] as these typically require data collection on non-frozen samples. Additionally, crystals in the micrometer size regime are required for more homogeneous reaction initiation throughout the crystal for both optical excitation and *in situ* mixing.

The need for rapid exchange of crystals in the beam path, in order to collect thousands of diffraction images in a practical timeframe, has advanced new methods of sample delivery including both injection-based and fixed-target approaches. [216, 217]. For the ultrafast timescales accessible with XFELs, injection methods have been used with the most success [204, 205, 208, 218]. However, fixed-target sample delivery offers the distinct advantages of comparably low sample consumption, high hit rates, and access to longer and more versatile time delays [212, 219–224]. Moreover, fixed-target SFX is ideally suited for efficient *in cellulo* diffraction data collection using living, crystal-containing cells, as recently demonstrated by Lahey-Rudolph *et al.* [225]. Crystallization of recombinant proteins in living cells is an exciting new approach particularly important for proteins that were/are not accessible for crystallization using established in vitro screening strategies, as shown for *T. brucei* IMPDH and fully glycosylated *T. brucei* CatB [206, 207]. High-resolution structural information on several recombinant proteins has already been obtained from diffraction of *in cellulo* crystals [226]. In this study, we use the previously described HARE-chip ('hit-and-return') design that allows for precisely defined crystal locations. These lithographically fabricated

silicon chips hold the microcrystals in random orientations in inverted pyramidal bottomless wells, also called features [220, 221, 227]. The HARE-chips are mountable on high-speed translation stages that enable a rapid exchange of crystals through the beam path, for routine data collection rates of ∼30 Hz, although higher rates up to ∼100 Hz have been achieved with these stages [212, 224]. The HARE-chip design is integral to efficient time-resolved data collection via the 'hit-and-return' (HARE) method, in which the time delays are mechanically set through movement of the stages to precise crystal positions. This enables efficient data collection for short (milliseconds) and long (seconds to minutes) time delays [212, 227]. Reaction initiation via optical excitation as well as *in situ* mixing have been demonstrated for reactions on millisecond to minute timescales [212–214].

In general, the challenge of efficient crystal loading remains for fixed-target approaches. In previous studies using the HARE-chip design, the proteins were first crystallized in batch and subsequently the crystal slurry was transferred to the chip [212, 214, 221, 223, 227–232]. Although the generation of micro-crystals based on canonical vapor diffusion conditions is greatly simplified by our vacuum-crystallization procedure, large-scale batch crystallization can still be challenging, including potentially time- and protein-consuming screening and optimization [233, 234]. Recently, on-chip crystallization was demonstrated for the Roadrunner chip. However, because the features lack concavity, crystals are distributed in random locations on the chips' surface and this preparation is therefore not easily adaptable to the HARE data collection method for time-resolved applications as the time delays are achieved by the periodic spacing of the crystals. Additionally, the high speed movement of the stages might shifting of the crystal positions on a flat surface, impeding the return to a particular crystal at a set time delay [212, 227, 235].

To overcome these challenges, we sought for a solution that would a) further reduce the amount of protein sample required, b) minimize the physical stress on the crystals, while maintaining compatibility with time-resolved data collection via the HARE method and

c) streamline the transition from a canonical vapor diffusion crystallization condition to a micro-crystallization condition suitable for serial crystallography.

Here we demonstrate an *in situ* crystallization method in which the crystals are directly grown within <1 nL volume of the HARE-chip wells. This method eliminates virtually all crystal handling and also drastically reduces protein consumption. Initially three model systems were crystallized inside the features of the chip: lysozyme, proteinase K, and xylose isomerase. To test this method with a challenging crystallization target we used a novel variant of the human eye lens protein, γS-crystallin, a class of proteins which are notoriously hard to crystallize. To further emphasize the reduction of physical stress on the microcrystals, *in situ* crystallization was explored with the fungal protein HEX-1, which grows micro-crystals in insect cells directly cultured on the HARE-chip. HARE-chips enabled fast and efficient diffraction data collection from *in cellulo* protein crystals in living cells at a synchrotron source. Room-temperature, serial X-ray crystallography structures were successfully determined for all five systems.

4.2 Materials and methods

4.2.1 Protein preparation and crystallization

Lysozyme

Lysozyme from chicken egg white was purchased from Sigma (L6876). The lyophilized powder was dissolved to 65 mg/ml in 50 mM sodium acetate pH 4.7. 5 µl of protein solution was mixed with 5 µl of precipitant solution (33% PEG 4000, 0.5 M NaCl, 50 mM sodium acetate pH 4.5) prior to deposition on the chip.

Proteinase K

Proteinase K from *Tritirachium album* was purchased from Sigma (P6556). The lyophilized powder was dissolved to 60 mg/ml in 50 mM HEPES pH 7.0. 5 µl of protein solution was mixed with 5 µl of precipitant solution (1 M NaNO3, 0.1 M sodium citrate pH 6.5) prior to deposition on the chip.

Xylose isomerase

Xylose isomerase from *Streptomyces rubiginosus* was purchased from Hampton Research (HR7-102) and stored for several years. The stock crystals were dissolved in water, washed repeatedly in a concentrator to exchange the storage buffer, and concentrated to 80 mg/ml. 5 µl of protein solution was mixed with 5 µl of precipitant solution (35% (w/v) PEG3350, 200 mM lithium sulfate and 10 mM Hepes/NaOH, pH 7.5) prior to deposition on the chip.

Human γS-crystallin variant

The human γS-crystallin variant (N15D/Q121E/N144D/N54D/Q93E/Q64E/Q17E/Q107E/Q71E) was created using site-directed mutagenesis PCR from the wild-type construct with an N-terminal 6x-His tag and a tobacco etch virus (TEV) protease cleavage sequence. *Escherichia coli* Rosetta (DE3) cells were transformed with a pET28a(+) vector (Novagen, Darmstadt, Germany) containing the human γS-crystallin variant cDNA. Overexpression was achieved using Studier's autoinduction protocol [69] for 1 hour at 37 °C followed by 20-24 h at 25 °C. The cells were lysed via sonication and supernatant of the lysate loaded on to a Ni-NTA column (Applied Biosystems, Foster City, CA, USA). The tagged protein was eluted using imidazole and the tag cleaved by TEV protease (produced in-house). The protein and tag were separated by reapplication to the Ni-NTA column. A final size exclu-

sion purification was performed on a HiLoad 16/600 Superdex 75 pg column (GE Healthcare Life Sciences, Piscataway, NJ, USA). The protein was lyophilized for storage, then resolubilized and buffer exchanged into 50 mM HEPES pH 7.0 and 5 mM DTT, concentrated to 20 mg/ml, and stored at 4 ℃ for several months. 5 µl of protein solution, diluted to 11 mg/mL in 50 mM HEPES pH 7.0, was mixed with 5 µl of precipitant solution (20% (w/v) PEG3350, 0.1 M sodium acetate pH 5.45) prior to deposition on the chip.

HEX-1

Cloning of the HEX-1 gene (GenBank vaccession No. XM_958614) from the filamentous fungus *Neurospora crassa* has been described previously [225]. In brief, the HEX-1 coding sequence was amplified using the primers 50-TACTACGACGACGACGXT CACG-30 (sense) and 50-GAGGCGGGAACCGTGGACG-30 (antisense) and blunt end-ligated into the EheI site of a pFastBac1 vector containing the sequence 50-ATGGGCG CCTAA-30 between the BamHI and HindIII restriction sites. For baculovirus production, recombinant bacmid DNA was generated in *E. coli* DH10EmBacY cells (Geneva Biotech) and used for lipofection of *Spodoptera frugiperda* Sf9 insect cells. The virus titer was calculated using the $TCID_50$ (tissue-culture infectious dose) in a serial dilution assay as described previously [225]. Intracellular crystallization of HEX-1 was achieved by infecting 9 × 105 *Trichoplusia ni* High Five insect cells with the Hex-1-encoding recombinant baculovirus (rBV) in a well of a six-well cell-culture plate in 2 ml serum-free ESF921 medium (Expression Systems) with a multiplicity of infection (MOI) of 1. The cells were incubated at 27 ℃ for 96 h. *In cellulo* crystal formation was verified by light microscopy using a Nikon Ts2R-FL microscope employing differential interference contrast. For chip loading, the cells were resuspended in cell- culture medium in the well and transferred into a 1.5 ml tube. After centrifugation for 1 min at 200g, the cell pellet was resuspended in 200 ml ESF921 medium and the cell suspension was pipetted onto the chip. Excess medium was removed using a custom-made

vacuum system [227].

4.2.2 *In situ* protein crystallization

HARE-chip design

The HARE-chips used in these experiments have previously been described in detail [227]. Briefly, lithographic techniques were used to produce >20,000 tapered bottomless wells, also called features, in single-crystal silicon. These have 6 × 6 or 8 × 8 compartments containing 24 × 24 or 20 × 20 features, respectively, with top openings of 82 × 82 µm that taper to 10 × 10 µm or 15 × 15 µm (Figure 4.1a). Chips with larger bottom openings of 25 × 25 µm were used for the experiments with intracellular crystals and in order to visualize the crystals in a stereomicroscope.

In-chip crystallization

10 µl of the premixed solution containing equal amounts of protein and precipitant solution was deposited via pipette in even droplets across one row of compartments of the freshly glow-discharged chips. A thin, flexible metal blade was used to spread the liquid evenly over the surface and into the features of the chip (Figure 4.1b). The chip was quickly sealed with transparent tape inside the custom chip crystallization tray over 3 ml of precipitant solution. Growth was observed with an Olympus SZX10 microscope and images captured with an Olympus DP27 camera. Olympus Stream software was used for size measurements.

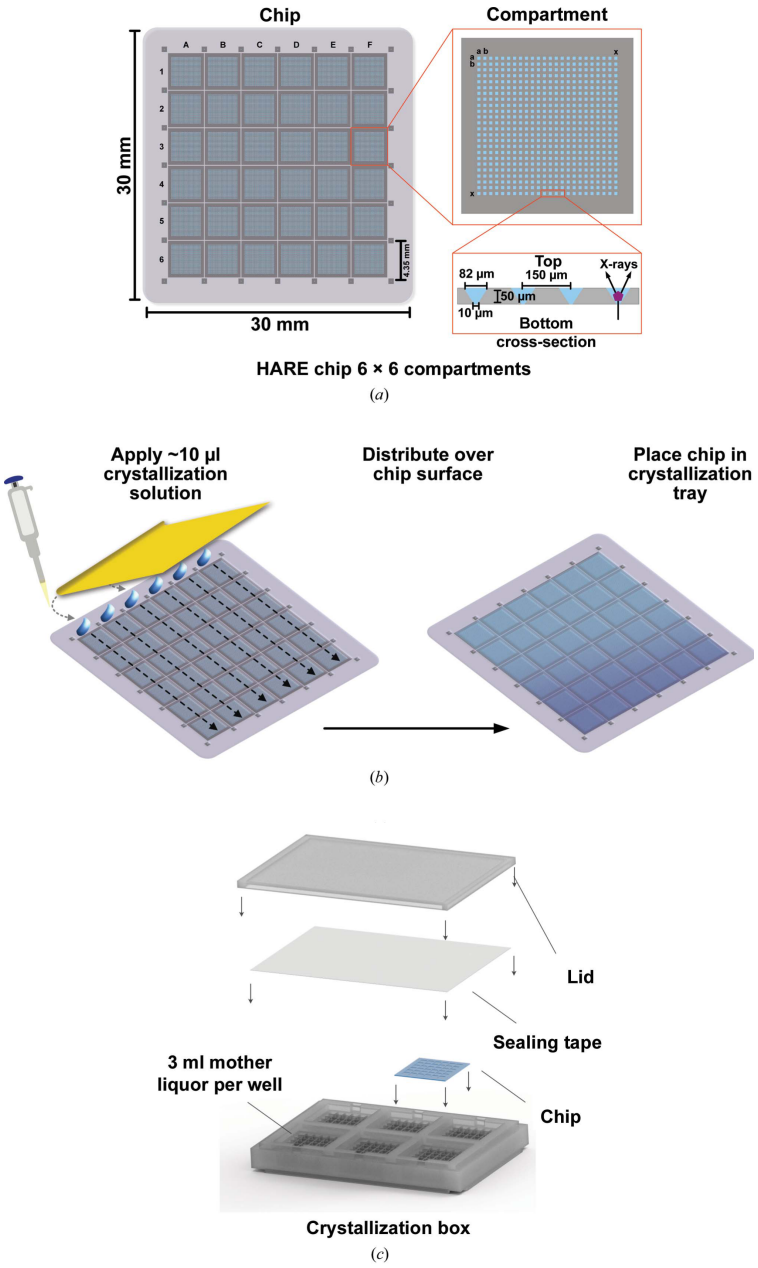

Figure 4.1: Vapor diffusion micro-crystallization procedure within the HARE-chip. a) Silicon HARE- chip with 6 × 6 compartments containing 24 × 24 features per compartment. The cross section shows the dimension of the features. b) A blade is used to spread a minimal amount of crystallization mixture evenly over the surface of the chip and into the features. c) 6 chips can be placed in the crystallization tray to conduct canonical vapor diffusion crystallization experiments. Sample consumption is minimized to 10 µl crystallization solution (using just 5 µl of protein stock solution) per chip.

Vapor diffusion micro-crystallization tray

To streamline vapor diffusion micro-crystallization with the HARE chips, we designed a custom in-chip crystallization box. Following a conventional vapor-diffusion approach, the crystallization solution can be loaded to the chip and placed on the crystallization box filled with mother liquor. Sealing of the box with conventional crystallization tape prevents dehydration of the mother liquor and allows for in-chip crystallization of the proteins. This box roughly matches the SBS plate format and several boxes can be stacked for convenient storage (Figure 4.1c).

In cellulo, in-chip crystallization

For in-chip crystallization of HEX-1 in living insect cells, the chips were coated with a 0.1 mg/ml aqueous solution of poly-D-lysine for 1 h and washed twice with PBS (pH 7.0). The chips were subsequently submerged in ESF921 medium and covered with 9 x 10^5 High Five cells per chip. After 20 min incubation at 27 °C for adhesion of the cells to the chips surface, cells were infected with an MOI of 1 and incubated at 27 °C until the beamtime at 96 h post-infection (h.p.i). The chips were imaged via the beamline camera using an IR light source. Since the HARE chips are transparent to IR light, the cells can be seen within the feature of the chip as well as on its surface.

Centrifugation for crystal centering into features

The chips were transferred to a new crystallization tray to avoid spillover of the reservoir solution during centrifugation. They were quickly resealed over ∼500 µl of water to maintain hydration. For sensitive crystals, it may be advisable to use mother liquor rather than water. A Concentrator Plus centrifugal evaporator unit (Eppendorf) with an A-2-VC plate rotor

was used in centrifuge mode at 1400 min^{-1} without vacuum and the plates were spun for 1 minute and returned to their original tray for storage until data collection.

4.2.3 Serial X-ray diffraction experiments

Serial data collection

All serial X-ray diffraction experiments were conducted at room temperature at EMBL beamline P14-2 (T-REXX) at the PETRA-III synchrotron at DESY, Hamburg (https://www.embl-hamburg.de/services/mx /P14_EH2/). The chips were mounted into chip holders inside a humidified chamber to prevent dehydration. They were sealed with 2.5 µm Mylar foil seals then connected to SmarAct translation stages as described previously [212, 224, 227]. These three-axis piezo translation stages precisely control the movement of the chips into the X-ray beam. Diffraction was recorded on an Eiger 4M detector. Data collection was done at room temperature at an energy of 12.65 and 12.7 keV, respectively with a single diffraction pattern recorded for each feature. Diffraction images were visualized via the Adxv software [236].

Structure determination

Diffraction data were processed using CrystFEL for peak finding, integration and hit-map generation [237]. Phasing was performed using Phaser molecular replacement [78]. PDB models 1DPX, 6J43, 6QNI, 6FD8, and 1KHI were used as search models for lysozyme, proteinase K, xylose isomerase, γS-crystallin variant, and HEX-1, respectively. Phenix was used for refinement and the structures were manually edited in Coot between rounds of refinement [79, 80]. Structure images were produced in PyMOL (Schrödinger).

4.3 Results

4.3.1 Proof of principle

In-chip protein crystallization procedure

In an initial proof-of principle experiment we aimed to demonstrate that proteins can be crystallized directly in the features of the HARE-chip using a canonical vapor diffusion approach (Figure 4.1). To this end crystallization conditions were first optimized for lysozyme via traditional hanging drop vapor diffusion screens, targeting high nucleation rates and crystals of approximately 20 µm in size in all dimensions (Figure 4.2a). Frequent nucleation was achieved by increasing the protein concentration of the crystallization solution. Further strategies for identifying promising conditions for serial crystallography and optimizing for nucleation rate and homogeneity are described by Beale *et al.* [233].

Using these optimized conditions, a solution of the same ratio of lysozyme:precipitant concentration was prepared to afford 10 µl of crystallization solution. This solution was applied to the top row of the silicon chip and spread across the surface and into the features of the chip with a thin flexible metal blade. Therefore, 5 µl of protein solution, assuming a 1:1 ratio of protein:precipitant, are sufficient to fill a complete chip (Figure 4.1b).

For lysozyme, the amount of protein consumed to fill a single chip was 350 µg. The total volume to fill the chip features can be further lowered to ∼7 µl, however with lower volumes a manual distribution to all corners of the chip becomes more difficult. Additionally, an application inside of a humidity-controlled environment is recommended to avoid rapid evaporation; a home-built solution was described previously by Mehrabi *et al.* [227]. The chips were then sealed using standard crystallization sealing tape inside custom-designed crystallization trays (Figure 4.1c). The trays are designed to hold 6 chips and 3 ml of reservoir solution per

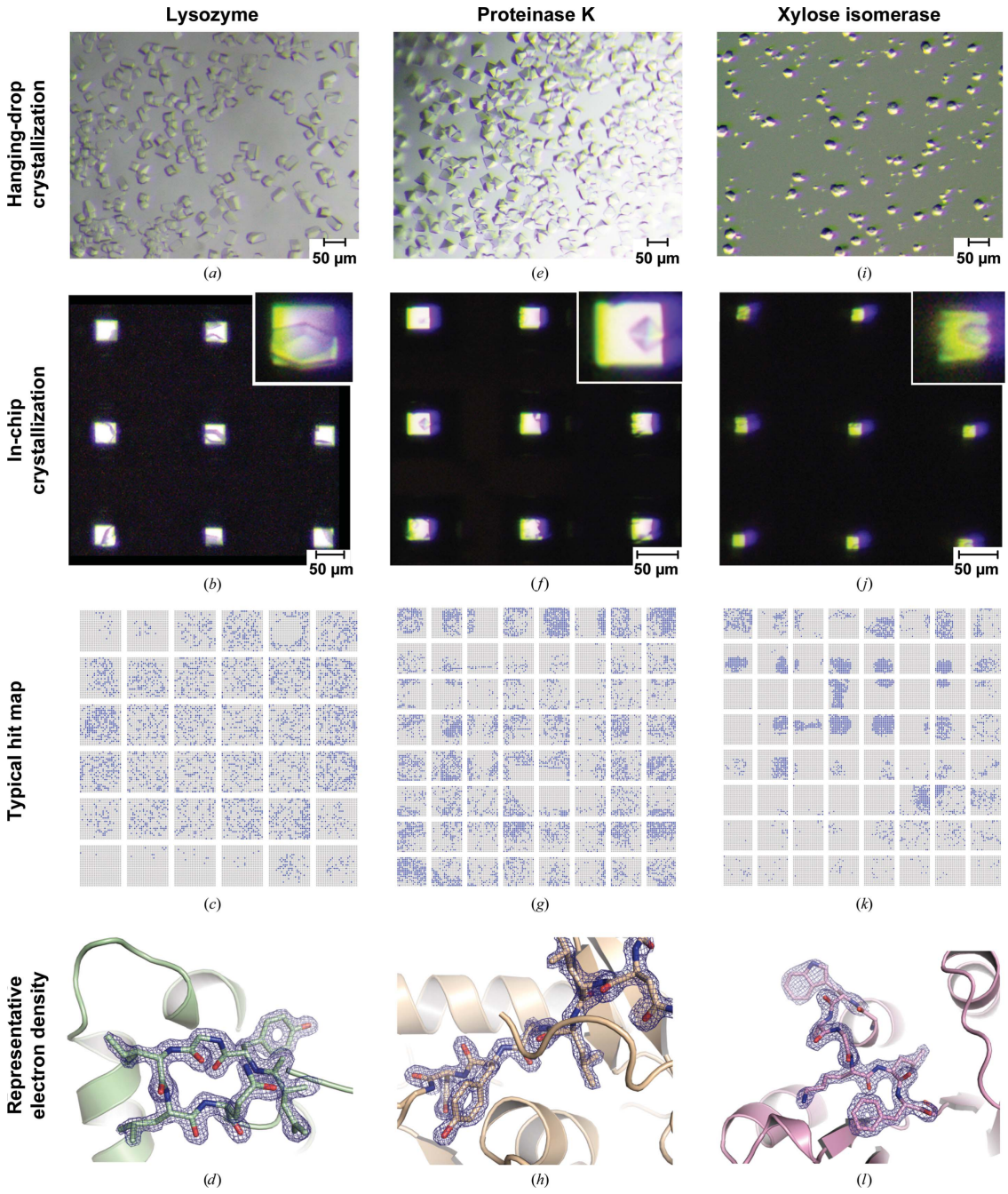

Figure 4.2: Vapor diffusion in-chip crystallization of model proteins. In-chip crystallization of model proteins (a)-(d) lysozyme, (e)-(h) proteinase K, and (i)-(l) xylose isomerase. Conventional hanging drops are compared to in-chip crystallization using the same crystallization conditions. The insert shows enlarged images of crystals within the features of the HARE-chip. A representative hit map is shown for each model protein, where blue indicates a recorded diffraction pattern that was successfully indexed by CrystFEL. A representative section of the $2F_o$-F_c (contoured at 2σ) electron density map after refinement of data from a single chip.

chip well, to enable either screening of multiple conditions or efficient in-chip crystallization of an established condition. The trays are translucent, allowing for the observation of the crystals in the features with a stereomicroscope. We anticipate that UV-microscopy would be ideally suited to visualize the crystals in the features of the chips and facilitate monitoring crystallization success; however, as the trays are not UV-transparent, the chips would need to be removed and sealed with transparent foil for evaluation by UV-microscopy In lack of an appropriate UV-microscope, visible light microscopy was used to analyze in-chip crystallizations prior to data collection. To better visualize the crystals within the features, the conditions for the crystallization solution were first tested on chips with features with 25 × 25 µm bottom openings as these allow more transmitted light (Figure 4.2b). For diffraction data collection, we used chips with bottom openings of 10-15 µm. The chips were mounted onto the high-speed translation stages for serial data collection at EMBL beamline P14-2 (T-REXX) at PETRA-III (Table 4.3, 4.2, and 4.3). The indexing rate describes the indexed diffraction patterns per number of collected images. Hit maps and histograms of resolution and unit cells parameters are shown in Appendix C.

Crystal centering increases hit rates

From visual analysis of the initial lysozyme trials (Chip 1, Chip 2) it was noted that almost all features contained one or more crystals. Initially however, the hit rates during diffraction data collection were significantly lower than the visual inspection would suggest. Presumably, crystals located in the periphery of the features likely fell outside the beam path, as the beam (13 x 7 µm) is centered at the openings (10 x 10 µm) of the features. To address this problem, we sought for a crystal-centering method. To this end, a post-crystallization centrifugation step was included in the workflow to gently sediment the crystals to the bottom center of the features. The centering of crystals in the features is apparent in the images of the same features of a chip with in-chip grown lysozyme crystals shown before and after centrifugation.

Table 4.1: X-ray data collection and refinement statistics for in-chip crystallized lysozyme.

	Lysozyme			
	Chip 1	Chip 2	Chip 3	Chip 4
PDB code	-	-	7NKF	7NJF
Crystal centering	-	-	-	yes
Normalized protein used (μg)	138.9	263.3	325.0	325.0
Collected features	10944	20736	25600	25600
Indexed features	2938	3707	7498	14840
Indexed diffraction patterns	2991	3973	8611	20911
Indexing rate	27%	19%	34%	82%
Indexed patterns per µg protein	22	15	26	64
Space group	P 4_32_12	P 4_32_12	P 4_32_12	P 4_32_12
a, b, c (Å)	78.6, 78.6, 38.6	78.5, 78.5, 38.6	78.8, 78.8, 38.7	78.5, 78.5, 38.8
α, β, γ, (°)	90, 90, 90	90, 90, 90	90, 90, 90	90, 90, 90
Resolution (Å)	78.74–1.70 (1.76–1.70)	78.74–1.70 (1.76–1.70)	55.87–1.70 (1.76–1.70)	55.56–1.70 (1.76–1.70)
CC* (%)	98.3 (93.3)	98.6 (90.9)	98.8 (97.2)	99.6 (98.2)
R_{split} (%)	19.69 (46.63)	17.67 (55.87)	16.55 (22.52)	10.00 (21.50)
$<I/\sigma(I)>$	5.1 (2.1)	5.2 (1.8)	6.8 (4.7)	10.1 (4.5)
Mutliplicity	68	81	174	408
Completeness (%)	100.00 (100.00)	100.00 (100.00)	100.00 (100.00)	100.00 (100.00)
Resolution range			55.72–1.70	55.51–1.70
for refinement (Å)			(1.83–1.70)	(1.76–1.70)
No. of reflections			13920 (1358)	13833 (1356)
R_{work} (%)			0.1750 (0.1964)	0.1740 (0.2130)
R_{free} (%)			0.2118 (0.2233)	0.2028 (0.2794)
Mean B-factor ($Å^2$)			22.49	24.6
No. non-H Atoms				
protein			1023	1013
ligand/ions			1	1
water			74	69
R.m.s. deviations				
bond length (Å)			0.013	0.006
bond angles (°)			1.26	0.93
Ramachandran				
favored (%)			99.21	98.41
allowed (%)			0.79	1.59
outliers (%)			0.00	0.00

Table 4.2: X-ray data collection and refinement statistics for in-chip crystallized proteinase K.

	Proteinase K				
	Chip 1	Chip 2	Chip 3	Chip 4	Chip 5
PDB code	-	-	7NJJ	-	-
Crystal centering	-	-	-	-	-
Normalized protein used (μg)	243.0	243.0	240.7	300.0	202.5
Collected features	20736	20736	20543	25600	17280
Indexed features	4574	2221	7618	2751	3661
Indexed diffraction patterns	5294	2502	10489	3855	4360
Indexing rate	26%	12%	51%	15%	25%
Indexed patterns per µg protein	22	10	44	13	22
Space group	P 4_32_12	P 4_32_12	P 4_32_12	P 4_32_12	P 4_32_12
a, b, c (Å)	68.3, 68.3, 108.2	68.5, 68.5, 108.6	68.5, 68.5, 108.7	68.4, 68.4, 108.4	68.4, 68.4, 108.2
α, β, γ, (°)	90, 90, 90	90, 90, 90	90, 90, 90	90, 90, 90	90, 90, 90
Resolution (Å)	108.70–1.65 (1.71–1.65)	108.70–1.65 (1.71–1.65)	68.49–1.65 (1.71–1.65)	68.49–1.65 (1.71–1.65)	68.49–1.65 (1.71–1.65)
CC* (%)	94.9 (88.1)	85.8 (74.2)	97.3 (76.3)	92.5 (79.1)	95.4 (78.3)
R_{split} (%)	33.23 (48.24)	57.24 (81.11)	26.03 (67.77)	41.50 (66.25)	32.91 (62.75)
$<I/\sigma(I)>$	3.7 (2.4)	2.4 (1.5)	3.9 (1.7)	2.9 (1.8)	3.6 (1.9)
Mutliplicity	37	17	72	45	45
Completeness (%)	99.98 (99.97)	99.8 (99.20)	100.00 (100.00)	100.00 (99.97)	99.9 (99.97)
Resolution range for refinement (Å)			57.95–1.65 (1.71 –1.65)		
No. of reflections			31851 (3100)		
R_{work} (%)			0.1779 (0.2534)		
R_{free} (%)			0.2033 (0.2875)		
Mean B-factor (Å^2)			15.29		
No. non-H Atoms					
protein			2031		
ligand/ions			4		
water			209		
R.m.s. deviations					
bond length (Å)			0.006		
bond angles (°)			0.77		
Ramachandran					
favored (%)			97.11		
allowed (%)			2.89		
outliers (%)			0.00		

Table 4.3: X-ray data collection and refinement statistics for in-chip crystallized proteins.

	Xylose isomerase	γS-crystallin mutant	HEX-1	
			Loaded	*In situ*
PDB code	7NJG	7NJE	7NJI	7NJH
Crystal centering	yes	yes	-	-
Normalized protein used (μg)	400.0	55.0	-	-
Collected features	25600	25600	20736	25281
Indexed features	3040	1482	5100	2023
Indexed diffraction patterns	5186	1510	5520	2111
Indexing rate	20%	6%	27%	8%
Indexed patterns per µg protein	13	27		
Space group	I222	$P2_12_12_1$	$P6_522$	$P6_522$
a, b, c (Å)	94.5, 103.2, 99.8	38.4, 89.2, 111.3	58.9, 58.9, 193.0	58.6, 58.6, 192.7
α, β, γ, (°)	90, 90, 90	90, 90, 90	90, 90, 120	90, 90, 120
Resolution (Å)	71.04–1.70 (1.97–1.90)	69.60–3.00 (3.05–3.00)	86.94 – 2.30 (2.38–2.30)	64.10–2.50 (2.59–2.50)
CC* (%)	93.9 (76.6)	98.9 (88.5)	97.6 (74.3)	95.9 (74.8)
R_{split} (%)	41.28 (96.66)	28.96 (110.43)	25.00 (100.71)	28.39 (120.53)
$<I/\sigma(I)>$	2.3 (1.1)	2.5 (1.0)	3.2 (1.2)	3.1 (0.9)
Mutliplicity	111	48	93	37
Completeness (%)	100.00 (100.00)	99.96 (100.00)	100.00 (100.00)	99.87 (99.86)
Resolution range for refinement (Å)	51.57 –1.90 (1.97 –1.90)	69.60–3.00 (3.11-3.00)	51.01 –2.3 (2.38 –2.30)	50.71–2.50 (2.59 –2.50)
No. of reflections	38717 (3834)	8132 (787)	9522 (917)	7394 (706)
R_{work} (%)	0.2016 (0.2789)	0.2350 (0.3796)	0.2193 (0.3138)	0.2202 (0.3415)
R_{free} (%)	0.2440 (0.3225)	0.2711 (0.4785)	0.2601 (0.3753)	0.2553 (0.3660)
Mean B-factor ($Å^2$)	22.74	52.64	47.52	55.55
No. non-H Atoms				
protein	3076	2903	1128	1128
ligand/ions	1	0	0	0
water	265	16	28	13
R.m.s. deviations				
bond length (Å)	0.003	0.004	0.010	0.007
bond angles (°)	0.6	0.84	1.16	0.89
Ramachandran				
favored (%)	96.62	95.93	95.17	95.17
allowed (%)	3.12	3.49	3.45	2.76
outliers (%)	0.26	0.58	1.38	2.07

In Figure 4.3a, only edges of the lysozyme crystals are apparent as they are located on the periphery of the features. After centrifugation, in Figure 4.3b, multiple crystals can be seen in each well and are now likely to be within the beam path.. To minimize crystallization variance, two identical lysozyme chips (Chip 3, Chip 4) were then prepared from the same stock solution of protein:precipitant mixture. Chip 3 was used as before, while Chip 4 was centrifuged for 1 minute at 1400 rpm (∼120 g). Centrifugation yields up to a nearly a 2-fold increase in the indexing rate and does not appear to have detrimental effects on diffraction quality (Table 4.1, Figure 4.3c and 4.3d). Lysozyme structures were solved at a resolution of 1.70 Å (Figure 4.2d) for Chip 3 (not centrifuged) and Chip 4 (centrifuged) datasets of in-chip grown crystals (Table 4.1) and the refined structures have been deposited in the Protein Data Bank (PDB ID: 7NKF and PDB ID: 7NJF, respectively).

Additional model systems can be crystallized inside HARE-chips

In-chip crystallization was then tested on two additional systems with well-known crystallization protocols, proteinase K and xylose isomerase. Similar to the strategy for lysozyme, conditions for abundant nucleation and ∼20 µm crystal size were optimized in hanging drop crystallization setups (Figure 4.2e and 4.2i). These optimized conditions were then directly applied to the chip in 10 µl (5 µl of protein mixed with 5 µl of mother liquor) droplets, and spread into the chip features, yielding in-chip grown crystals (Figure 4.2f and 4.2j). The total amount of protein sample consumed for each chip for proteinase K and xylose isomerase was 300 µg and 400 µg, respectively. Data from six proteinase K chips and one xylose isomerase chip were collected. Using datasets from proteinase K chip 3 and xylose isomerase chip 1, the structures for each were solved at a resolution of 1.65 Å and 2.00 Å, respectively (Table 4.1 and 4.3, Figure 4.2h and 4.2l). Coordinates have been deposited in the PDB (PDB: 7NJJ, 7NJG).

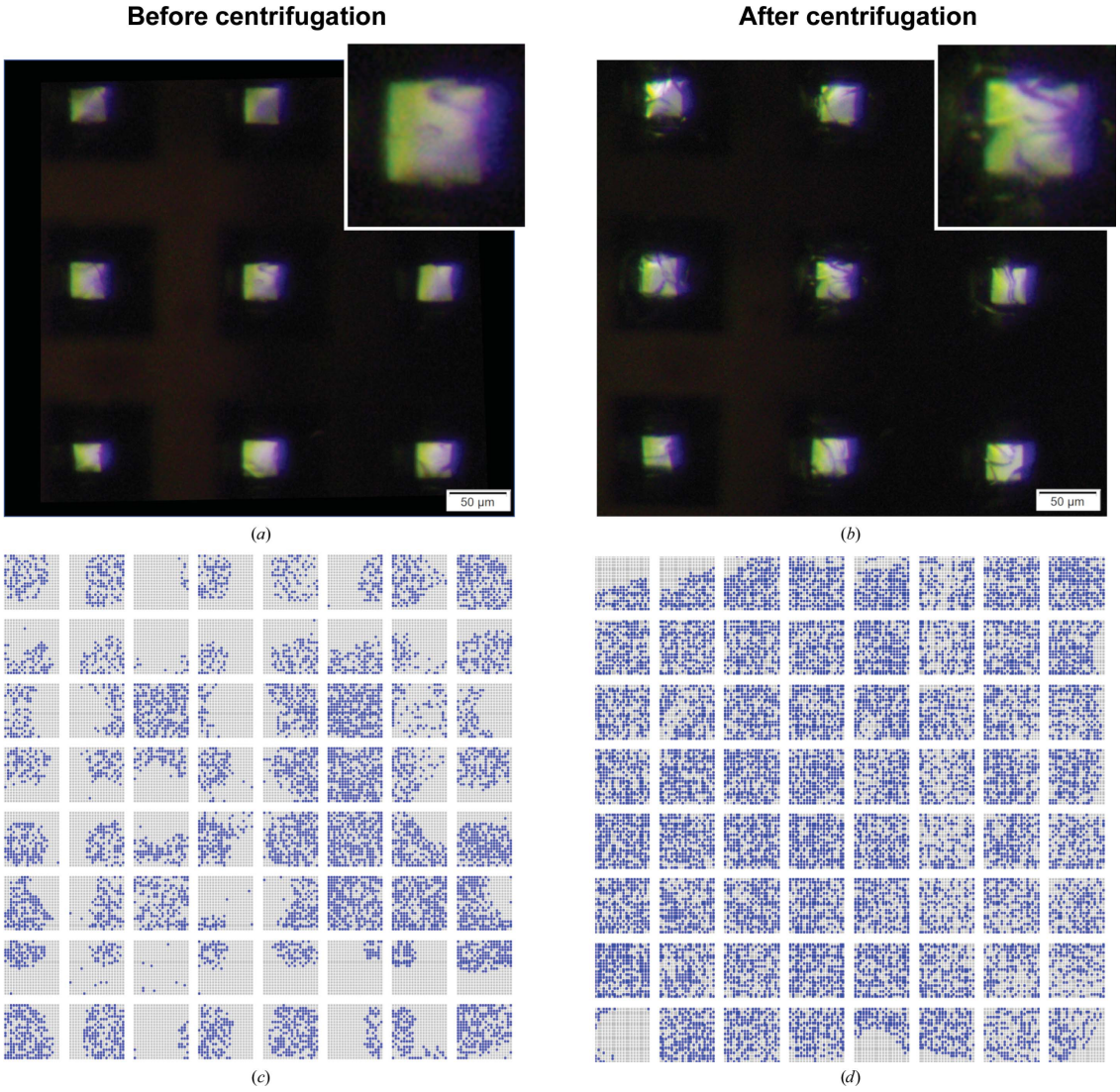

Figure 4.3: Crystal centering using gentle centrifugation. The same features of a chip with lysozyme crystals are shown (a) before and (b) after centrifugation for 1 min. Hit maps for two identical chips prepared from the same stock solution of lysozyme:precipitant mixture (c) without centrifugation and (d) with centrifugation. Blue indicates a recorded diffraction pattern that was successfully indexed by CrystFEL.

4.3.2 In-chip crystallization of a new protein variant

Although the crystallization of model systems is an important quality control, we wanted to demonstrate that this method can also be used for novel structure determination of a previously unsolvedprotein. Moreover, we also sought to demonstrate that micro-crystallization can be achieved at protein concentrations typical for soluble proteins (5 - 25 mg/ml).

In-chip crystallization of human γS-crystallin

To this end, we investigated an aggregation-prone, deamidation variant of the highly soluble eye lens protein, human γS-crystallin. The deamidation variant of γS-crystallin used in this study is an extreme example of naturally occurring, age-related deamidation and is implicated in cataract formation [46, 57]. In total this variant has nine substitutions of amide-containing amino acids to carboxylic acid-containing amino acids. To date, only two crystal structures have been reported for human γS-crystallin, presumably because these highly soluble crystallins resist crystallization in keeping with their biological role [64, 83].

Via conventional sparse matrix screens, we identified a crystallization condition for this novel variant and then optimized it for higher nucleation rates. We found suitable vapor diffusion hanging-drop crystallization to be achievable at a protein concentration of 11 mg/ml (Figure 4.4a). The same crystallization condition was then applied to the chip using the previously established protocol. In-chip crystal growth was observed in our custom crystallization trays after 1 day of incubation at 25 °C (Figure 4.4b). Notably, the total amount of protein consumed to fill a chip was only 55 µg, demonstrating that this method is suitable to directly transfer vapor diffusion, hanging-drop crystallization conditions to the chip format without high sample consumption. This experiment also shows how standard high-throughput screening workflows can be utilized to enable serial crystallography with the HARE-chip technology. The structure was solved at a resolution of 3.0 Å from a single chip (Table 4.3, Figure 4.4c and 4.4d). The refined structure has been deposited in the PDB (PDB: 7NJE).

Structure of a novel γS-crystallin variant

While Purkiss and coworkers determined the crystal structure of the human γS-crystallin truncated to just the C-terminal domain (PDB: 1HA4)[83], Thorn *et al.* crystallized the dimer of γS-crystallin linked via an intermolecular disulfide bond between the C24 in each

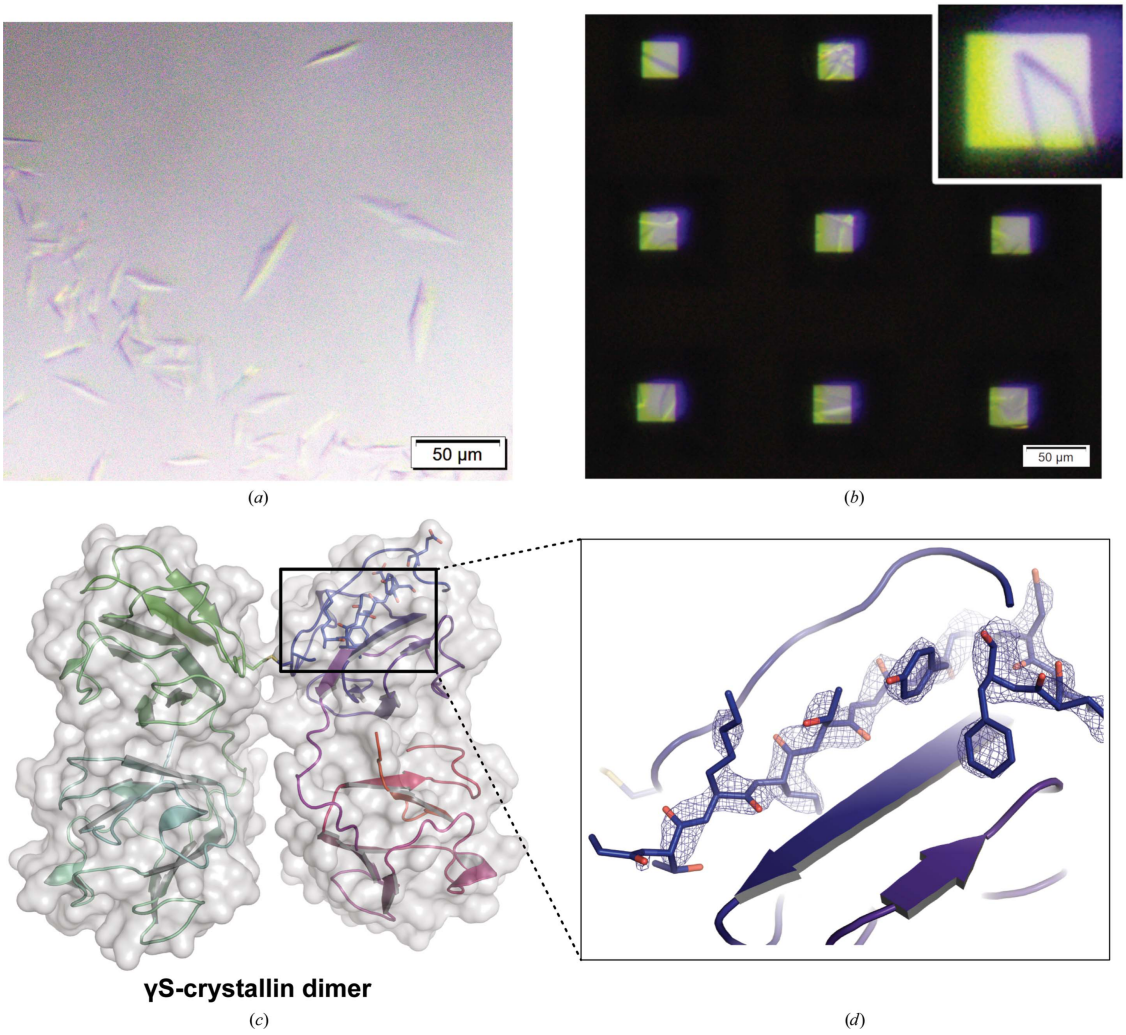

Figure 4.4: In-chip crystallization of γS-crystallin. Crystallization of the γS-crystallin variant using the same crystallization condition in traditional hanging drops (a) and for in-chip crystallization (b). The insert shows an enlarged image of a crystal within the chip features. (c) The solved structure for the γS-crystallin variant with two monomers linked via a disulfide bond. (d) Representative section of the $2F_o$-F_c (contoured at 2σ) electron density map after refinement from the merged datasets of the two chips for the γS-crystallin variant. From N-terminus to C-terminus chain A is colored from blue to red, while chain B is colored from green to cyan.

monomer (PDB: 6FD8) [64]. Solution-state NMR has also been employed in the study of human γS-crystallin; structures of the wild type monomer (PDB: 2M3T) [68, 82] and aggregation prone single-site variants (PDB: 2M3U, 6IF9) [82, 238] have been solved. The γS-crystallin deamidation variant structure reported here crystallizes in space group $P2_12_12_1$. It shows a disulfide-linked dimer at the same pair of cysteines (numbered here as Cys25) as the

wild-type dimer structure PDB:6FD8. However, unlike 6FD8, this novel structure arranges in a different orientation from the previously described QR configuration [64]. Instead, the monomers are mirrored across the dimer interface (Figure 4.4c), with interfacial contacts arising from the disulfide bonds between Cys25 on each subunit and the δ-oxygen of Arg26 and τ-nitrogen of His87 on either subunit. The fold of the monomer units is highly similar to 6FD8, with a global RMSD of 0.463 Å derived from the alignment of a chain A from 6FD8 and chain A from the variant γS-crystallin dimer structure solved here [64]. The mutated sites appear to play a significant role in the crystallization of this deamidated variant. Additional crystal packing contacts are visible in this novel structure that are absent from other reported structures. Significantly, five out of the nine sites of deamidation (Asp15, Glu121, Asp144, Glu17, and Glu107) create salt bridges to symmetry mates; these contacts are absent in the 6FD8 and 1HA4 structures.

Deamidation and oxidation are frequently observed modifications in crystallins in cataractous lenses [10, 33, 44, 46]. Deamidation has even been suggested to lead to increased disulfide bond formation [49, 54]. Human γS-crystallin, with its higher cysteine content compared to other lens crystallins, displays extensive deamidation and disulfide bonding in aged lenses [55, 239, 240], and fulfills a complex role in the lens with the potential to mediate oxidative damage via disulfide exchange [35]. Although both deamidation and oxidation are suggested to result in minor structural changes, these small structural changes can still be critically detrimental to protein dynamics and stability [49, 54, 64]. Further work is being conducted to define the role of deamidation in γS-crystallin stability and aggregation propensity and to investigate the interplay of multiple post-translational modifications in cataract formation.

4.3.3 Intracellular protein crystallization

Exploiting the intrinsic ability of cells to crystallize proteins represents an alternative approach to obtain protein micro-crystals suitable for X-ray crystallography [226]. We have previously shown that serial femtosecond diffraction of µm-sized protein crystals directly in living cells on a fixed target (FT-SFX) enables high-resolution structure elucidation [241]. The structure of HEX-1 from the fungus *Neurospora crassa*, crystallized in Sf9 insect cells, was solved at 1.8 Å resolution using diffraction data from only a single chip collected within 12 min at the Linac Coherent Light Source (LCLS). Here, we used the same protein to test the applicability of fixed-target sample delivery for serial *in cellulo* diffraction data collection at a synchrotron source at room temperature.

HEX-1 is the woronin body major protein in the filamentous fungus *N. crassa* and naturally forms crystals to seal the septal pores in case of cell damage [242]. The spontaneous self-assembly into intracellular crystals also occurs in insect cells after infection by a recombinant baculovirus (rBV) encoding the HEX-1 gene. Regular, micrometer-sized hexagonal crystals grow reproducibly and with high efficiency in living insect cells [225]. In the High Five insect cells used here, crystal growth is observed 48 h after rBV infection at the earliest, with a maximum of crystal-containing cells at 96 h after infection. The cells produce spindle-like crystals with average dimensions of 26.3 ± 10.2 µm in length and 5.3 ± 1.5 µm in width, which is considerably larger than the crystal dimensions observed in Sf9 cells that we have used before (9.1 ± 3.2 µm in length and 3.5 ± 0.7 µm in width) [241], but only marginally larger than the feature openings of the chips that were used for the intracellular crystals (∼25 µm).

Establishing HARE-chips for *in cellulo* synchrotron diffraction data collection

In a first approach, serial diffraction of the intracellular HEX-1 crystals was established using the HARE-chips at the P14.2 synchrotron beamline. For that, High Five insect cells were infected with the HEX-1 encoding rBV in a 6-well cell culture plate using an MOI of 1. Intracellular crystal growth was confirmed by light microscopy four days after infection. Immediately before the diffraction experiment, crystal-containing cells were stripped and 200 µl cell suspension from a single well was loaded onto the chip using the previously described custom-made vacuum system [227]. Serial diffraction data was collected directly without any additional steps. The diffraction details for HEX-1 intracellular crystals are listed in Table 4.3. Applying the parameters of a primitive hexagonal unit cell, 5,520 of the recorded detector images were successfully indexed (27% indexing rate). The refined unit cell parameters are comparable to that extracted from previous X-ray diffraction experiments [225, 241, 243], confirming the indicated similar composition of the *in-vitro* and *in cellulo* grown HEX-1 crystals. The structural model of HEX-1 refined at 2.30 Å is superimposable to that obtained from FT-SFX of *in cellulo* grown HEX-1 [241], with an overall root mean square deviation (RMSD) of 0.225 for 141 Cα atoms.

Structure determination using *in situ* crystallized HEX-1

In a second approach, *in situ* crystallization of HEX-1 was tested in living High Five cells that have been loaded into the features of the HARE-chips. After adhesion on the poly-D-lysine coated silicon chip, High Five cells were infected with the HEX-1 encoding rBV and cultured on the chip surface until the diffraction experiment, 96 h p.i. An almost complete coverage of the chip surface by the cell layer was detected by light microscopy, clearly extending into the features (Figure 4.5a). Spindle-shaped crystals were observed in the majority of cells, exhibiting a morphology and dimensions comparable to that of intracellular HEX-1 crystals

grown in a cell culture plate. For serial diffraction data collection, the chip was removed from the well of the cell culture plate and excess of culture medium was removed before mounting. The diffraction details for HEX-1 *in situ* crystals are comparable to that obtained after loading HEX-1 crystal-containing cells onto the chip (Table 4.3). Although the indexing rate was slightly decreased (8%), diffraction data of a single chip enabled the structure determination at a resolution of 2.50 Å (Figure 4.5b). The refined HEX-1 structures solved by *in cellulo* diffraction of loaded crystal-containing cells and of *in situ* grown crystals have been deposited in the Protein Data Bank (PDB:7NJI and PDB:7NJH, respectively).

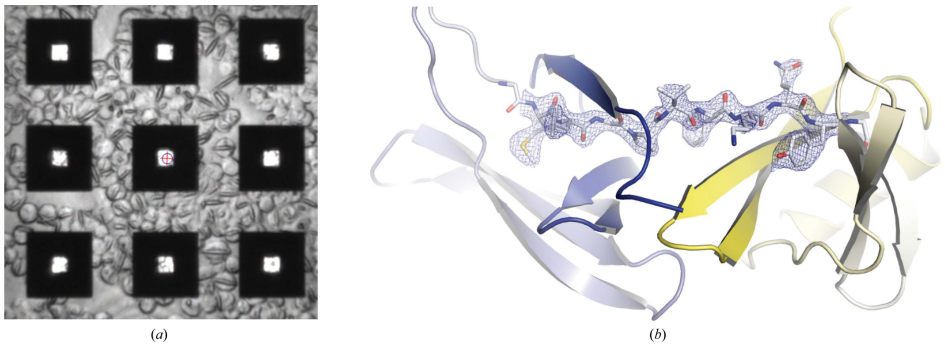

Figure 4.5: *In situ* crystallization of intracellular HEX-1 crystals. (a) Fungal protein HEX-1 crystallized *in cellulo* on the surface and in the features of the chip. (b) The HEX-1 structure with the N-terminal domain shown in blue and the C-terminal domain shown in yellow with a representative section of the $2F_o$-F_c (contoured at 2σ) electron density map after refinement from the chip 1 dataset.

4.4 Discussion

As in any crystallographic project, the availability of homogenous, well-diffracting microcrystals is an experimental bottleneck in fixed-target serial-crystallography. Therefore, previous studies have focused on reducing sample consumption and crystal handling of batch-crystallized solutions. Lyubimov *et al.* loaded microfluidic trap arrays with only 5 µl of crystal slurry [244], while Murray *et al.* transferred even smaller volumes (<2 µl) of micro-

crystal suspensions onto X ray-transparent silicon nitride chips [245]. Recently, Davy *et al.* used acoustic droplet ejection to load the 'Oxford photo-chips' (highly similar to the HARE-chips) with only 3 µl of crystal slurry grown in batch [221]. Although these methods provide a remarkable sample reduction, they all rely on pre-crystallized material. By contrast, the crystallization on the surface of fixed targets supports has also been described before.

While Ren *et al.* used monocrystalline quartz plates as a support structure for on chip crystallization of various sizes [246], Lee *et al.* developed a one-dimensional fixed target system in which microcrystals are loaded into an array of polyimide tubes [247]. This method allows for low sample consumption and was shown to successfully grow crystals *in situ* via batch crystallization. However, unlike the HARE-chips these techniques would not allow for ligand mixing studies that have become important for reaction initiation in time-resolved experiments and the method by Lee *et al.* does not support vapor diffusion-driven *in situ* crystallization [247]. By contrast, Lieske *et al.* developed an on-chip vapor diffusion crystallization method on the surface of the porous silicon 'Roadrunner' chips that were also used for ligand soaking [235]. In the methods mentioned above the crystals are randomly positioned rather than in predetermined locations, preventing the use of the HARE method for time-resolved crystallography [212]. Opara *et al.* developed an *in situ* crystallization method using silicon nitride membranes that is highly similar to the approach described here, as the crystals are located in predefined positions and crystallized using a vapor diffusion approach [248]. In contrast to the HARE-chips the silicon nitride membranes are closed on one side of the chip, which may lead to different crystallization results. In general, an exact comparison of the different approaches described above is complicated by different form-factors, the number of features as well as the concentration of the crystal slurries or proteins solutions.

As a practical advantage, crystallization within the HARE-chips requires minimal equipment and can thus be carried out in non-specialized labs. With the exception of the HARE-chips,

the required materials are common laboratory supplies or can be substituted with similar tools. The crystallization trays are readily accessible through 3D printing and the files are available with this manuscript. At the same time, this in-chip crystallization approach can be used to seamlessly extend existing high-throughput crystallization workflows. The major benefit of this approach is to directly transfer optimized crystallization conditions from droplets to the chip format, without or with limited additional adaptation. Notably, optimization does not require the use of an entire chip, but partial chip screening can be used to optimize the size and density of crystals using < 1 µl of protein solution in a single column of the HARE-chip compartments. Importantly, as the crystals are confined to grow inside the chip features and only a limited supply of protein is available within each feature, a crystal size limit compatible with time-resolved applications is inherent in the crystallization setup. The feasibility of this workflow is not only demonstrated by model systems, but also by the successful structure determination of a novel γS-crystallin variant, a group of proteins known to be rather recalcitrant towards crystallization. Thus, for novel systems, promising conditions for in-chip crystallization can be found using established, conventional screening approaches, which can later be extended to in-chip crystallization.

The reported model protein structures were solved using data from a single chip loaded with approximately 140-400 µg of protein for lysozyme, proteinase K, and xylose isomerase, slightly less than consumed by loading crystal slurries via vacuum loading of these proteins [213]. The median hit rate of 25% indicates that a single chip is usually sufficient for structure determination [249]. An interesting observation is that this can be substantially increased by a simple short centrifugation step, an aspect that needs further detailed exploration in future experiments. However, in-chip crystallization is not limited to model systems. The γS-crystallin structure demonstrates that in-chip crystallization can also be applied to non-model proteins. This structure also emphasizes that typical protein concentrations (here 11 mg/ml), commonly found in vapor diffusion crystallization screens are amenable to HARE-chip crystallization. At this protein concentration the overall sample consumption

reduces to 55 µg of protein per chip. This is a reduction of 5-10 fold compared to the amount of protein typically used in vacuum loading of crystal-slurries using the HARE-chip. However, in comparison to the model systems, γS-crystallin showed rather low hit rates (6%), and it is likely that its comparably low protein concentration affected the final crystal density. Presumably, a further optimization of the nucleation propensity, or the use of seed-stocks, would have a positive effect on the crystallization and lead to higher in-chip hit rates [233]. While the hit rate determines the efficiency of the data-collection experiment, serial crystallography also permits to estimate the efficiency of the crystallization itself. To this end the number of diffraction patterns can be compared to the total amount of protein. While the model-systems showed a median number of 21 diffraction patterns per µg of protein, γS-crystallin showed 27 diffraction patterns per µg of protein – thus a comparable efficiency of the crystallization. This emphasizes the potential of HARE-chip crystallization to reduce the amount of protein that is required for serial crystallography. We note that, an automation of these workflows in the future will likely lead to a further reduction of the sample requirements.

In addition to reduced sample consumption, another advantage of in-chip crystallization is the reduced crystal handling compared to the vacuum loading method previously used in HARE time-resolved studies. With in-chip crystallization, the crystals can remain unperturbed after growth, with no transfer steps between growth and data collection. This could be of particularly aid to intracellular crystallization as these samples are often highly sensitive, especially when the crystals are purified from the cells. However, intracellular protein crystallization offers some distinct advantages over traditional screening approaches: crystals can be grown in a cellular environment with natural post-translational modifications [206] alongside a diverse array of small molecules and possible cofactors to support crystallization; indeed, cofactors have been discovered via this method [207]. *In cellulo* crystallization is also more scalable and eschews laborious purification steps. We have recently shown that silicon chips are ideally suited for serial crystallography providing high-resolution diffrac-

tion of HEX-1 crystals within the intact cells, via serial femtosecond crystallography (SFX) at an XFEL [241]. Here, we confirm that fixed-target delivery of crystal-containing cells also enables fast and efficient data collection via serial synchrotron crystallography (SSX) at room temperature. It is possible that the resolution of the diffraction data is limited by the reduced photon flux of the synchrotron source. However, the HEX-1 structure determined via SSX is directly superimposable to that determined via fixed-target SFX, validating the comparability of SSX and SFX data [249].

Moreover, insect cells can be cultivated and infected directly on the surface of the HARE-chips without affecting the growth and the quality of the HEX-1 crystals. The *in situ* approach provides the advantage to avoid any cell transfer procedures, thus the sample remains unperturbed until X-ray exposure. In contrast, loading of cells containing preformed crystals requires the removal of excess medium. If harsh vacuum loading systems are used, this could affect the cell integrity and thus the crystal quality, since virus infected cells are particularly sensitive to mechanical stress. The viral infection might also inhibit the attachment of the crystal-containing cells to the chip surface after loading, leading to the loss of some cells during removal of the cell culture medium and thus to reduced hit rates. These limitations should be overcome by the *in situ* approach, but the indexing rate did not improve. This is attributed to problems in growing the cell monolayer up to the center of the chip features, where any support is missing. Thus, several features did not contain a crystal-containing cell in the volume that is hit by the X-ray beam. It needs to be tested in future studies if a very gentle centrifugation centering will improve the hit rates, as observed for other samples.

In addition to the advantage of exploiting intracellular crystals via SSX, this work demonstrates that the main advantage of HARE-chip delivery of intracellular crystals, is a significant reduction of the required material. Per indexed diffraction pattern this method has an almost 2000-fold lower sample consumption compared to liquid-jet SFX approaches,

previously performed to solve the structures of *T. brucei* CatB and IMPDH [206, 207].

4.5 Conclusions

Here we present a new crystallization technique inside HARE-chips that can substantially reduce protein consumption and sample handling for serial X-ray crystallography. Canonical vapor diffusion crystallization conditions can be directly transferred to crystallize inside the HARE-chips. The direct growth of protein micro-crystals within precisely defined features is therefore compatible with the HARE-method for efficient time-resolved crystallography. For systems that are costly to produce, resist batch crystallization, form highly delicate crystals, or crystallize in living cells, in-chip crystallization may offer distinct advantages over other sample preparation techniques.

4.6 Author contributions

E.C.S. initiated and devised the research; A.O.K purified gamma crystallin; B.N.B. carried out in-chip crystallization experiments; H.S. and E.C.S. designed the in-chip crystallization tray; P.M., E.C.S, J.B. and D.v.S. carried out data-collection and processing; R.S., J.B. and L.R. carried out all *in-cellulo* experiments. B.N.B., L.R. and E.C.S wrote the manuscript. All authors discussed and corrected the manuscript.

Chapter 5

Conclusion

The long-lived proteins of the human eye lens, the crystallins, have evolved to be remarkably resilient proteins. Their fine-tuned surface properties create the necessary balance to produce lens transparency and resist protein aggregation. Even with extensive deamidation and oxidation modifications, as detailed in this thesis, γS-crystallin maintains its overall protein fold; however, these modifications alter the protein's stability and propensity for aggregation. Higher dynamics likely exposes hydrophobic portions of the protein and these partially unfolded states aggregate, eventually leading to light-scattering protein precipitates characteristic of cataract. γS-crystallin in particular may be predisposed to accumulate oxidative modifications in the form of disulfide bonds between its highly solvent-exposed cysteines. This observation hints at a more complex role for γS in the lens, not only as a structural protein that contributes lens refractive index, but as a participant in lens redox homeostasis. Further investigation into the role of γS and other eye lens proteins as chemical participants, resisting as well as employing post-translational modifications, is warranted. Future work may also look to explore further the prevalence in aged and cataract lenses of multiple post-translational modifications occurring on a single protein molecule and the possible synergistic effects.

The surface properties that help crystallins maintain short-range ordered spatial arrangements in the lens as well as resist protein aggregation likely also contribute to their recalcitrance to protein crystallization. The in-chip method of crystallization described in this thesis expands the toolkit available for serial crystallography on hard-to-crystallize proteins, such as the crystallins, that may form small and delicate crystals. This technique maximizes sample economy and minimizes physical stress. Further work may improve on this method, possibly using seed stocks to increase nucleation for higher hit rates. With this alternative route to crystallization harnessing direct growth in serial crystallography chips, a number of previously unfeasible protein systems may be studied with time-resolved crystallography, providing reaction mechanisms and structures of short-lived reaction intermediates.

Bibliography

[1] R Michael and AJ Bron. The ageing lens and cataract: a model of normal and pathological ageing. *Philos. Trans. R. Soc. Lond., B, Biol. Sci.*, 366(1568):1278–1292, 2011.

[2] Peter J Francis, Vanita Berry, Anthony T Moore, and Shomi Bhattacharya. Lens biology: development and human cataractogenesis. *Trends Genet.*, 15(5):191–196, 1999.

[3] K Krishna Sharma and Puttur Santhoshkumar. Lens aging: effects of crystallins. *Biochim. Biophys. Acta - Gen. Subj.*, 1790(10):1095–1108, 2009.

[4] Venkata Pulla Rao Vendra, Ismail Khan, Sushil Chandani, Anbukkarasi Muniyandi, and Dorairajan Balasubramanian. Gamma crystallins of the human eye lens. *Biochim. Biophys. Acta - Gen. Subj.*, 1860(1):333–343, 2016.

[5] Lisa Brennan, Joshua Disatham, and Marc Kantorow. Mechanisms of organelle elimination for lens development and differentiation. *Exp. Eye Res.*, 209:108682, 2021.

[6] Mireille Delaye and Annette Tardieu. Short-range order of crystallin proteins accounts for eye lens transparency. *Nature*, 302(5907):415–417, 1983.

[7] EA Hermans, M Dubbelman, GL Van der Heijde, and RM Heethaar. Change in the accommodative force on the lens of the human eye with age. *Vision Res.*, 48(1): 119–126, 2008.

[8] Niels Lynnerup, Henrik Kjeldsen, Steffen Heegaard, Christina Jacobsen, and Jan Heinemeier. Radiocarbon dating of the human eye lens crystallines reveal proteins without carbon turnover throughout life. *PloS One*, 3(1):e1529, 2008.

[9] Daniel A Goodenough. The crystalline lens: A system networked by gap junctional intercellular communication. *Semin. Cell Dev. Biol.*, 3(1):49–58, 1992.

[10] Peter G Hains and Roger JW Truscott. Post-translational modifications in the nuclear region of young, aged, and cataract human lenses. *J. Proteome Res.*, 6(10):3935–3943, 2007.

[11] Cameron M Lee and Natalie A Afshari. The global state of cataract blindness. *Curr. Opin. Ophthalmol.*, 28(1):98–103, 2017.

[12] Marc A Sprague-Piercy, Megan A Rocha, Ashley O Kwok, and Rachel W Martin. α-crystallins in the vertebrate eye lens: Complex oligomers and molecular chaperones. *Annu. Rev. Phys. Chem.*, 72:143–163, 2021.

[13] Stacy RA Hanson, Azeem Hasan, David L Smith, and Jean B Smith. The major in vivo modifications of the human water-insoluble lens crystallins are disulfide bonds, deamidation, methionine oxidation and backbone cleavage. *Exp. Eye Res.*, 71(2):195–207, 2000.

[14] Martin Haslbeck, Jirka Peschek, Johannes Buchner, and Sevil Weinkauf. Structure and function of α-crystallins: Traversing from in vitro to in vivo. *Biochim. Biophys. Acta - Gen. Subj.*, 1860(1):149–166, 2016.

[15] Joseph Horwitz. Alpha-crystallin can function as a molecular chaperone. *PNAS*, 89 (21):10449–10453, 1992.

[16] Robert C Augusteyn. α-crystallin: a review of its structure and function. *Clin. Exp. Optom.*, 87(6):356–366, 2004.

[17] Eugene Serebryany and Jonathan A King. The $\beta\gamma$-crystallins: Native state stability and pathways to aggregation. *Prog. Biophys. Mol. Biol.*, 115(1):32–41, 2014.

[18] Rainer Jaenicke and Christine Slingsby. Lens crystallins and their microbial homologs: structure, stability, and function. *Crit. Rev. Biochem. Mol. Biol.*, 36(5):435–499, 2001.

[19] Christine Slingsby and OA Bateman. Quaternary interactions in eye lens beta-crystallins: basic and acidic subunits of beta-crystallins favor heterologous association. *Biochem.*, 29(28):6592–6599, 1990.

[20] Zhaoyong Xi, Matthew J Whitley, and Angela M Gronenborn. Human βB2-crystallin forms a face-en-face dimer in solution: an integrated NMR and SAXS study. *Structure*, 25(3):496–505, 2017.

[21] Christine Slingsby and Naommi J Clout. Structure of the crystallins. *Eye*, 13(3): 395–402, 1999.

[22] Graeme Wistow. The human crystallin gene families. *Hum. Genomics*, 6(1):1–10, 2012.

[23] Kyle W Roskamp, David M Montelongo, Chelsea D Anorma, Diana N Bandak, Janine A Chua, Kurtis T Malecha, and Rachel W Martin. Multiple aggregation pathways in human γS-crystallin and its aggregation-prone G18V variant. *Investig. Ophthalmol. Vis. Sci.*, 58(4):2397–2405, 2017.

[24] Marc A Sprague-Piercy, Eric Wong, Kyle W Roskamp, Joseph N Fakhoury, J Alfredo Freites, Douglas J Tobias, and Rachel W Martin. Human αB-crystallin discriminates between aggregation-prone and function-preserving variants of a client protein. *Biochim. Biophys. Acta - Gen. Subj.*, 1864(3):129502, 2020.

[25] Roger JW Truscott and Michael G Friedrich. The etiology of human age-related cataract. Proteins don't last forever. *Biochim. Biophys. Acta - Gen. Subj.*, 1860(1): 192–198, 2016.

[26] Megan A Rocha, Marc A Sprague-Piercy, Ashley O Kwok, Kyle W Roskamp, and Rachel W Martin. Chemical properties determine solubility and stability in $\beta\gamma$-crystallins of the eye lens. *ChemBioChem*, 22(8):1329–1346, 2021.

[27] Terrence Geiger and S Clarke. Deamidation, isomerization, and racemization at asparaginyl and aspartyl residues in peptides. Succinimide-linked reactions that contribute to protein degradation. *Int. J. Biol. Chem.*, 262(2):785–794, 1987.

[28] Kirsten J Lampi, Phillip A Wilmarth, Matthew R Murray, and Larry L David. Lens β-crystallins: the role of deamidation and related modifications in aging and cataract. *Prog. Biophys. Mol. Biol.*, 115(1):21–31, 2014.

[29] Xiaojuan Li, Cheng Lin, and Peter B O'Connor. Glutamine deamidation: differentiation of glutamic acid and γ-glutamic acid in peptides by electron capture dissociation. *Anal. Chem.*, 82(9):3606–3615, 2010.

[30] Aida Serra, Xavier Gallart-Palau, Juan Wei, and Siu Kwan Sze. Characterization of glutamine deamidation by long-length electrostatic repulsion-hydrophilic interaction chromatography-tandem mass spectrometry in shotgun proteomics. *Anal. Chem.*, 88 (21):10573–10582, 2016.

[31] Noriko Fujii, Takumi Takata, Norihiko Fujii, and Kenzo Aki. Isomerization of aspartyl residues in crystallins and its influence upon cataract. *Biochim. Biophys. Acta - Gen. Subj.*, 1860(1):183–191, 2016.

[32] Yuanqi Tao and Ryan R Julian. Identification of amino acid epimerization and isomerization in crystallin proteins by tandem LC-MS. *Anal. Chem.*, 86(19):9733–9741, 2014.

[33] Peter G Hains and Roger JW Truscott. Proteomic analysis of the oxidation of cysteine residues in human age-related nuclear cataract lenses. *Biochim. Biophys. Acta Proteins Proteom.*, 1784(12):1959–1964, 2008.

[34] Lisa J Alcock, Michael V Perkins, and Justin M Chalker. Chemical methods for mapping cysteine oxidation. *RIC Reviews*, 47(1):231–268, 2018.

[35] Kyle W Roskamp, Sana Azim, Gunther Kassier, Brenna Norton-Baker, Marc A Sprague-Piercy, RJ Dwyane Miller, and Rachel W Martin. Human γS-crystallin–copper binding helps buffer against aggregation caused by oxidative damage. *Biochem.*, 59(25):2371–2385, 2020.

[36] Usha P Andley. Crystallins in the eye: function and pathology. *Prog. Retin. Eye Res.*, 26(1):78–98, 2007.

[37] Hideaki Morishita and Noboru Mizushima. Autophagy in the lens. *Exp. Eye Res.*, 144:22–28, 2016.

[38] Hideaki Morishita, Tomoya Eguchi, Satoshi Tsukamoto, Yuriko Sakamaki, Satoru Takahashi, Chieko Saito, Ikuko Koyama-Honda, and Noboru Mizushima. Organelle degradation in the lens by plaat phospholipases. *Nature*, 592(7855):634–638, 2021.

[39] Hans Bloemendal, Wilfried de Jong, Rainer Jaenicke, Nicolette H Lubsen, Christine Slingsby, and Annette Tardieu. Ageing and vision: structure, stability and function of lens crystallins. *Prog. Biophys. Mol. Biol.*, 86(3):407–485, 2004.

[40] Graeme J Wistow and Joram Piatigorsky. Lens crystallins: the evolution and expression of proteins for a highly specialized tissue. *Annu. Rev. Biochem.*, 57(1):479–504, 1988.

[41] Christine Slingsby, Graeme J Wistow, and Alice R Clark. Evolution of crystallins for a role in the vertebrate eye lens. *Protein Sci.*, 22(4):367–380, 2013.

[42] Yu-Chi Liu, Mark Wilkins, Terry Kim, Boris Malyugin, and Jodhbir S Mehta. Cataracts. *Lancet*, 390(10094):600–612, 2017.

[43] Surendra Dasari, Phillip A Wilmarth, Ashok P Reddy, Lucinda JG Robertson, Srinivasa R Nagalla, and Larry L David. Quantification of isotopically overlapping deamidated and 18O-labeled peptides using isotopic envelope mixture modeling. *J. Proteome Res.*, 8(3):1263–1270, 2009.

[44] Kirsten J Lampi, Zhixiang Ma, Stacy RA Hanson, Misuyoshi Azuma, Marjorie Shih, Thomas R Shearer, David L Smith, Jean B Smith, and Larry L David. Age-related changes in human lens crystallins identified by two-dimensional electrophoresis and mass spectrometry. *Exp. Eye Res.*, 67(1):31–43, 1998.

[45] OP Srivastava, K Srivastava, JM Chaves, and AK Gill. Post-translationally modified human lens crystallin fragments show aggregation in vitro. *Biochem. Biophys. Rep.*, 10:94–131, 2017.

[46] PA Wilmarth, S Tanner, S Dasari, SR Nagalla, MA Riviere, V Bafna, PA Pevzner, and LL David. Age-related changes in human crystallins determined from comparative analysis of post-translational modifications in young and aged lens: does deamidation contribute to crystallin insolubility? *J. Proteome Res.*, 5(10):2554–2566, 2006.

[47] Michael G Friedrich, Zhen Wang, Kevin L Schey, and Roger JW Truscott. Spontaneous cleavage at Glu and Gln residues in long-lived proteins. *ACS Chem. Biol.*, 16(11):2244–2254, 2021.

[48] Shannon L Flaugh, Ishara A Mills, and Jonathan King. Glutamine deamidation destabilizes human γD-crystallin and lowers the kinetic barrier to unfolding. *J. Biol. Chem.*, 281(41):30782–30793, 2006.

[49] Heather M Forsythe, Calvin J Vetter, Kayla Ann Jara, Patrick N Reardon, Larry L David, Elisar J Barbar, and Kirsten J Lampi. Altered protein dynamics and increased aggregation of human γs-crystallin due to cataract-associated deamidations. *Biochem.*, 58(40):4112–4124, 2019.

[50] Kirsten J Lampi, Julie T Oxford, Hans Peter Bachinger, Thomas R Shearer, Larry L David, and Deborah M Kapfer. Deamidation of human βB1 alters the elongated structure of the dimer. *Exp. Eye Res.*, 72(3):279–288, 2001.

[51] Ajay Pande, Natalya Mokhor, and Jayanti Pande. Deamidation of human γS-crystallin increases attractive protein interactions: implications for cataract. *Biochem.*, 54(31): 4890–4899, 2015.

[52] Nicholas J Ray, Damien Hall, and John A Carver. Deamidation of N76 in human γS-crystallin promotes dimer formation. *Biochim. Biophys. Acta - Gen. Subj.*, 1860 (1):315–324, 2016.

[53] Takumi Takata, Julie T Oxford, Borries Demeler, and Kirsten J Lampi. Deamidation destabilizes and triggers aggregation of a lens protein, βA3-crystallin. *Protein Sci.*, 17 (9):1565–1575, 2008.

[54] Calvin J Vetter, David C Thorn, Samuel G Wheeler, Charlie C Mundorff, Kate A Halverson, Thomas E Wales, Ujwal P Shinde, John R Engen, Larry L David, John A Carver, et al. Cumulative deamidations of the major lens protein γS-crystallin increase its aggregation during unfolding and oxidation. *Protein Sci.*, 29(9):1945–1963, 2020.

[55] Stacy Hanson, David L Smith, and Jean B Smith. Deamidation and disulfide bonding in human lens γ-crystallins. *Exp. Eye Res.*, 67(3):301–312, 1998.

[56] Michelle Yu Sung Hooi, Mark J Raftery, and Roger John Willis Truscott. Age-dependent deamidation of glutamine residues in human γS crystallin: Deamidation and unstructured regions. *Protein Sci.*, 21(7):1074–1079, 2012.

[57] Veniamin N Lapko, Andrew G Purkiss, David L Smith, and Jean B Smith. Deamidation in human γS-crystallin from cataractous lenses is influenced by surface exposure. *Biochem.*, 41(27):8638–8648, 2002.

[58] Larry Takemoto, Daniel Boyle, et al. Increased deamidation of asparagine during human senile cataractogenesis. *Mol. Vis.*, 6:164–168, 2000.

[59] Takumi Takata, Julie T Oxford, Theodore R Brandon, and Kirsten J Lampi. Deamidation alters the structure and decreases the stability of human lens βA3-crystallin. *Biochem.*, 46(30):8861–8871, 2007.

[60] Kirsten J Lampi, Kencee K Amyx, Petra Ahmann, and Eric A Steel. Deamidation in human lens βB2-crystallin destabilizes the dimer. *Biochem.*, 45(10):3146–3153, 2006.

[61] Brian C Searle, Surendra Dasari, Phillip A Wilmarth, Mark Turner, Ashok P Reddy, Larry L David, and Srinivasa R Nagalla. Identification of protein modifications using MS/MS de novo sequencing and the opensea alignment algorithm. *J. Proteome Res.*, 4(2):546–554, 2005.

[62] Alex J Guseman, Matthew J Whitley, Jeremy J González, Nityam Rathi, Mikayla Ambarian, and Angela M Gronenborn. Assessing the structures and interactions of γD-crystallin deamidation variants. *Structure*, 29(3):284–291, 2021.

[63] Eugene Serebryany, Shuhuai Yu, Sunia A Trauger, Bogdan Budnik, and Eugene I Shakhnovich. Dynamic disulfide exchange in a crystallin protein in the human eye lens promotes cataract-associated aggregation. *Int. J. Biol. Chem.*, 293(46):17997–18009, 2018.

[64] David C Thorn, Aidan B Grosas, Peter D Mabbitt, Nicholas J Ray, Colin J Jackson, and John A Carver. The structure and stability of the disulfide-linked γs-crystallin dimer provide insight into oxidation products associated with lens cataract formation. *J. Mol. Biol.*, 431(3):483–497, 2019.

[65] Kyle W Roskamp, Natalia Kozlyuk, Suvrajit Sengupta, Jan C Bierma, and Rachel W Martin. Divalent cations and the divergence of $\beta\gamma$-crystallin function. *Biochem.*, 58 (45):4505–4518, 2019.

[66] Arline Fernández-Silva, Leidys French-Pacheco, Lina Rivillas-Acevedo, and Carlos Amero. Aggregation pathways of human γD crystallin induced by metal ions revealed by time dependent methods. *PeerJ*, 8:e9178, 2020.

[67] Liliana Quintanar, Jose A Domínguez-Calva, Eugene Serebryany, Lina Rivillas-Acevedo, Cameron Haase-Pettingell, Carlos Amero, and Jonathan A King. Copper and zinc ions specifically promote nonamyloid aggregation of the highly stable human γ-D crystallin. *ACS Chem. Biol.*, 11(1):263–272, 2016.

[68] William D Brubaker and Rachel W Martin. 1H, 13C, and 15N assignments of wild-type human γS-crystallin and its cataract-related variant γS-G18V. *Biomol. NMR Assign.*, 6(1):63–67, 2012.

[69] F William Studier. Protein production by auto-induction in high-density shaking cultures. *Protein Expr. Purif.*, 41(1):207–234, 2005.

[70] Thaiesha A Wright, Jamie M Stewart, Richard C Page, and Dominik Konkolewicz. Extraction of thermodynamic parameters of protein unfolding using parallelized differential scanning fluorimetry. *J. Phys. Chem. Lett.*, 8(3):553–558, 2017.

[71] Kevin N Dyer, Michal Hammel, Robert P Rambo, Susan E Tsutakawa, Ivan Rodic, Scott Classen, John A Tainer, and Greg L Hura. High-throughput SAXS for the characterization of biomolecules in solution: a practical approach. In *Methods Mol. Biol.*, pages 245–258. Springer, 2014.

[72] Greg L Hura, Angeli L Menon, Michal Hammel, Robert P Rambo, Farris L Poole Ii, Susan E Tsutakawa, Francis E Jenney Jr, Scott Classen, Kenneth A Frankel, Robert C Hopkins, et al. Robust, high-throughput solution structural analyses by small angle X-ray scattering (SAXS). *Nat. Methods*, 6(8):606–612, 2009.

[73] Cy M Jeffries, Melissa A Graewert, Clément E Blanchet, David B Langley, Andrew E Whitten, and Dmitri I Svergun. Preparing monodisperse macromolecular samples for successful biological small-angle X-ray and neutron-scattering experiments. *Nat. Protoc.*, 11(11):2122–2153, 2016.

[74] Michel HJ Koch, Patrice Vachette, and Dmitri I Svergun. Small-angle scattering: a view on the properties, structures and structural changes of biological macromolecules in solution. *Q. Rev. Biophys.*, 36(2):147–227, 2003.

[75] D Vivarès and Françoise Bonnete. X-ray scattering studies of aspergillus flavus urate oxidase: towards a better understanding of PEG effects on the crystallization of large proteins. *Acta Crystallogr. D*, 58(3):472–479, 2002.

[76] Fabrice Gorrec. The MORPHEUS protein crystallization screen. *J. Appl. Crystallogr.*, 42(6):1035–1042, 2009.

[77] Wolfgang Kabsch. XDS. *Acta Crystallogr. D*, 66(2):125–132, 2010.

[78] Airlie J McCoy, Ralf W Grosse-Kunstleve, Paul D Adams, Martyn D Winn, Laurent C Storoni, and Randy J Read. Phaser crystallographic software. *J. Appl. Crystallogr.*, 40(4):658–674, 2007.

[79] Paul Emsley, Bernhard Lohkamp, William G Scott, and Kevin Cowtan. Features and development of Coot. *Acta Crystallogr. D*, 66(4):486–501, 2010.

[80] Dorothee Liebschner, Pavel V Afonine, Matthew L Baker, Gábor Bunkóczi, Vincent B Chen, Tristan I Croll, Bradley Hintze, L-W Hung, Swati Jain, Airlie J McCoy, et al. Macromolecular structure determination using X-rays, neutrons and electrons: recent developments in Phenix. *Acta Crystallogr. D*, 75(10):861–877, 2019.

[81] Sanbo Qin and Huan-Xiang Zhou. Calculation of second virial coefficients of atomistic proteins using fast fourier transform. *J. Phys. Chem. B*, 123(39):8203–8215, 2019.

[82] Carolyn N Kingsley, William D Brubaker, Stefan Markovic, Anne Diehl, Amanda J Brindley, Hartmut Oschkinat, and Rachel W Martin. Preferential and specific binding of human αB-crystallin to a cataract-related variant of γS-crystallin. *Structure*, 21 (12):2221–2227, 2013.

[83] Andrew G Purkiss, Orval A Bateman, Julia M Goodfellow, Nicolette H Lubsen, and Christine Slingsby. The X-ray crystal structure of human γS-crystallin C-terminal domain. *J. Biol. Chem.*, 277(6):4199–4205, 2002.

[84] R Stevens, L Stevens, and NC Price. The stabilities of various thiol compounds used in protein purifications. *Biochem. Educ.*, 11(2):70, 1983.

[85] Ajay Pande, Jayanti Pande, Neer Asherie, Aleksey Lomakin, Olutayo Ogun, Jonathan King, and George B Benedek. Crystal cataracts: human genetic cataract caused by protein crystallization. *PNAS*, 98(11):6116–6120, 2001.

[86] Brenna Norton-Baker, Pedram Mehrabi, Juliane Boger, Robert Schönherr, David von Stetten, Hendrik Schikora, Ashley O Kwok, Rachel W Martin, RJ Dwayne Miller, Lars Redecke, et al. A simple vapor-diffusion method enables protein crystallization inside the HARE serial crystallography chip. *Acta Crystallogr. D*, 77(6), 2021.

[87] Byungkook Lee and Frederic M Richards. The interpretation of protein structures: estimation of static accessibility. *J. Mol. Biol.*, 55(3):379–IN4, 1971.

[88] Martyn D Winn, Charles C Ballard, Kevin D Cowtan, Eleanor J Dodson, Paul Emsley, Phil R Evans, Ronan M Keegan, Eugene B Krissinel, Andrew GW Leslie, Airlie McCoy, et al. Overview of the CCP4 suite and current developments. *Acta Crystallogr. D*, 67 (4):235–242, 2011.

[89] Song-Ho Chong and Sihyun Ham. Interaction with the surrounding water plays a key role in determining the aggregation propensity of proteins. *Angew. Chem. Int. Ed.*, 53 (15):3961–3964, 2014.

[90] Song-Ho Chong and Sihyun Ham. Distinct role of hydration water in protein misfolding and aggregation revealed by fluctuating thermodynamics analysis. *Acc. Chem. Res.*, 48(4):956–965, 2015.

[91] Ojore BV Oka, Hui Y Yeoh, and Neil J Bulleid. Thiol-disulfide exchange between the pdi family of oxidoreductases negates the requirement for an oxidase or reductase for each enzyme. *Biochem. J.*, 469(2):279–288, 2015.

[92] Bonney Wilkinson and Hiram F Gilbert. Protein disulfide isomerase. *Biochim. Biophys. Acta - Gen. Subj.*, 1699(1-2):35–44, 2004.

[93] Fang Huang and Werner M Nau. A conformational flexibility scale for amino acids in peptides. *Angew. Chem. Int. Ed.*, 42(20):2269–2272, 2003.

[94] Martijn van Rosmalen, Mike Krom, and Maarten Merkx. Tuning the flexibility of glycine-serine linkers to allow rational design of multidomain proteins. *Biochem.*, 56 (50):6565–6574, 2017.

[95] Ernest Awoonor-Williams and Christopher N Rowley. Evaluation of methods for the calculation of the pKa of cysteine residues in proteins. *J. Chem. Theory Comput.*, 12 (9):4662–4673, 2016.

[96] Grzegorz Bulaj, Tanja Kortemme, and David P Goldenberg. Ionization-reactivity relationships for cysteine thiols in polypeptides. *Biochem.*, 37(25):8965–8972, 1998.

[97] Péter Nagy. Kinetics and mechanisms of thiol–disulfide exchange covering direct substitution and thiol oxidation-mediated pathways. *Antioxid. Redox Signal.*, 18(13): 1623–1641, 2013.

[98] Surapong Pinitglang, Aaron B Watts, Manij Patel, James D Reid, Michael A Noble, Sheraz Gul, Anjumon Bokth, Akavish Naeem, Hasu Patel, Emrys W Thomas, et al. A classical enzyme active center motif lacks catalytic competence until modulated electrostatically. *Biochem.*, 36(33):9968–9982, 1997.

[99] Mats HM Olsson, Chresten R Søndergaard, Michal Rostkowski, and Jan H Jensen. PROPKA3: Consistent treatment of internal and surface residues in empirical pKa predictions. *J. Chem. Theory Comput.*, 7(2):525–537, 2011.

[100] Chresten R Søndergaard, Mats HM Olsson, Michał Rostkowski, and Jan H Jensen. Improved treatment of ligands and coupling effects in empirical calculation and rationalization of p k a values. *J. Chem. Theory Comput.*, 7(7):2284–2295, 2011.

[101] Freya Q Schafer and Garry R Buettner. Redox environment of the cell as viewed through the redox state of the glutathione disulfide/glutathione couple. *Free Radic. Biol.*, 30(11):1191–1212, 2001.

[102] Lukasz Goldschmidt, David R Cooper, Zygmunt S Derewenda, and David Eisenberg. Toward rational protein crystallization: A web server for the design of crystallizable protein variants. *Protein Sci.*, 16(8):1569–1576, 2007.

[103] Brandon H Toyama, Jeffrey N Savas, Sung Kyu Park, Michael S Harris, Nicholas T Ingolia, John R Yates III, and Martin W Hetzer. Identification of long-lived proteins reveals exceptional stability of essential cellular structures. *Cell*, 154(5):971–982, 2013.

[104] Dor Ben-Amotz. Hydrophobic ambivalence: Teetering on the edge of randomness. *J. Phys. Chem. Lett.*, 6:1696–1701, 2015.

[105] Joel G. Davis, Kamil P. Gierszal, Ping Wang, and Dor Ben-Amotz. Water structural transformation at molecular hydrophobic interfaces. *Nature*, 491:582–585, 2012.

[106] P. N. Perera, K. R. Fega, C. Lawrence, E. J. Sundstrom, J. Tomlinson-Phillips, and Dor Ben-Amotz. Observation of water dangling OH bonds around dissolved nonpolar groups. *Proc. Natl. Acad. Sci. U. S. A.*, 106(30):12230–12234, 2009.

[107] Kamil P. Gierszal, Joel G. Davis, Michael D. Hands, David S. Wilcox, Lyudmila V. Slipchenko, and Dor Ben-Amotz. π-hydrogen bonding in liquid water. *J. Phys. Chem. Lett.*, 2:2930–2933, 2011.

[108] E. W. Knapp and I. Muegge. Heterogeneous diffusion of water at protein surfaces: Application to BPTI. *J. Phys. Chem.*, 97:11339–11343, 1993.

[109] Kuo-Ying Huang, Carolyn N. Kingsley, Ryan Sheil, Chi-Yuan Cheng, Jan C. Bierma, Kyle W. Roskamp, Domarin Khago, Rachel W. Martin, and Songi Han. Stability of protein-specific hydration shell on crowding. *J. Am. Chem. Soc.*, 138:5392–5402, 2016.

[110] Ryan Barnes, Sheng Sun, Yann Fichou, Frederick W. Dahlquist, Matthias Heyden, and Songi Han. Spatially heterogeneous surface water diffusivity around structured protein surfaces at equilibrium. *J. Am. Chem. Soc.*, 139(49):17890–17901, 2017.

[111] D. P. Kharakoz and A. P. Sarvazyan. Hydrational and intrinsic compressibilities of globular proteins. *Biopolymers*, 33:11–26, 1993.

[112] Domarin Khago, Jan C. Bierma, Kyle W. Roskamp, Natalia Kozlyuk, and Rachel W. Martin. Protein refractive index increment is determined by conformation as well as composition. *J. Phys.: Condens. Matter*, 30(43):435101, 2018.

[113] P. Ball. Water as an active constituent in cell biology. *Chem. Rev.*, 108(1):74–108, 2008.

[114] F. Akif Tezcan, Brian R. Crane, Jay R. Winkler, and Harry B. Gray. Electron tunneling in protein crystals. *Proc. Natl. Acad. Sci. U. S. A.*, 98(9):5002–5006, 2001.

[115] Fabian Hecker, JoAnne Stubbe, and Marina Bennati. Detection of water molecules on the radical transfer pathway of ribonucleotide reductase by ^{17}O electron-nuclear double resonance spectroscopy. *J. Am. Chem. Soc.*, 143:7237–7241, 2021.

[116] Jay A. LaVerne. OH radicals and oxidizing products in the gamma radiolysis of water. *Radiat. Res.*, 153:196–200, 2000.

[117] D. Ghosal, M.V. Omelchenko, E.K. Gaidamakova, Matrosova V.Y., A. Vasilenko, A. Venkateswaran, M. Zhai, H.M. Kostandarithes, H. Brim, and K.S*etal* Makarova. How radiation kills cells: Survival of *Deinococcus radiodurans* and *Shewanella oneidensis* under oxidative stress. *FEMS Microbiol. Rev.*, 29:361–375, 2005.

[118] Juan Du and Janusz M. Gebicki. Proteins are major initial cell targets of hydroxyl free radicals. *Int. J. Biochem. Cell Biol.*, 36(11):2334–2343, 2004.

[119] M.J. Davies, S. Fu, and R. T. Dean. Protein hydroperoxides can give rise to reactive free radicals. *Biochem. J.*, 305(2):643–649, 1995.

[120] Courtney K. Robinson, Kim Webb, Amardeep Kaur, Pawel Jaruga, Miral Dizdaroglu, Nitin S. Baliga, Allen Place, and Jocelyne Diruggiero. A major role for nonenzymatic antioxidant processes in the radioresistance of *Halobacterium salinarum*. *J. Bacteriol.*, 193(7):1653–1662, 2011.

[121] Alexandra-Cristina Munteanu, Valentina Uivarosi, and Adrian Andries. Recent progress in understanding the molecular mechanisms of radioresistance in *Deinococcus* bacteria. *Extremophiles*, 9(4):707–719, 2015.

[122] Sandeep Kumar Shukla, Ajay Kumar Sharma, Sania Bajaj, and M.H. Yashavarddhan. Radiation proteome: A clue to protection, carcinogenesis, and drug development. *Drug Discov. Today*, 26(2):525–531, 2021.

[123] Richard M Lipman, Brenda J. Tripathi, and Ramesh C. Tripathi. Cataracts induced by microwave and ionizing radiation. *Surv. Ophthalmol.*, 33(3):200–210, 1988.

[124] Marie-Odile Bernier, Neige Journy, Daphnee Villoing, Michele M Doody, Bruce H Alexander, Martha S Linet, and Cari M Kitahara. Cataract risk in a cohort of us radiologic technologists performing nuclear medicine procedures. *Radiology*, 286(2): 592–601, 2018.

[125] Leo T Chylack Jr, Leif E Peterson, Alan H Feiveson, Mary L Wear, F Keith Manuel, William H Tung, Dale S Hardy, Lisa J Marak, and Francis A Cucinotta. NASA study of cataract in astronauts (NASCA). Report 1: Cross-sectional study of the relationship of exposure to space radiation and risk of lens opacity. *Radiat. Res.*, 172(1):10–20, 2009.

[126] Eiji Nakashima, Kazuo Neriishi, and Atsushi Minamoto. A reanalysis of atomic-bomb cataract data, 2000–2002: A threshold analysis. *Health Phys.*, 90(2):154–160, 2006.

[127] Kazuo Neriishi, Eiji Nakashima, Atsushi Minamoto, Saeko Fujiwara, Masazumi Akahoshi, Hiromu K Mishima, Takashi Kitaoka, and Roy E Shore. Postoperative cataract cases among atomic bomb survivors: Radiation dose response and threshold. *Radiat. Res.*, 168(4):404–408, 2007.

[128] Gaël P. Hammer, Ulrike Scheidemann-Wesp, Florence Samkange-Zeeb, Henryk Wicke, Kazuo Neriishi, and Maria Blettner. Occupational exposure to low doses of ionizing radiation and cataract development: A systematic literature review and perspectives on future studies. *Radiat. Environ. Biophys.*, 52(3):303–319, 2013.

[129] Nobuyuki Hamada, Yuki Fujimichi, Toshiyasu Iwasaki, Noriko Fujii, Masato Furuhashi, Eri Kubo, Tohru Minamino, Takaharu Nomura, and Hitoshi Sato. Emerging issues in radiogenic cataracts and cardiovascular disease. *J. Radiat. Res.*, 55(5):831–846, 2014.

[130] Samantha Cornacchia, Rosangela Errico, Luciana La Tegola, Arcangela Maldera, Giovanni Simeone, Vincenzo Fusco, Artor Niccoli-Asabella, Giuseppe Rubini, and Giuseppe Guglielmi. The new lens dose limit: Implication for occupational radiation protection. *La Radiologia Medica*, 124(8):728–735, 2019.

[131] Per P. Fagerholm, Bo T. Philipson, and Bo Lindström. Normal human lens-the distribution of protein. *Exp. Eye Res.*, 33(6):615–620, 1981.

[132] Ingu Kim, Takeshi Saito, Norihiko Fujii, Takashi Kanamoto, Toshiyuki Chatake, and Noriko Fujii. Site specific oxidation of amino acid residues in rat lens γ-crystallin induced by low-dose γ-irradiation. *Biochem. Biophys. Res. Commun.*, 466(4):622–628, 2015.

[133] Srinivasagan Ramkumar, Noriko Fujii, Norihiko Fujii, Bency Thankappan, Hiroaki Sakaue, Kim Ingu, Kalimuthusamy Natarajaseenivasan, and Kumarasamy Anbarasu. Comparison of effect of gamma ray irradiation on wild-type and N-terminal mutants of αA-crystallin. *Mol. Vision*, 20:1002, 2014.

[134] W. M. Ross, M. O. Creighton, W. R. Inch, and J. R. Trevithick. Radiation cataract formation diminished by vitamin E in rat lenses in vitro. *Exp. Eye Res.*, 36(5):645–653, 1983.

[135] W. M. Ross, M. O. Creighton, and J. R. Trevithick. Radiation cataractogenesis induced by neutron or gamma irradiation in the rat lens is reduced by vitamin E. *Scanning Microsc.*, 4(3):13, 1990.

[136] Seyithan Taysi, Ramazan Memisogullari, Mehmet Koc, Ahmet Taylan Yazici, Murat Aslankurt, Kenan Gumustekin, Behçet Al, Fatma Ozabacigil, Adnan Yilmaz, and Hasan Tahsin Ozder. Melatonin reduces oxidative stress in the rat lens due to radiation-induced oxidative injury. *Int. J. Radiat. Biol.*, 84(10):803–808, 2008.

[137] Hideaki Morishita, Tomoya Eguchi, Satoshi Tsukamoto, Yuriko Sakamaki, Satoru Takahashi, Chieko Saito, Ikuko Koyama-Honda, and Noboru Mizushima. Organelle degradation in the lens by PLAAT phospholipases. *Nature*, 592:634–638, 2021.

[138] Steven Bassnett. On the mechanism of organelle degradation in the vertebrate lens. *Exp. Eye Res.*, 88(2):133–139, 2009.

[139] Frank J Giblin. Glutathione: a vital lens antioxidant. *J. Ocul. Pharmacol. Ther.*, 16 (2):121–135, 2000.

[140] Veronica Harrington, Shantis McCall, Sy Huynh, Kiran Srivastava, and Om P Srivastava. Crystallins in water soluble-high molecular weight protein fractions and water insoluble protein fractions in aging and cataractous human lenses. *Mol. Vision*, 10 (61):476–489, 2004.

[141] Jiejin Chen, Shannon L Flaugh, Patrik R Callis, and Jonathan King. Mechanism of the highly efficient quenching of tryptophan fluorescence in human γD-crystallin. *Biochem.*, 45(38):11552–11563, 2006.

[142] Jiejin Chen, Dmitri Toptygin, Ludwig Brand, and Jonathan King. Mechanism of the efficient tryptophan fluorescence quenching in human γD-crystallin studied by time-resolved fluorescence. *Biochem.*, 47(40):10705–10721, 2008.

[143] Jiejin Chen, Patrik R Callis, and Jonathan King. Mechanism of the very efficient quenching of tryptophan fluorescence in human γD-and γS-crystallins: the γ-crystallin fold may have evolved to protect tryptophan residues from ultraviolet photodamage. *Biochem.*, 48(17):3708–3716, 2009.

[144] Randy Ngelale, Christopher Lee, Steven Bustillos, and Mikael Nilsson. Radiolytic degradation of uranyl-loaded tributyl phosphate by high and low let radiation. *Solvent Extr. Ion Exch.*, 37(1):38–52, 2019.

[145] Christopher C. Perry, José Ramos-Méndez, and Jamie R. Milligan. Boronated condensed DNA as a heterochromatic radiation target model. *Biomacromolecules*, 22: 1675–1684, 2021.

[146] Hugo Fricke and Sterne Morse. The chemical action of roentgen rays on dilute ferrosulphate solutions as a measure of dose. *Am. J. Roentgenol., Radium Ther. Nucl. Med.*, 18:430–432, 1927.

[147] Ridthee Meesat, Sunuchakan Sanguanmith, Jintana Meesungnoen, Martin Lepage, Abdelouahed Khalil, and Jean-Paul Jay-Gerin. Utilization of the ferrous sulfate (fricke) dosimeter for evaluating the radioprotective potential of cystamine: Experiment and monte carlo simulation. *Radiat. Res.*, 177(6):813–826, 2012.

[148] George L Ellman. Tissue sulfhydryl groups. *Arch. Biochem. Biophys.*, 82(1):70–77, 1959.

[149] Peter W. Riddles, Robert L. Blakeley, and Burt Zerner. Ellman's reagent: 5, 5'-dithiobis (2-nitrobenzoic acid)–A reexamination. *Anal. Biochem.*, 94(1):75–81, 1979.

[150] AJ Miles, Robert W Janes, and Bonnie A Wallace. Tools and methods for circular dichroism spectroscopy of proteins: a tutorial review. *Chem. Soc. Rev.*, 50:8400–8413, 2021.

[151] William D. Brubaker, J. Alfredo Freites, Kory J. Golchert, Rebecca A. Shapiro, Vasilios Morikis, Douglas J. Tobias, and Rachel W. Martin. Separating instability from aggregation propensity in γS-crystallin variants. *Biophys. J.*, 100(2):498–506, 2011.

[152] K Mandal, B Chakrabarti, J Thomson, and RJ Siezen. Structure and stability of gamma-crystallins. denaturation and proteolysis behavior. *J. Biol. Chem.*, 262(17): 8096–8102, 1987.

[153] Steven S-S Wang and Wen-Sing Wen. Examining the influence of ultraviolet C irradiation on recombinant human γD-crystallin. *Mol. Vision*, 16:2777, 2010.

[154] Norihiko Fujii, Tooru Nakamura, Yutaka Sadakane, Takeshi Saito, and Noriko Fujii. Differential susceptibility of alpha a-and alpha b-crystallin to gamma-ray irradiation. *Biochim. Biophys. Acta, Proteins Proteomics*, 1774(3):345–350, 2007.

[155] Alexis Vallée-Bélisle and Stephen W. Michnick. Visualizing transient protein-folding intermediates by tryptophan-scanning mutagenesis. *Nat. Struct. Mol. Biol.*, 19(7): 731–736, 2012.

[156] Yasutsugu Fukunaga, Yasuhiro Katsuragi, Takashi Izumi, and Fumio Sakiyama. Fluorescence characteristics of kynurenine and N'-formylkynurenine, their use as reporters of the environment of tryptophan 62 in hen egg-white lysozyme. *J. Biochem.*, 92(1): 129–141, 1982.

[157] A. O. Bateman, R. Sarra, S. T. Van Genesen, G. Kappe, N. H. Lubsen, and C. Slingsby. The stability of human acidic β-crystallin oligomers and hetero-oligomers. *Exp. Eye Res.*, 77(4):409–422, 2003.

[158] Shannon L Flaugh, Melissa S Kosinski-Collins, and Jonathan King. Contributions of hydrophobic domain interface interactions to the folding and stability of human γd-crystallin. *Protein Sci.*, 14(3):569–581, 2005.

[159] Melissa S Kosinski-Collins, Shannon L Flaugh, and Jonathan King. Probing folding and fluorescence quenching in human γD crystallin greek key domains using triple tryptophan mutant proteins. *Protein Sci.*, 13(8):2223–2235, 2004.

[160] Heather M. Forsythe, Calvin J. Vetter, Kayla Ann Jara, Patrick N. Reardon, Larry L. David, Elisar J. Barbar, and Kirsten J. Lampi. Altered protein dynamics and increased aggregation of human γS-crystallin due to cataract-associated deamidations. *Biochem.*, 58:4112–4124, 2019.

[161] Mikhail Linetsky and BJ Ortwerth. Quantitation of the singlet oxygen produced by UVA irradiation of human lens proteins. *Photochem. Photobiol.*, 65(3):522–529, 1997.

[162] S Zigman. Environmental near-UV radiation and cataracts. *Optom. and Vis. Sci.*, 3 (49):182, 1996.

[163] John M.C. Gutteridge and Stephanie Wilkins. Copper salt dependent hydroxyl radical formation damage to proteins acting as antioxidants. *Biochim. Biophys. Acta, Gen. Subj.*, 759:38–41, 1983.

[164] Barry Halliwell and John M.C. Gutteridge. The antioxidants of human extracellular fluids. *Arch. Biochem. Biophys.*, 280(1):1–8, 1990.

[165] Michael R. Gunther, Phillip M. Hanna, Ronald P. Mason, and Myron S. Cohen. Hydroxyl radical formation fron cuprous ion and hydrogen peroxide: A spin-trapping study. *Arch. Biochem. Biophys.*, 316:515–522, 1995.

[166] Kevin J. Barnham, Colin L. Masters, and Ashley I. Bush. Neurodegenerative diseases and oxidative stress. *Nat. Rev. Drug Discovery*, 3:205–214, 2004.

[167] Roger T Dean, Shanlin FU, Roland Socker, and Michael J Davies. Biochemistry and pathology of radical-mediated protein oxidation. *Biochem. J.*, 324(1):1–18, 1997.

[168] Michael J Davies. Protein oxidation and peroxidation. *Biochem. J.*, 473(7):805–825, 2016.

[169] K. Uchida. Histidine and lysine as targets of oxidative modification. *Amino Acids*, 25 (3-4):249–257, 2003.

[170] Samuel H Yong and Marcus Karel. Reactions between peroxidizing lipids and histidyl residue analogues: Enhancement of lipid oxidation and browning by 4-methylimidazole. *Lipids*, 13(1):1–5, 1978.

[171] Earl R Stadtman and Rodney L Levine. *Redox proteomics: from protein modifications to cellular dysfunction and diseases*, volume 9. John Wiley & Sons Hoboken NJ, 2006. 1–23 pp.

[172] Guozhong Xu and Mark R Chance. Hydroxyl radical-mediated modification of proteins as probes for structural proteomics. *Chem. Rev.*, 107(8):3514–3543, 2007.

[173] Guozhong Xu, Keiji Takamoto, and Mark R Chance. Radiolytic modification of basic amino acid residues in peptides: Probes for examining protein-protein interactions. *Anal. Chem.*, 75(24):6995–7007, 2003.

[174] Danté T Johnson, Luciano H Di Stefano, and Lisa M Jones. Fast photochemical oxidation of proteins (FPOP): A powerful mass spectrometry–based structural proteomics tool. *J. Biol. Chem.*, 294(32):11969–11979, 2019.

[175] Hao Zhang, Brian C Gau, Lisa M Jones, Ilan Vidavsky, and Michael L Gross. Fast photochemical oxidation of proteins for comparing structures of protein-ligand complexes: the calmodulin-peptide model system. *Anal. Chem.*, 83(1):311–318, 2011.

[176] Lisa M Jones, Justin B. Sperry, James A. Carroll, and Michael L Gross. Fast photochemical oxidation of proteins for epitope mapping. *Anal. Chem.*, 83(20):7657–7661, 2011.

[177] Amina S Woods, Hay-Yan J Wang, and Shelley N Jackson. Sulfation, the up-and-coming post-translational modification: Its role and mechanism in protein-protein interaction. *J. Proteome Res.*, 6(3):1176–1182, 2007.

[178] K. F. Medzihradszky, Z. Darula, E. Perlson, Michael Fainzilber, R. J. Chalkley, H. Ball, D. Greenbaum, M. Bogyo, D. R. Tyson, R. A. Bradshaw, and A. L. Burlingame. O-sulfonation of serine and threonine: Mass spectrometric detection and characterization of a new posttranslational modification in diverse proteins throughout the eukaryotes. *Mol. Cell. Proteomics*, 3(5):429–440, 2004.

[179] Dana W. Aswad, Mallik V. Paranandi, and Brandon T. Schurter. Isoaspartate in peptides and proteins: Formation, significance, and analysis. *J. Pharm. Biomed. Anal.*, 21(6):1129–1136, 2000.

[180] R.A. Warmack, H. Shawa, K. Liu, K. Lopez, J.A. Loo, J. Horwitz, and S.G. Clarke. The L-isoaspartate modification within protein fragments in the aging lens can promote protein aggregation. *J. Biol. Chem.*, 294:12203–12219, 2019.

[181] Noriko Fujii, Hiroki Uchida, and Takeshi Saito. The damaging effect of UV-C irradiation on lens alpha-crystallin. *Mol. Vision*, 10:814–820, 2004.

[182] N. Fujii, K. Hiroki, S. Matsumoto, K. Masuda, M. Inoue, Y. Tanaka, M. Awakura, and M. Akaboshi. Correlation between the loss of the chaperone-like activity and the oxidation, isomerization and racemization of gamma-irradiated α-crystallin. *Photochem. Photobiol.*, 74(3):477–482, 2001.

[183] Hee-Jung Kim, Sura Ha, Hee Yoon Lee, and Kong-Joo Lee. Rosics: Chemistry and proteomics of cysteine modifications in redox biology. *Mass Spectrom. Rev.*, 34(2): 184–208, 2015.

[184] S. Gebicki and J. M .Gebicki. Formation of peroxides in amino acids and proteins exposed to oxygen free radicals. *Biochem. J.*, 289(3):743–749, 1993.

[185] Jude C. Lakbub, Joshua T. Shipman, and Heather Desaire. Recent mass spectrometry-based techniques and considerations for disulfide bond characterization in proteins. *Anal. Bioanal. Chem.*, 410(10):2467–2484, 2018.

[186] Jesús R Requena, Chien-Chung Chao, Rodney L Levine, and Earl R Stadtman. Glutamic and aminoadipic semialdehydes are the main carbonyl products of metal-catalyzed oxidation of proteins. *Proc. Natl. Acad. Sci. U. S. A.*, 98(1):69–74, 2001.

[187] Xingjun Fan, Jianye Zhang, Mathilde Theves, Christopher Strauch, Ina Nemet, Xiaoqin Liu, Juan Qian, Frank J Giblin, and Vincent M Monnier. Mechanism of lysine oxidation in human lens crystallins during aging and in diabetes. *J. Biol. Chem.*, 284 (50):34618–34627, 2009.

[188] Joshua S Sharp and Kenneth B Tomer. Effects of anion proximity in peptide primary sequence on the rate and mechanism of leucine oxidation. *Anal. Chem.*, 78(14):4885–4893, 2006.

[189] Michael J Davies and Roger JW Truscott. Photo-oxidation of proteins and its role in cataractogenesis. *J. Photochem. Photobiol., B*, 63(1-3):114–125, 2001.

[190] Michael J Davies. Singlet oxygen-mediated damage to proteins and its consequences. *Biochem. Biophys. Res. Commun.*, 305(3):761–770, 2003.

[191] Eric L Finley, Mark Busman, James Dillon, Rosalie K Crouch, and Kevin L Schey. Identification of photooxidation sites in bovine α-crystallin. *Photochem. Photobiol.*, 66 (5):635–641, 1997.

[192] Nathaniel Schafheimer, Zhen Wang, Kevin Schey, and Jonathan King. Tyrosine/cysteine cluster sensitizing human γD-crystallin to ultraviolet radiation-induced photoaggregation in vitro. *Biochem.*, 53(6):979–990, 2014.

[193] Adina Elena Segneanu, Ioan Gozescu, Anamaria Dabici, Paula Sfirloaga, and Zoltan Szabadai. *Organic compounds FT-IR spectroscopy*, volume 145. InTechOpen, Rijeka, 2012. 145–164 pp.

[194] Adolfo Amici, RL Levine, Lin Tsai, and ER Stadtman. Conversion of amino acid residues in proteins and amino acid homopolymers to carbonyl derivatives by metal-catalyzed oxidation reactions. *J. Biol. Chem.*, 264(6):3341–3346, 1989.

[195] Jackob Moskovitz and Derek B Oien. Protein carbonyl and the methionine sulfoxide reductase system. *Antioxid. Redox Signaling*, 12(3):405–415, 2010.

[196] Yuanchao Liu, Tristan Asset, Yechuan Chen, Eamonn Murphy, Eric O Potma, Ivana Matanovic, Dmitry A Fishman, and Plamen Atanassov. Facile all-optical method for in situ detection of low amounts of ammonia. *Iscience*, 23(11):101757, 2020.

[197] Dongmao Zhang, Yong Xie, Melissa F. Mrozek, Corasi Ortiz, V. Jo Davisson, and Dor Ben-Amotz. Raman detection of proteomic analytes. *Anal. Chem.*, 75(21):5703–5709, 2003.

[198] Halina M Zbikowska, Pawel Nowak, and Barbara Wachowicz. Protein modification caused by a high dose of gamma irradiation in cryo-sterilized plasma: Protective effects of ascorbate. *Free Radical Biol. Med.*, 40(3):536–542, 2006.

[199] Béatrice Sjöberg, Sarah Foley, Bruno Cardey, Michel Fromm, and Mironel Enescu. Methionine oxidation by hydrogen peroxide in peptides and proteins: A theoretical and raman spectroscopy study. *J. Photochem. Photobiol., B*, 188:95–99, 2018.

[200] Kevin L Schey, Zhen Wang, Michael G Friedrich, and Roger JW Truscott. New insights into the mechanisms of age-related protein-protein crosslinking in the human lens. *Exp. Eye Res.*, 209:108679, 2021.

[201] Michael G Friedrich, Zhen Wang, Kevin L Schey, and Roger JW Truscott. Spontaneous cross-linking of proteins at aspartate and asparagine residues is mediated via a succinimide intermediate. *Biochem. J.*, 475(20):3189–3200, 2018.

[202] C. Giulivi, N. J. Traaseth, and K. J. A. Davies. Tyrosine oxidation products: Analysis and biological relevance. *Amino Acids*, 25(3-4):227–232, 2003.

[203] J. W. Heinecke, W. Li, G. A. Francis, and J. A. Goldstein. Tyrosyl radical generated by myeloperoxidase catalyzes the oxidative cross-linking of proteins. *J. Clin. Invest.*, 91(6):2866–2872, 1993.

[204] Henry N Chapman. X-ray free-electron lasers for the structure and dynamics of macromolecules. *Annu. Rev. Biochem.*, 88:35–58, 2019.

[205] Henry N Chapman, Petra Fromme, Anton Barty, Thomas A White, Richard A Kirian, Andrew Aquila, Mark S Hunter, Joachim Schulz, Daniel P DePonte, Uwe Weierstall, et al. Femtosecond X-ray protein nanocrystallography. *Nature*, 470(7332):73–77, 2011.

[206] Lars Redecke, Karol Nass, Daniel P DePonte, Thomas A White, Dirk Rehders, Anton Barty, Francesco Stellato, Mengning Liang, Thomas RM Barends, Sébastien Boutet, et al. Natively inhibited trypanosoma brucei cathepsin b structure determined by using an X-ray laser. *Science*, 339(6116):227–230, 2013.

[207] Karol Nass, Lars Redecke, M Perbandt, O Yefanov, M Klinge, R Koopmann, F Stellato, A Gabdulkhakov, R Schönherr, D Rehders, et al. In cellulo crystallization of trypanosoma brucei imp dehydrogenase enables the identification of genuine co-factors. *Nat. Commun.*, 11(1):1–13, 2020.

[208] Jason Tenboer, Shibom Basu, Nadia Zatsepin, Kanupriya Pande, Despina Milathianaki, Matthias Frank, Mark Hunter, Sébastien Boutet, Garth J Williams, Jason E Koglin, et al. Time-resolved serial crystallography captures high-resolution intermediates of photoactive yellow protein. *Science*, 346(6214):1242–1246, 2014.

[209] Thomas RM Barends, Lutz Foucar, Albert Ardevol, Karol Nass, Andrew Aquila, Sabine Botha, R Bruce Doak, Konstantin Falahati, Elisabeth Hartmann, Mario Hilpert, et al. Direct observation of ultrafast collective motions in CO myoglobin upon ligand dissociation. *Science*, 350(6259):445–450, 2015.

[210] Eriko Nango, Antoine Royant, Minoru Kubo, Takanori Nakane, Cecilia Wickstrand, Tetsunari Kimura, Tomoyuki Tanaka, Kensuke Tono, Changyong Song, Rie Tanaka, et al. A three-dimensional movie of structural changes in bacteriorhodopsin. *Science*, 354(6319):1552–1557, 2016.

[211] Kanupriya Pande, Christopher DM Hutchison, Gerrit Groenhof, Andy Aquila, Josef S Robinson, Jason Tenboer, Shibom Basu, Sébastien Boutet, Daniel P DePonte, Mengning Liang, et al. Femtosecond structural dynamics drives the trans/cis isomerization in photoactive yellow protein. *Science*, 352(6286):725–729, 2016.

[212] Eike C Schulz, Pedram Mehrabi, Henrike M Müller-Werkmeister, Friedjof Tellkamp, Ajay Jha, William Stuart, Elke Persch, Raoul De Gasparo, François Diederich, Emil F Pai, et al. The hit-and-return system enables efficient time-resolved serial synchrotron crystallography. *Nature methods*, 15(11):901–904, 2018.

[213] Pedram Mehrabi, Eike C Schulz, Michael Agthe, Sam Horrell, Gleb Bourenkov, David von Stetten, Jan-Philipp Leimkohl, Hendrik Schikora, Thomas R Schneider, Arwen R Pearson, et al. Liquid application method for time-resolved analyses by serial synchrotron crystallography. *Nature methods*, 16(10):979–982, 2019.

[214] Pedram Mehrabi, Eike C Schulz, Raison Dsouza, Henrike M Müller-Werkmeister, Friedjof Tellkamp, RJ Dwayne Miller, and Emil F Pai. Time-resolved crystallography reveals allosteric communication aligned with molecular breathing. *Science*, 365 (6458):1167–1170, 2019.

[215] Tobias Weinert, Petr Skopintsev, Daniel James, Florian Dworkowski, Ezequiel Panepucci, Demet Kekilli, Antonia Furrer, Steffen Brünle, Sandra Mous, Dmitry Ozerov, et al. Proton uptake mechanism in bacteriorhodopsin captured by serial synchrotron crystallography. *Science*, 365(6448):61–65, 2019.

[216] Marie Luise Grünbein and Gabriela Nass Kovacs. Sample delivery for serial crystallography at free-electron lasers and synchrotrons. *Acta Crystallogr. D*, 75(2):178–191, 2019.

[217] Isabelle Martiel, Henrike M Müller-Werkmeister, and Aina E Cohen. Strategies for sample delivery for femtosecond crystallography. *Acta Crystallogr. D*, 75(2):160–177, 2019.

[218] Sébastien Boutet, Lukas Lomb, Garth J Williams, Thomas RM Barends, Andrew Aquila, R Bruce Doak, Uwe Weierstall, Daniel P DePonte, Jan Steinbrener, Robert L Shoeman, et al. High-resolution protein structure determination by serial femtosecond crystallography. *Science*, 337(6092):362–364, 2012.

[219] Mark S Hunter, Brent Segelke, Marc Messerschmidt, Garth J Williams, Nadia A Zatsepin, Anton Barty, W Henry Benner, David B Carlson, Matthew Coleman, Alexander Graf, et al. Fixed-target protein serial microcrystallography with an X-ray free electron laser. *Scientific reports*, 4(1):1–5, 2014.

[220] Saeed Oghbaey, Antoine Sarracini, Helen M Ginn, Olivier Pare-Labrosse, Anling Kuo, Alexander Marx, Sascha W Epp, Darren A Sherrell, Bryan T Eger, Yinpeng Zhong, et al. Fixed target combined with spectral mapping: approaching 100% hit rates for serial crystallography. *Acta Crystallogr. D*, 72(8):944–955, 2016.

[221] Bradley Davy, Danny Axford, John H Beale, Agata Butryn, Peter Docker, Ali Ebrahim, Gabriel Leen, Allen M Orville, Robin L Owen, and Pierre Aller. Reducing sample consumption for serial crystallography using acoustic drop ejection. *J. Synchrotron Radiat.*, 26(5):1820–1825, 2019.

[222] A Tolstikova, M Levantino, O Yefanov, V Hennicke, P Fischer, J Meyer, A Mozzanica, S Redford, E Crosas, NL Opara, et al. 1 kHz fixed-target serial crystallography using a multilayer monochromator and an integrating pixel detector. *IUCrJ*, 6(5):927–937, 2019.

[223] Robin L Owen, Danny Axford, Darren A Sherrell, Anling Kuo, Oliver P Ernst, Eike C Schulz, RJ Dwayne Miller, and Henrike M Mueller-Werkmeister. Low-dose fixed-target serial synchrotron crystallography. *Acta Crystallogr. D*, 73(4):373–378, 2017.

[224] Darren A Sherrell, Andrew J Foster, Lee Hudson, Brian Nutter, James O'Hea, Silke Nelson, Olivier Paré-Labrosse, Saeed Oghbaey, RJ Dwayne Miller, and Robin L Owen. A modular and compact portable mini-endstation for high-precision, high-speed fixed target serial crystallography at fel and synchrotron sources. *J. Synchrotron Radiat.*, 22(6):1372–1378, 2015.

[225] Janine Mia Lahey-Rudolph, Robert Schönherr, Cy M Jeffries, Clément E Blanchet, Juliane Boger, Ana Sofia Ferreira Ramos, Winnie Maria Riekehr, D-P Triandafillidis, Alexandros Valmas, Irene Margiolaki, et al. Rapid screening of in cellulo grown protein crystals via a small-angle X-ray scattering/X-ray powder diffraction synergistic approach. *J. Appl. Crystallogr.*, 53(5), 2020.

[226] Robert Schönherr, Janine Mia Rudolph, and Lars Redecke. Protein crystallization in living cells. *Biol. Chem.*, 399(7):751–772, 2018.

[227] Pedram Mehrabi, Henrike M Müller-Werkmeister, J-P Leimkohl, Hendrik Schikora, Jelena Ninkovic, Silvia Krivokuca, Ladislav Andriček, Sascha W Epp, Darren Sherrell, Robin L Owen, et al. The HARE chip for efficient time-resolved serial synchrotron crystallography. *J. Synchrotron Radiat.*, 27(2):360–370, 2020.

[228] Eike C Schulz, Johannes Kaub, Frederik Busse, Pedram Mehrabi, Henrike M Müller-Werkmeister, Emil F Pai, Wesley D Robertson, and RJ Dwayne Miller. Protein crystals IR laser ablated from aqueous solution at high speed retain their diffractive properties:

Applications in high-speed serial crystallography. *J. Appl. Crystallogr.*, 50(6):1773–1781, 2017.

[229] Marina Lučić, Dimitri A Svistunenko, Michael T Wilson, Amanda K Chaplin, Bradley Davy, Ali Ebrahim, Danny Axford, Takehiko Tosha, Hiroshi Sugimoto, Shigeki Owada, et al. Serial femtosecond zero dose crystallography captures a water-free distal heme site in a dye-decolorising peroxidase to reveal a catalytic role for an arginine in FeIV=O formation. *Angew. Chem. Int. Ed.*, 132(48):21840–21846, 2020.

[230] Tadeo Moreno-Chicano, Ali Ebrahim, Danny Axford, Martin V Appleby, John H Beale, Amanda K Chaplin, Helen ME Duyvesteyn, Reza A Ghiladi, Shigeki Owada, Darren A Sherrell, et al. High-throughput structures of protein–ligand complexes at room temperature using serial femtosecond crystallography. *IUCrJ*, 6(6):1074–1085, 2019.

[231] Ali Ebrahim, Martin V Appleby, Danny Axford, John Beale, Tadeo Moreno-Chicano, Darren A Sherrell, Richard W Strange, Michael A Hough, and Robin L Owen. Resolving polymorphs and radiation-driven effects in microcrystals using fixed-target serial synchrotron crystallography. *Acta Crystallogr. D*, 75(2):151–159, 2019.

[232] Ali Ebrahim, Tadeo Moreno-Chicano, Martin V Appleby, Amanda K Chaplin, John H Beale, Darren A Sherrell, Helen ME Duyvesteyn, Shigeki Owada, Kensuke Tono, Hiroshi Sugimoto, et al. Dose-resolved serial synchrotron and XFEL structures of radiation-sensitive metalloproteins. *IUCrJ*, 6(4):543–551, 2019.

[233] John H Beale, Rachel Bolton, Stephen A Marshall, Emma V Beale, Stephen B Carr, Ali Ebrahim, Tadeo Moreno-Chicano, Michael A Hough, Jonathan AR Worrall, Ivo Tews, et al. Successful sample preparation for serial crystallography experiments. *J. Appl. Crystallogr.*, 52(6):1385–1396, 2019.

[234] Rachel W Martin and Kurt W Zilm. Preparation of protein nanocrystals and their characterization by solid state NMR. *J. Magn. Reson.*, 165(1):162–174, 2003.

[235] Julia Lieske, Maximilian Cerv, Stefan Kreida, Dana Komadina, Janine Fischer, Miriam Barthelmess, Pontus Fischer, Tim Pakendorf, Oleksandr Yefanov, Valerio Mariani, et al. On-chip crystallization for serial crystallography experiments and on-chip ligand-binding studies. *IUCrJ*, 6(4):714–728, 2019.

[236] Andrew Arvai. Adxv. `https://www.scripps.edu/tainer/arvai/adxv.html/`, 2019.

[237] Thomas A White, Richard A Kirian, Andrew V Martin, Andrew Aquila, Karol Nass, Anton Barty, and Henry N Chapman. Crystfel: a software suite for snapshot serial crystallography. *J. Appl. Crystallogr.*, 45(2):335–341, 2012.

[238] Khandekar Jishan Bari, Shrikant Sharma, and Kandala VR Chary. Structure of G57W mutant of human γS-crystallin and its involvement in cataract formation. *J. Struct. Biol*, 205(3):72–78, 2019.

[239] Fériel Skouri-Panet, Françoise Bonneté, Karine Prat, Orval A Bateman, Nicolette H Lubsen, and Annette Tardieu. Lens crystallins and oxidation: the special case of γS. *Biophys. Chem.*, 89(1):65–76, 2001.

[240] Zhixiang Ma, Stacy RA Hanson, Kirsten J Lampi, Larry L David, David L Smith, and Jean B Smith. Age-related changes in human lens crystallins identified by HPLC and mass spectrometry. *Exp. Eye Res.*, 67(1):21–30, 1998.

[241] J Mia Lahey-Rudolph, Robert Schönherr, Miriam Barthelmess, Pontus Fischer, Carolin Seuring, Armin Wagner, Alke Meents, and Lars Redecke. Fixed-target serial femtosecond crystallography using in cellulo grown microcrystals. *IUCrJ*, 8(4), 2021.

[242] Karen Tenney, Ian Hunt, James Sweigard, June I Pounder, Chadonna McClain, Emma Jean Bowman, and Barry J Bowman. HEX-1, a gene unique to filamentous fungi, encodes the major protein of the woronin body and functions as a plug for septal pores. *Fungal Genet. Biol.*, 31(3):205–217, 2000.

[243] Ping Yuan, Gregory Jedd, Desigan Kumaran, Subramanyam Swaminathan, Helen Shio, David Hewitt, Nam-Hai Chua, and Kunchithapadam Swaminathan. A HEX-1 crystal lattice required for woronin body function in neurospora crassa. *Nat. Struct. Mol. Biol.*, 10(4):264–270, 2003.

[244] Artem Y Lyubimov, Thomas D Murray, Antoine Koehl, Ismail Emre Araci, Monarin Uervirojnangkoorn, Oliver B Zeldin, Aina E Cohen, S Michael Soltis, Elizabeth L Baxter, Aaron S Brewster, et al. Capture and X-ray diffraction studies of protein microcrystals in a microfluidic trap array. *Acta Crystallogr. D*, 71(4):928–940, 2015.

[245] Thomas D Murray, Artem Y Lyubimov, Craig M Ogata, Huy Vo, Monarin Uervirojnangkoorn, Axel T Brunger, and James M Berger. A high-transparency, micropatternable chip for X-ray diffraction analysis of microcrystals under native growth conditions. *Acta Crystallogr. D*, 71(10):1987–1997, 2015.

[246] Zhong Ren, Medine Ayhan, Sepalika Bandara, Kalinga Bowatte, Indika Kumarapperuma, Semini Gunawardana, Heewhan Shin, Cong Wang, Xiaoli Zeng, and Xiaojing Yang. Crystal-on-crystal chips for in situ serial diffraction at room temperature. *Lab on a Chip*, 18(15):2246–2256, 2018.

[247] Keondo Lee, Donghyeon Lee, Sangwon Baek, Jaehyun Park, Sang Jae Lee, Sehan Park, Wan Kyun Chung, J-L Lee, H-S Cho, Yunje Cho, et al. Viscous-medium-based crystal support in a sample holder for fixed-target serial femtosecond crystallography. *J. Appl. Crystallogr.*, 53(4), 2020.

[248] Nadia Opara, Isabelle Martiel, Stefan A Arnold, Thomas Braun, Henning Stahlberg, Mikako Makita, Christian David, and Celestino Padeste. Direct protein crystallization on ultrathin membranes for diffraction measurements at X-ray free-electron lasers. *J. Appl. Crystallogr.*, 50(3):909–918, 2017.

[249] P Mehrabi, R Bücker, G Bourenkov, HM Ginn, D von Stetten, HM Müller-Werkmeister, A Kuo, T Morizumi, BT Eger, W-L Ou, et al. Serial femtosecond and serial synchrotron crystallography can yield data of equivalent quality: A systematic comparison. *Sci. Adv.*, 7(12):eabf1380, 2021.

Appendix A

Supplementary material for *Deamidation of the human eye lens protein γS-crystallin accelerates oxidative aging*

Codon-optimized γS-wt sequence with NcoI and XhoI restriction sites:

```
CCATGGGACATCACCATCACCATCACGAAAATCTTTATTTTCAAGGCAGCAAAACGGGCACCAAAATCACGTTC
TACGAAGACAAAAATTTCCAAGGTCGCCGTTACGACTGTGACTGCGACTGTGCGGACTTCCACACATACCTGTC
CCGTTGCAACTCTATCAAAGTTGAAGGCGGCACCTGGGCTGTATACGAACGCCCGAACTTCGCTGGCTACATGT
ACATCCTTCCGCAGGGCGAATACCCGGAATACCAGCGCTGGATGGGTCTGAACGACCGTCTGTCGTCTTGCCGC
GCTGTACATCTGCCGTCCGGCGGTCAGTACAAAATCCAGATCTTCGAAAAAGGCGACTTCTCCGGCCAGATGTA
CGAAACCACCGAAGACTGCCCGTCTATCATGGAACAATTCCACATGCGCGAAATCCACTCTTGTAAAGTTCTGG
AAGGCGTATGGATCTTCTACGAACTGCCGAACTACCGCGGTCGCCAGTACCTGCTGGACAAAAAAGAATACCGC
AAACCGATCGACTGGGGCGCGGCCTCTCCGGCTGTACAGAGCTTCCGTCGTATCGTTGAATAATAACTCGAG
```

Primer	Sequence (5' to 3')
N15_fwd	GAC AAA GAT TTC CAA GGT CGC
N15_rev	GCG ACC TTG GAA ATC TTT GTC
Q121_fwd	ATC ATG GAA GAA TTC CAC ATG
Q121_rev	CAT GTG GAA TTC TTC CAT GAT
N144_fwd	TAC GAA CTG CCG GAC TAC
N144_rev	GTA GTC CGG CAG TTC GTA
N54D_fwd	CCG GAC TTC GCT GGC TAC ATG TAC ATC CTT CCG
N54D_rev	GCG TTC GTA TAC AGC CCA GGT GCC GCC TTC
Q93E_fwd	CGT CCG GCG GTG AGT ACA AAA TCC AGA TCT TCG AAA AAG GCG
Q93E_rev	GCA GAT GTA CAG CGC GGC AAG ACG ACA GAC GG
Q64E_fwd	CTT CCG GAG GGC GAA TAC CCG GAA TAC CAG C
Q64E_rev	GAT GTA CAT GTA GCC AGC GAA GTC CGG GCG TTC GTA TAC
Q17E_fwd	GAA GAC AAA GAT TTC GAA GGT CGC CGT TAC GAC TGT GAC TG
Q17E_rev	GTA GAA CGT GAT TTT GGT GCC CGT TTT GCT GCC TTG
Q107E_fwd	GGC GAG ATG TAC GAA ACC ACC GAA GAC TGC CCG TCT ATC
Q107E_rev	GGA GAA GTC GCC TTT TTC GAA GAT CTG GAT TTT GTA CTC ACC GCC G
Q71E_fwd	GGA ATA CGA GCG CTG GAT GGG TCT GAA CGA CCG TCT GTC G
Q71E_rev	GGG TAT TCG CCC TCC GGA AGG ATG TAC ATG TAG CCA GCG
codonY11_fwd	CAA AGA CTT CCA AGG TCG CCG TTA C
codonY11_fwd_2	CAA AGA CTT CGA AGG TCG CCG TTA C
codonY11_rev	TCT TCA TAG AAC GTG ATT TTG GTG CC

Figure A.1: Oligonucleotides for PCR mutagenesis. A mistranslation of Y11 was identified in the deamidated variants and was corrected by the application of primers codonY11_fwd to γS-3 and γS-5 and codonY11_fwd_2 to γS-7 and γS-9 with codonY11_rev used for all deamidated variants.

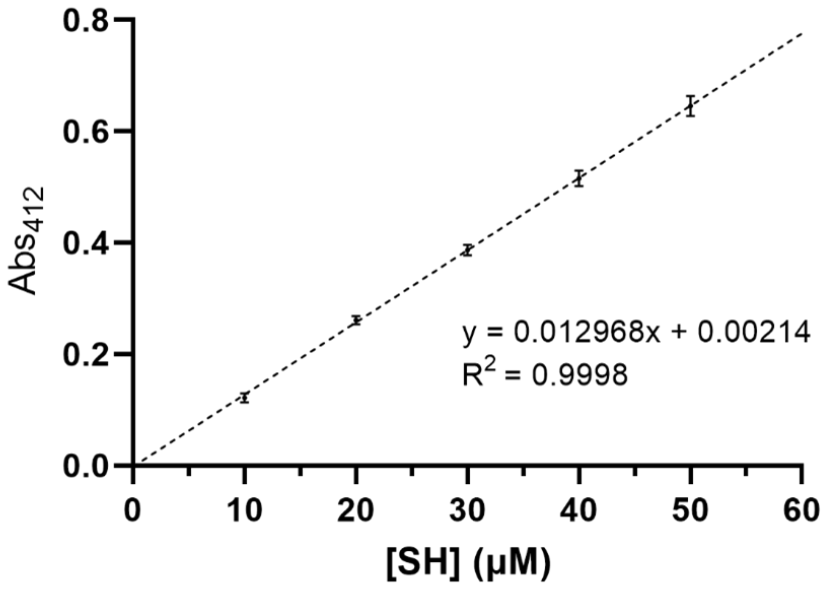

Figure A.2: Calibration curve for Ellman's assay in 2% SDS, 100 mM TRIS pH 8.0 using dithiothreitol (DTT). The concentration of thiol is 2× the concentration of DTT. The extinction coefficient calculated is 12968 $M^{-1}cm^{-1}$.

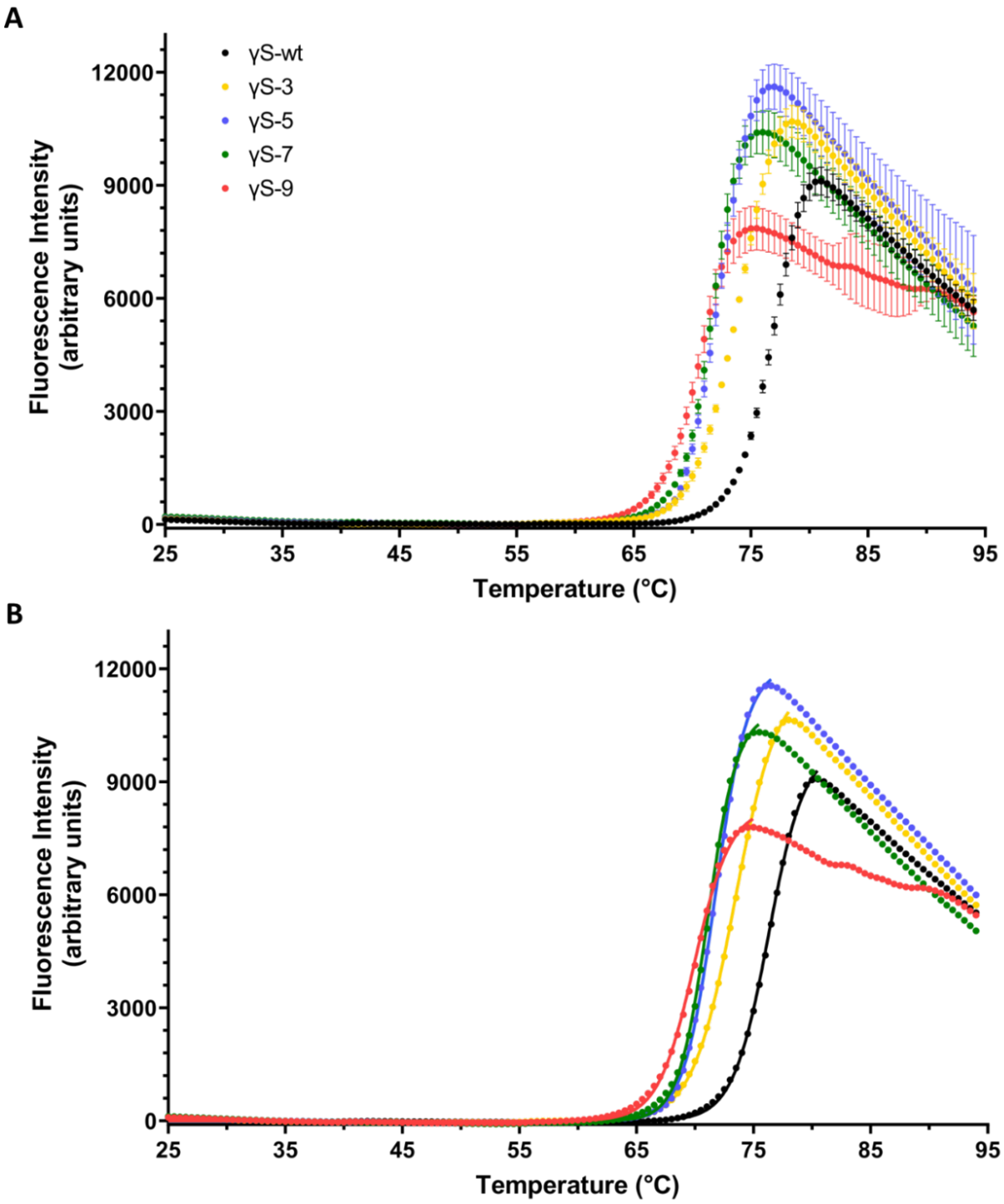

Figure A.3: (A) The average fluorescence intensity from three replicates measured by differential scanning fluorimetry (DSF) for γS-crystallin wild-type (γS-wt, black), 3-site (γS-3, yellow), 5-site (γS-5, blue), 7-site (γS-7, green), and 9-site deamidation variants (γS-9, pink). (B) The average fluorescence intensity for each protein with overlaid solid lines showing the Boltzmann fit curves calculated for each data set. Only the region of the DSF data up to the fluorescence maxima are used for the Boltzmann fit.

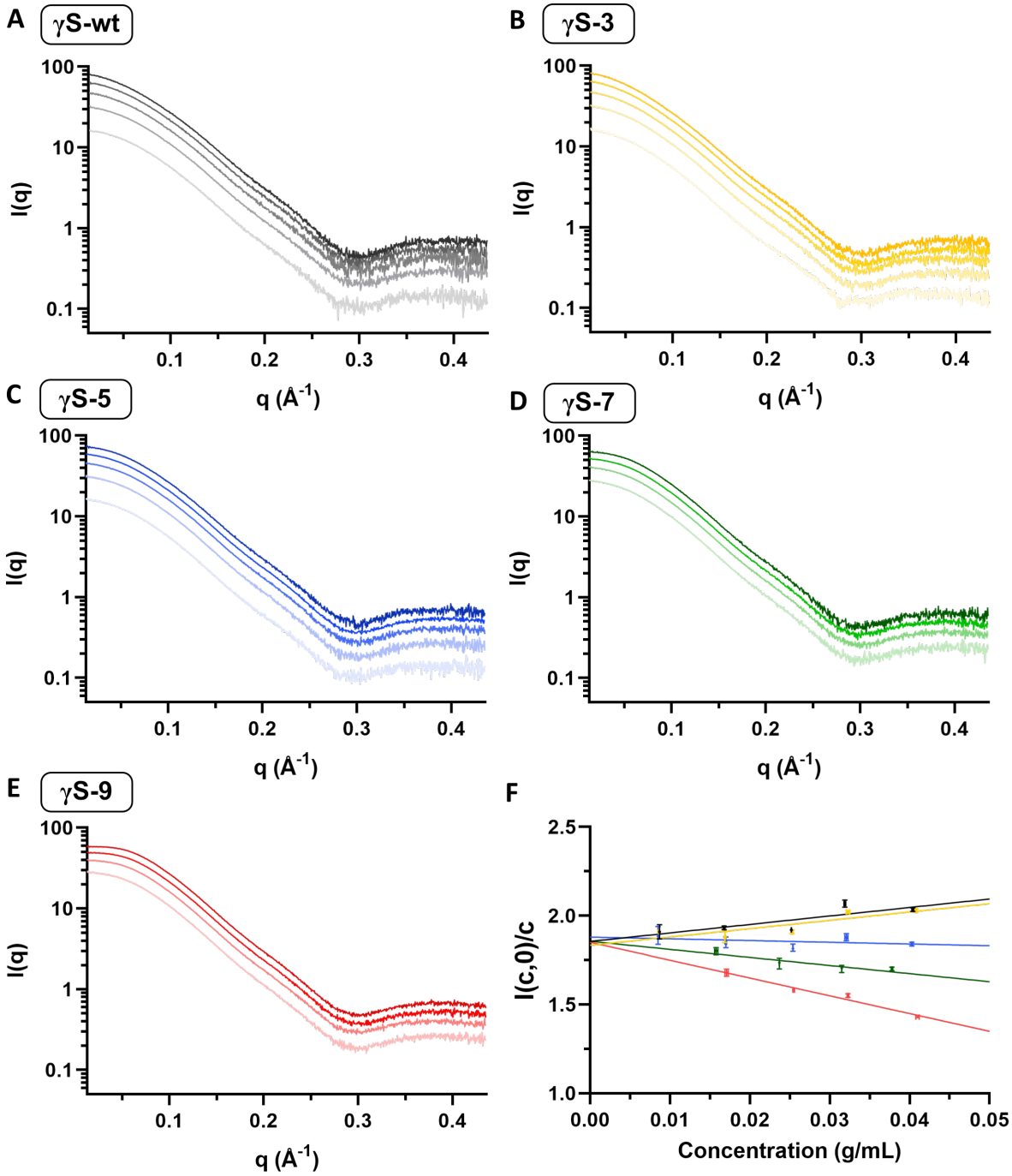

Figure A.4: SAXS profiles for (A) γS-wt, (B) γS-3. (C) γS-5, (D) γS-7, and (E) γS-9 with concentrations ranging from approximately 40 mg/mL down to either 16 mg/mL (γS-7 and γS-9) or 8 mg/mL (γS-wt, γS-3, and γS-5). Each concentration series was measured in triplicate. (F) The intensity at zero angle over concentration as a function of concentration. The y-intercept of the linear regression gives the intensity at zero angle extrapolated to zero concentration.

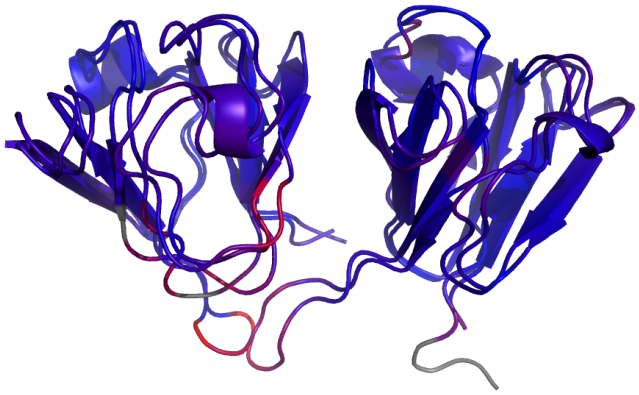

Figure A.5: Structure alignment of the previously reported NMR structure of γS-wt (PDB: 2M3T) and the novel crystal structure reported here (PDB:7N36). The script *colorbyrmsd* in Pymol was used to highlight areas of minimum pairwise RMSD in blue and maximum in red. The loop containing K154 and K155 as well as the linker region between domains show the maximum difference.

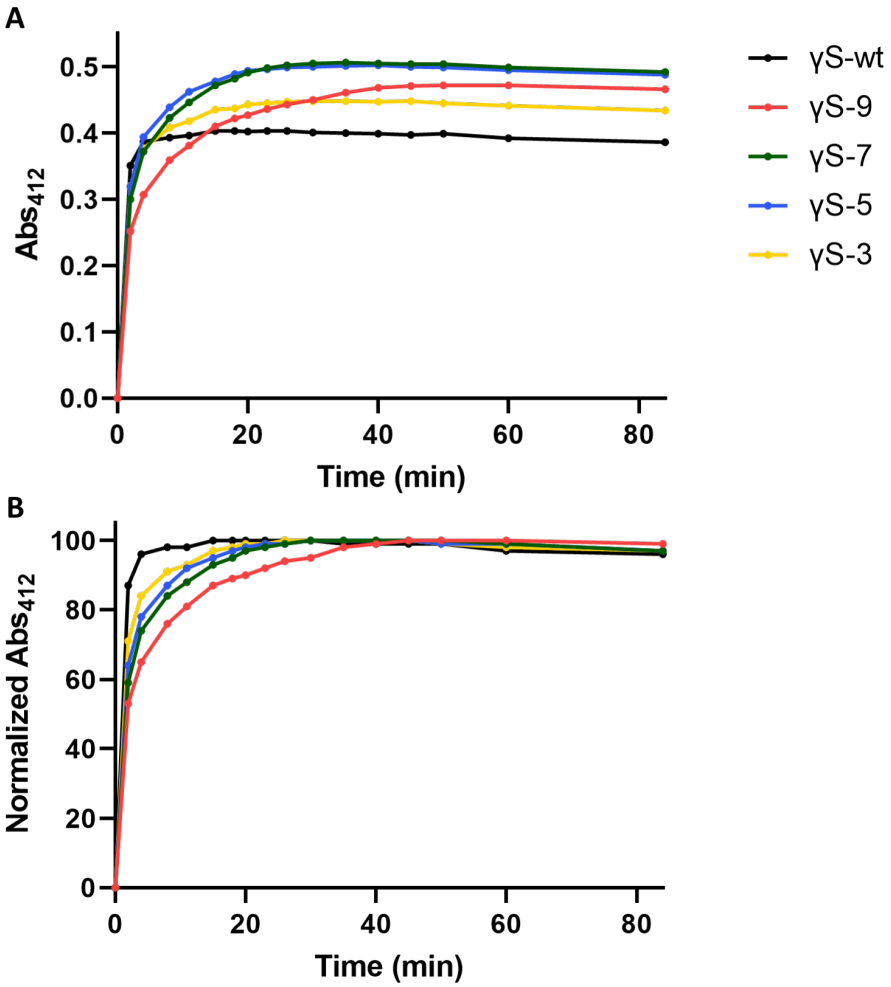

Figure A.6: (A) Absorbance at 412 nm after the addition of DTNB for γS-wt and each variant. (B) Normalized absorbance at 412 nm for each reaction. Increasing number of deamidated sites leads to longer reaction times to maximum Abs_{412}.

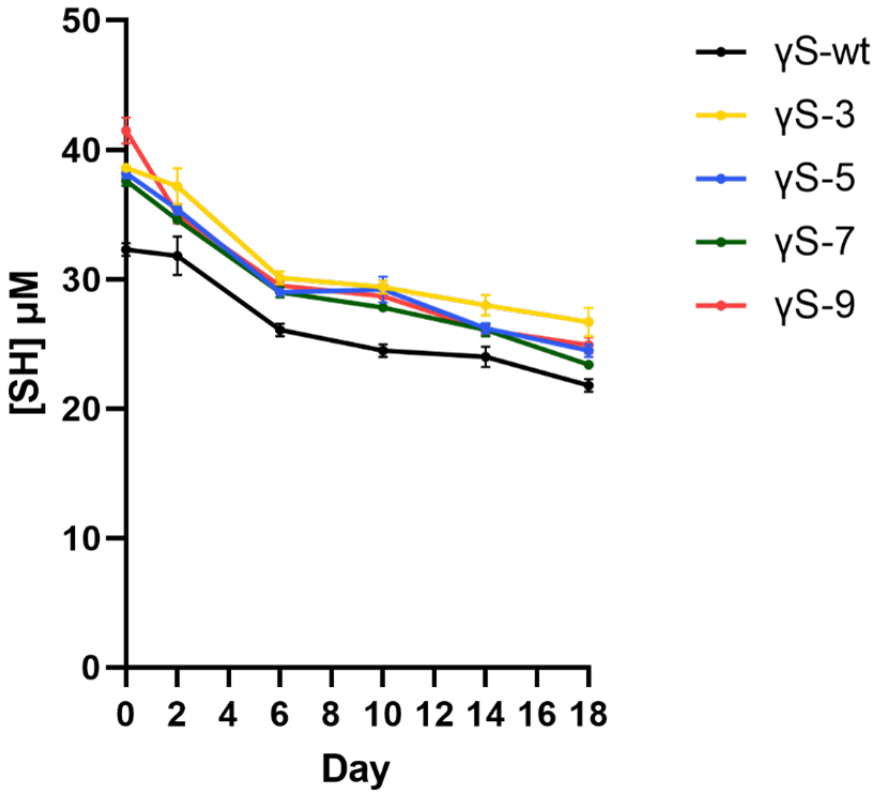

Figure A.7: (A) Assessment of free thiol concentration over time using Ellman's assay for γS-crystallin wild-type (γS-wt, black), 3-site (γS-3, yellow), 5-site (γS-5, blue), 7-site (γS-7, green), and 9-site deamidation variant (γS-9, pink). Proteins were aged at 210 – 250 µM which was diluted 40-fold for these measurements.

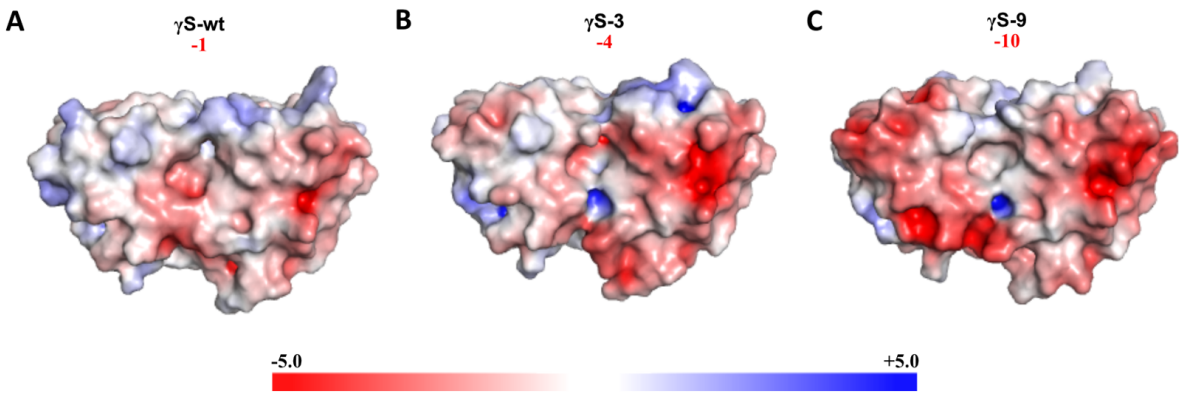

Figure A.8: (A) Adaptive Poisson-Boltzmann Solver (APBS) electrostatics calculation was used to generate surface charge maps in PyMol for (A) γS-wt PDB:7N36, (B) γS-3 PDB:7N37, and (C) γS-9B PDB:7N3B showing regions of high negative charge with increasing deamidation.

Appendix B

Supplementary material for *Human γS-crystallin resists unfolding despite extensive chemical modification from exposure to ionizing radiation*

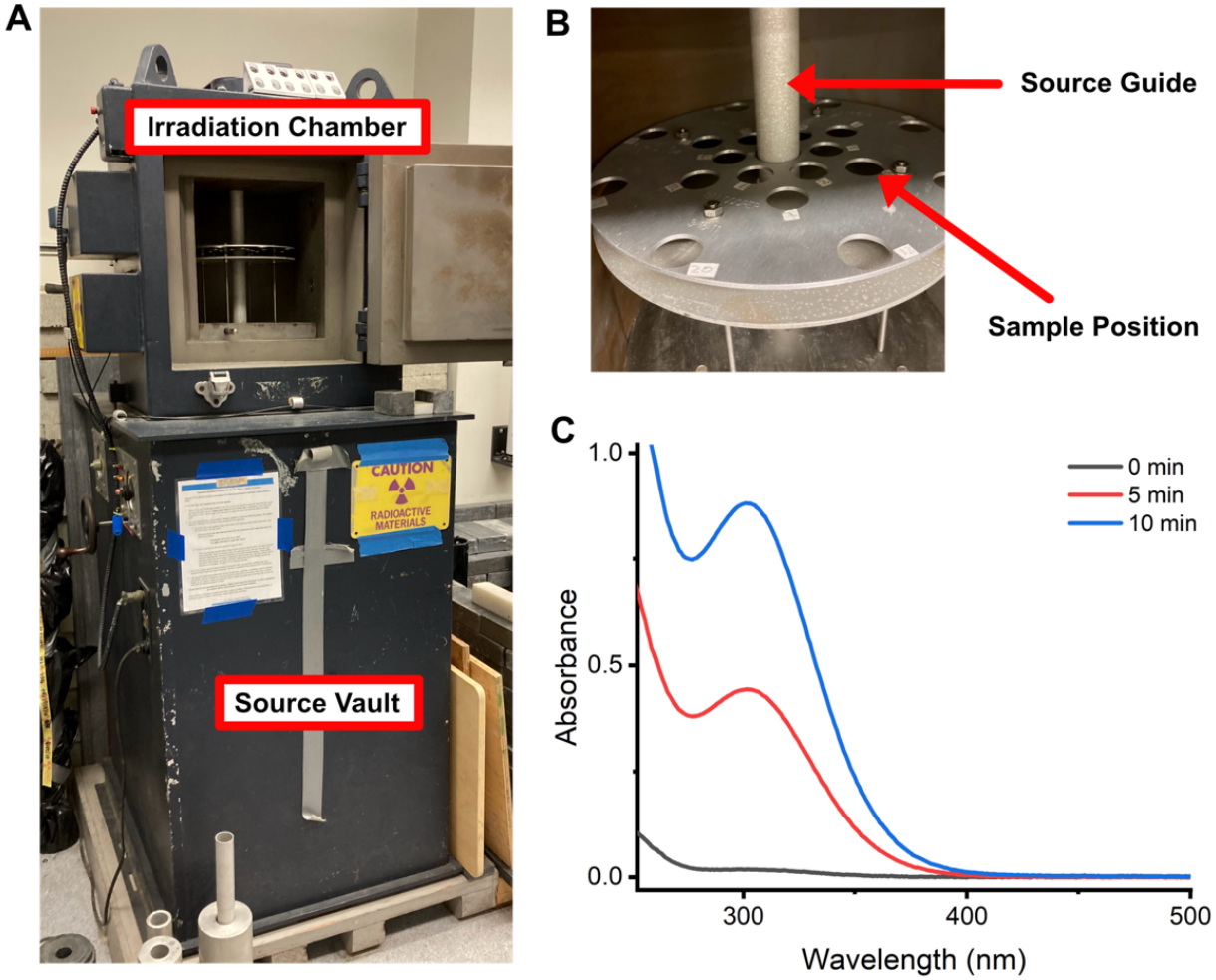

Figure B.1: (A) ^{137}Cs Irradiator Mark-I. The ^{137}Cs is raised into the source guide rod during irradiation. (B) The samples were held in the sample ring at a set distance from the source. (C) Fricke dosimetry was used to confirm the dose for our sample setup. The Fricke solution was irradiated for 5 and 10 minutes and the absorbance at 304 nm was measured as 0.442 after 5 minutes and 0.878 after 10 minutes. The calculated dose rate was 1.54 kGy/hr.

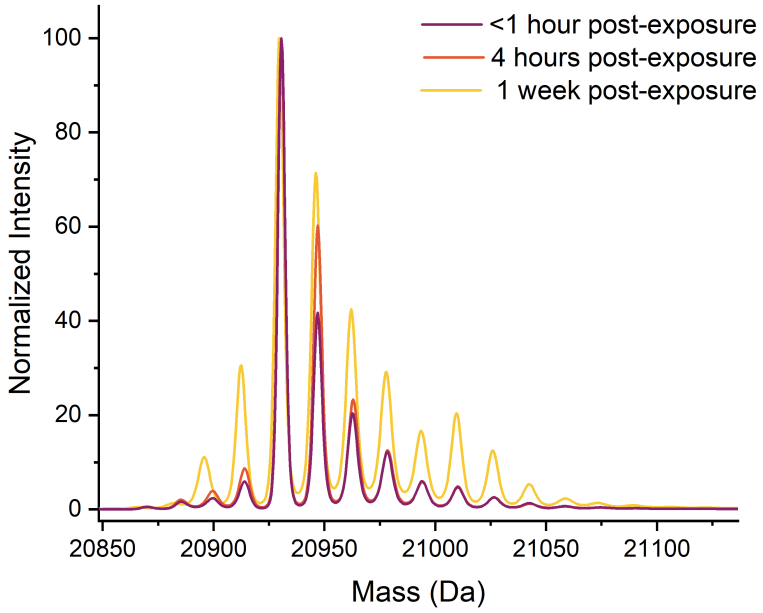

Figure B.2: Deconvoluted intact mass spectra of HγS irradiated for 1 hr/1.5 kGy immediately after removal from the source (purple), 4 hours after removal from the source (orange) and 1 week after removal from the source (yellow). These data indicate that HγS continues to be modified post-exposure.

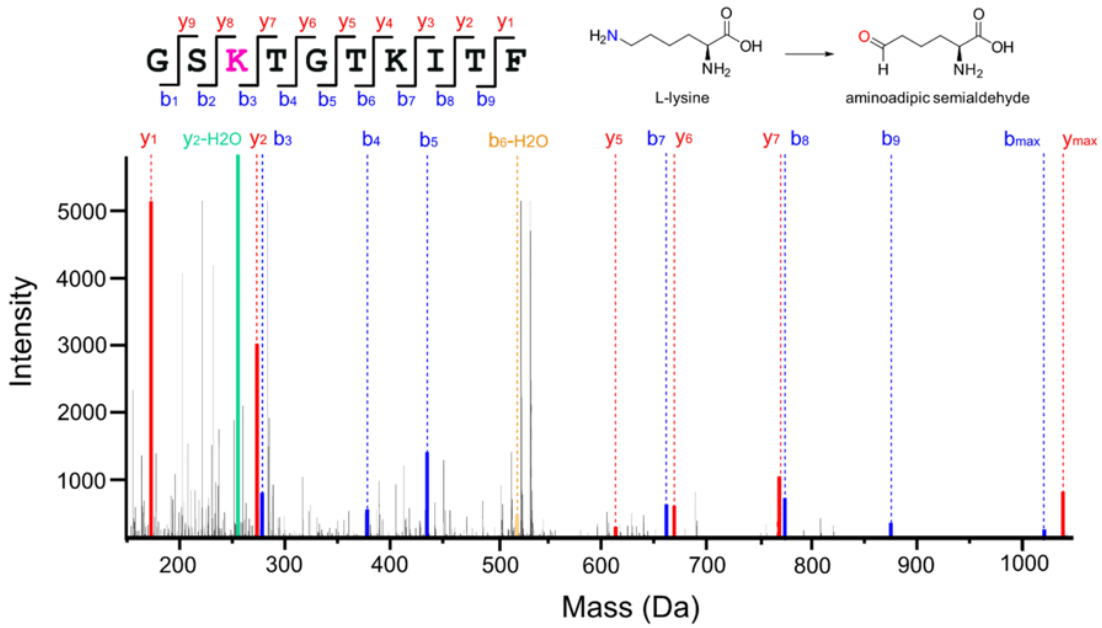

Assignment	Mass (Da)	Intensity (counts)	Modifiers
y1	166.08	5052	
y2-H2O	249.16	21340	
y2	267.13	3224	
b3	272.14	846	Oxidation K (1)
b4	373.17	481	Oxidation K (1)
b5	430.23	1523	Oxidation K (1)
b6-H2O	513.21	297	Oxidation K (1)
y5	609.36	164	
b7	659.34	654	Oxidation K (1)
y6	666.41	651	
y7	767.45	1147	
b8	772.44	741	Oxidation K (1)
b9	873.51	362	Oxidation K (1)

Figure B.3: Tandem mass spectrum and peak list for the pepsin digest peptide 1-GSKTGTKITF-10. The b3 ion and subsequent b ions show a -1 Da loss on one of the first three residues. Oxidation of lysine results in a -1 Da loss in the conversion to the aldehyde derivative, suggesting this peptide resulted from an oxidation of K3.

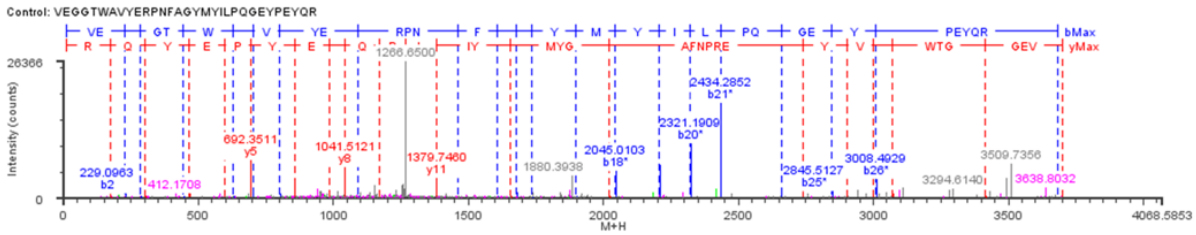

Assignment	Mass (Da)	Intensity (counts)	Modifiers	Assignment	Mass (Da)	Intensity (counts)	Modifiers
y1	175.0959	259		y11-H2O	1361.718	507	
a2	201.1006	787		y11	1379.746	3853	
b2	229.0963	831		b13	1459.5951	160	
a3	258.1041	108		a14	1578.8434	474	
b3	286.1269	219		b14	1606.8911	486	
y2	303.1582	219		y13	1655.9369	312	
b5	444.197	203		b15	1677.8593	1116	
y3	466.2321	943		b16	1734.9816	260	
y4	595.2849	488		a17	1870.0011	270	
a6	602.2539	146		b17	1898.0344	354	
b6	630.2852	266		y16*	2023.0513	223	Oxidation M (1)
a7	673.3377	323		b18*	2045.0103	5182	Oxidation M (1)
y5	692.3511	7252		a19*	2180.1023	1169	Oxidation M (1)
b7	701.3341	896		b19*	2208.0957	6344	Oxidation M (1)
b8	800.4171	934		b20*	2321.1909	10556	Oxidation M (1)
y6-NH3	838.412	162		b21*-H2O	2416.2446	1825	Oxidation M (1)
y6	855.4312	3544		b21*	2434.2852	18326	Oxidation M (1)
y7-H2O	966.4432	772		b23*	2659.4243	1141	Oxidation M (1)
y7	984.4826	1396		y22*	2737.4307	521	Oxidation M (1)
y8	1041.5121	5972		b25*	2845.5127	1316	Oxidation M (1)
b10-NH3	1075.5303	469		y23*	2900.5312	1408	Oxidation M (1)
b10	1092.5646	499		y24*	2999.5962	712	Oxidation M (1)
y9	1169.5917	1210		b26*	3008.4929	3712	Oxidation M (1)
a11	1220.6372	605		y25*	3070.6343	832	Oxidation M (1)
y10-NH3	1249.5657	645		y28*	3414.356	202	Oxidation M (1)
y10	1266.5886	16750					

Figure B.4: Tandem mass spectrum and peak list for the trypsin digest peptide 42-VEGGTWAVYERPNFAGYMYILPQGEYPEYQR-72. The lack of mass change on the b17 ion and the addition of +16 Da to the b18 ion and subsequent b ions demonstrates oxidation of M59.

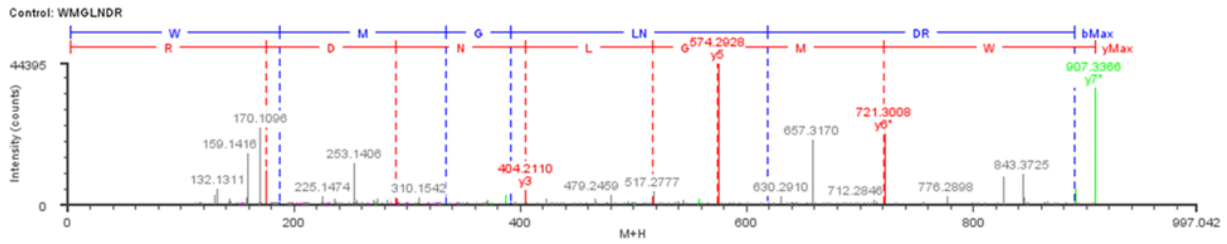

Assignment	Mass (Da)	Intensity (counts)	Modifiers
y1-H2O	157.1165	161	
y1-NH3	158.1063	509	
b1-H2O	169.1132	263	
y1	175.1681	10688	
b1	187.1351	370	
y2-H2O	272.1727	285	
y2	290.1894	1759	
a2*	306.159	154	Oxidation M (1)
b2*-NH3	317.132	644	Oxidation M (1)
b2*	334.1506	1936	Oxidation M (1)
a3*	363.1932	135	Oxidation M (1)
b3*-H2O	373.1554	181	Oxidation M (1)
b3*-NH3	374.1442	440	Oxidation M (1)
y3-H2O	386.2054	148	
y3-NH3	387.1898	3147	
b3*	391.1672	517	Oxidation M (1)
y3	404.211	4463	
a4*	476.2625	112	Oxidation M (1)
y4-NH3	500.2557	555	
y4	517.1648	361	
y5-H2O	556.2769	391	
y5-NH3	557.2661	1780	
y5	574.2928	44395	
b5*	618.2497	157	Oxidation M (1)
y6*-H2O	703.293	835	Oxidation M (1)
a6*	705.268	153	Oxidation M (1)
y6*	721.3008	22470	Oxidation M (1)
y7*-H2O	889.3745	135	Oxidation M (1)
y7*-NH3	890.4197	4937	Oxidation M (1)
y7*	907.3366	36780	Oxidation M (1)

Figure B.5: Tandem mass spectrum and peak list for the trypsin digest peptide 73-WMGLNDR-79. The lack of mass change on the y5 ion and the addition of +16 Da to the y6 ion and subsequent y ions, as well as lack of mass change on b1 and addition of +16 Da to the b2 ion and subsequent b ions demonstrates oxidation of M74.

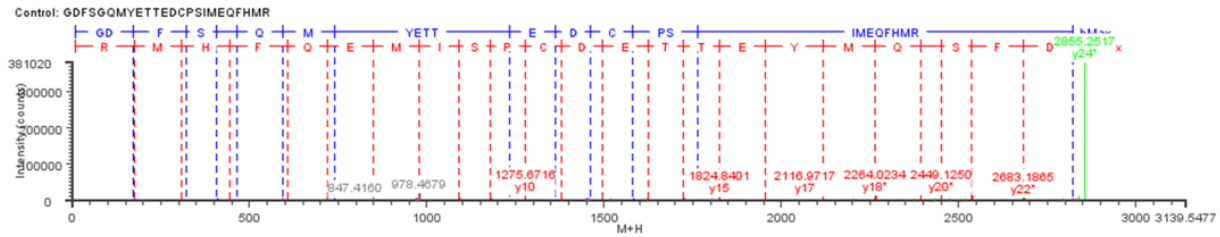

Assignment	Mass (Da)	Intensity (counts)	Modifiers	Assignment	Mass (Da)	Intensity (counts)	Modifiers
y1-H2O	157.1475	190		y6	847.6084	113	
b2	173.1071	197		a8*	874.3091	126	Oxidation M (1)
y1	175.1685	621		b8*	902.5993	304	Oxidation M (1)
a3	292.1702	205		y7	978.6574	171	
y2	306.1979	1088		b9-NH3	998.5712	154	
b3	320.1623	693		b9	1015.2303	173	
a4	379.1808	209		y8	1091.4393	901	
b4-H2O	389.1756	723		b10*	1132.2902	1413	Oxidation M (1)
b4	407.1785	1020		y9	1178.4476	743	
y3	443.2347	1150		b11*	1233.3702	304	Oxidation M (1)
b5-H2O	446.1916	206		y10	1275.5873	2134	
b5-NH3	447.1919	197		y11	1378.3569	254	
b5	464.203	237		y12	1493.3458	479	
b6-H2O	574.2232	221		y14	1723.6437	666	
b6-NH3	575.2215	378		y15	1824.5723	1109	
y4	590.2869	1464		y16	1953.7211	843	
b6	592.235	645		y17	2116.7334	2223	
y5-NH3	701.2923	410		y18*	2263.7605	824	Oxidation M (1)
y5	718.2914	1389		y20*	2449.6069	847	Oxidation M (1)
b7*-H2O	721.2454	224	Oxidation M (1)	y21*	2536.7844	631	Oxidation M (1)
b7*	739.2623	304	Oxidation M (1)	y24*-H2O	2836.8862	3208	Oxidation M (1)
y6-H2O	829.328	409		y24*	2854.9028	62097	Oxidation M (1)

Figure B.6: Tandem mass spectrum and peak list for the trypsin digest peptide 102-GDFSGQMYETTEDCPSIMEQFHMR-125. The lack of mass change on the y17 ion and the addition of +16 Da to the y18 ion and subsequent y ions, as well as lack of mass change on the b6 ion and the addition of +16 Da to the b7 ion and subsequent b ions demonstrates oxidation of M108.

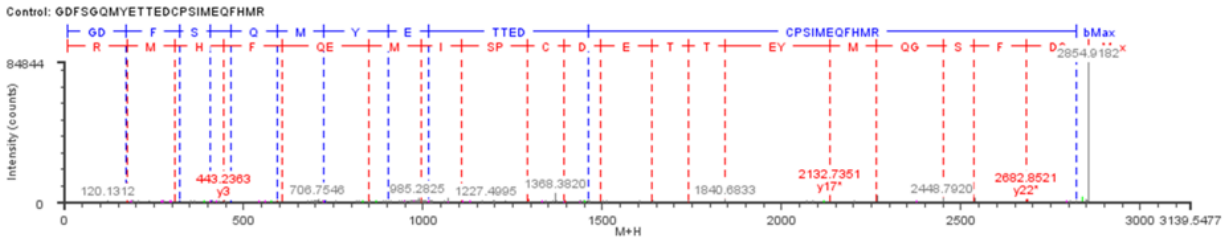

Assignment	Mass (Da)	Intensity (counts)	Modifiers	Assignment	Mass (Da)	Intensity (counts)	Modifiers
y1-H2O	157.148	181		b9-H2O	997.2227	332	
b2	173.1058	283		a9*	1003.5489	478	Oxidation M (1)
y1	175.1667	789		b9	1015.3193	353	
y2-H2O	288.1487	174		y8*	1107.4937	322	Oxidation M (1)
y2-NH3	289.1779	120		a11*	1205.4117	135	Oxidation M (1)
a3	292.1692	300		y10*	1291.5879	2083	Oxidation M (1)
b3-H2O	302.1481	208		y11*	1394.5739	922	Oxidation M (1)
y2	306.1983	1310		a13*	1449.9229	923	Oxidation M (1)
b3	320.1605	1214		b13	1461.7791	163	
a4	379.1925	245		b13*	1477.2343	249	Oxidation M (1)
b4-H2O	389.1752	927		y12	1493.8676	227	
b4	407.1804	1533		y12*	1509.4847	275	Oxidation M (1)
a5	436.2003	178		y13*	1638.4642	107	Oxidation M (1)
y3	443.2363	1537		y14*	1739.5192	1095	Oxidation M (1)
b5	464.1914	682		y15*	1840.5464	1483	Oxidation M (1)
a6	564.1924	114		y17*-H2O	2114.7209	551	Oxidation M (1)
y4-NH3	573.2664	189		y17*	2132.7351	4672	Oxidation M (1)
b6-H2O	574.2233	1063		y18*-H2O	2245.6943	247	Oxidation M (1)
y4	590.2895	1447		y18*	2263.5925	3580	Oxidation M (1)
b6	592.222	1222		y19*			
b7	723.2507	910		y20*-NH3	2432.6448	291	Oxidation M (1)
y6-H2O	829.2997	483		y20*	2449.6072	1860	Oxidation M (1)
y6	847.3151	1870		y21*-H2O	2518.5969	186	Oxidation M (1)
b8-H2O	868.2592	483		y21*	2535.6409	1676	Oxidation M (1)
b8-NH3	869.3275	143		y22*	2682.8521	2043	Oxidation M (1)
b8	886.3123	339		y24*-H2O	2836.9375	3376	Oxidation M (1)
y7*	994.3598	987	Oxidation M (1)	y24*	2854.6646	7479	Oxidation M (1)

Figure B.7: Tandem mass spectrum and peak list for the trypsin digest peptide 102-GDFSGQMYETTEDCPSIMEQFHMR-125. The lack of mass change on the y6 ion and the addition of +16 Da to the y7 ion and subsequent y ions demonstrates oxidation of M119.

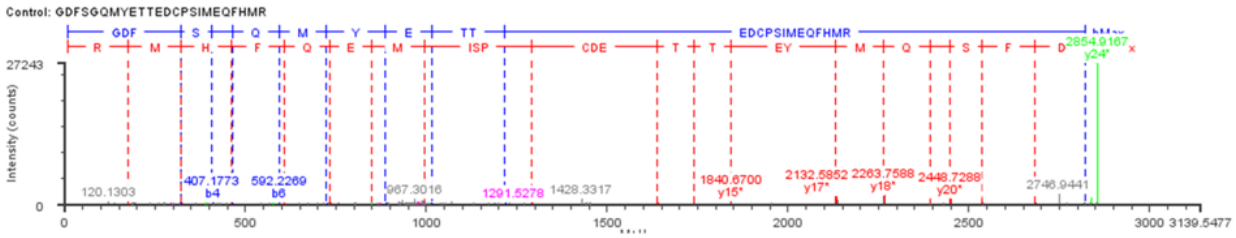

Assignment	Mass (Da)	Intensity (counts)	Modifiers
y1	175.1654	329	
b3	320.1557	278	
y2*	322.1915	122	Oxidation M (1)
b4-H2O	389.1705	297	
b4	407.1773	475	
y3*	459.2289	232	Oxidation M (1)
b5	464.1888	126	
b6-H2O	574.2421	177	
b6-NH3	575.219	329	
b6	592.2269	448	
y4*	606.2795	242	Oxidation M (1)
b7	723.2176	256	
y5*	734.2537	188	Oxidation M (1)
y6*-NH3	846.2582	223	Oxidation M (1)
y6*	863.2909	207	Oxidation M (1)
b8	886.3071	162	
y7*	994.3729	214	Oxidation M (1)
b9-H2O	997.3035	194	
b9	1015.2784	279	
b11	1217.3018	219	
y10*	1291.4392	176	Oxidation M (1)
y13*	1638.5977	268	Oxidation M (1)
y14*	1739.5386	479	Oxidation M (1)
y15*	1840.67	619	Oxidation M (1)
y17*	2132.5852	1728	Oxidation M (1)
y18*	2263.7588	1840	Oxidation M (1)
y19*	2391.7827	615	Oxidation M (1)
y20*	2448.7288	1236	Oxidation M (1)
y21*	2535.8076	474	Oxidation M (1)
y22*	2683.0017	558	Oxidation M (1)
y24*-H2O	2836.7964	1315	Oxidation M (1)
y24*	2854.9167	27243	Oxidation M (1)

Figure B.8: Tandem mass spectrum and peak list for the trypsin digest peptide 102-GDFSGQMYETTEDCPSIMEQFHMR-125. The lack of mass change on the y1 ion and the addition of +16 Da to the y2 ion and subsequent y ions demonstrates oxidation of M124.

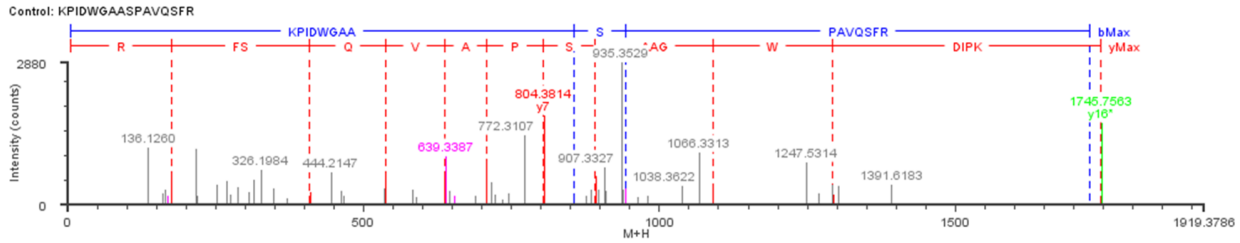

Assignment	Mass (Da)	Intensity (counts)	Modifiers
y1	175.1682	550	
y3	409.238	244	
y4	537.2903	646	
y5	636.3266	657	
y6	707.3299	850	
y7	804.3814	1814	
b8*	855.4062	208	Hydroxyl W (1)
y8	891.4169	587	
b9*	942.3573	310	Hydroxyl W (1)
y11	1090.4874	365	
y12*	1292.4341	209	Hydroxyl W (1)
y16*	1745.7563	1664	Hydroxyl W (1)

Figure B.9: Tandem mass spectrum and peak list for the trypsin digest peptide 159-KPIDWGAASPAVQSFR-174. The lack of mass change on the y11 ion and the addition of +16 Da to the y12 ion and subsequent y ions demonstrates oxidation of W163.

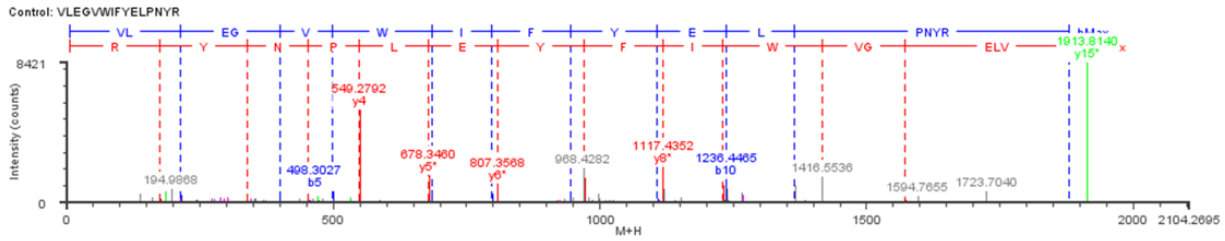

Assignment	Mass (Da)	Intensity (counts)	Modifiers
y1	175.1661	229	
a2	185.2138	667	
b2	213.2073	442	
y2	338.2161	238	
a4	371.2521	147	
b4	399.253	457	
y3	452.242	164	
a5	470.3103	380	
b5	498.3027	658	
y4-NH3	532.258	262	
y4	549.2792	5576	
y5*	678.346	1644	Oxidation L (1)
b6	684.348	705	
b7	797.4233	499	
y6*	807.3568	1127	Oxidation L (1)
b8	944.407	495	
y7*	970.3701	1461	Oxidation L (1)
b9	1107.4791	227	
y8*	1117.4352	2122	Oxidation L (1)
y9*	1230.5137	1042	Oxidation L (1)
b10	1236.4465	1367	
b11*	1365.4825	793	Oxidation L (1)
y10*	1416.4567	1164	Oxidation L (1)
y12*	1572.5155	126	Oxidation L (1)
y15*	1913.814	8421	Oxidation L (1)

Figure B.10: Tandem mass spectrum and peak list for the trypsin digest peptide 132-VLEGVWIFYELPNYR-146. The lack of mass change on the y4 ion and the addition of +16 Da to the y5 ion and subsequent y ions demonstrates oxidation of L142 .

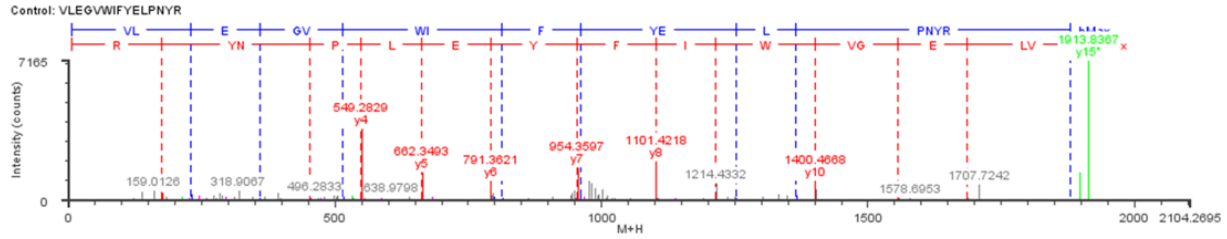

Assignment	Mass (Da)	Intensity (counts)	Modifiers
y1	175.1667	355	
b2*-H2O	211.1922	153	Oxidation L (1)
b2*-NH3	212.1445	167	Oxidation L (1)
b2*	229.1992	318	Oxidation L (1)
b3*	358.2214	100	Oxidation L (1)
y3	452.2447	174	
b5*	514.2862	165	Oxidation L (1)
y4-NH3	532.2471	259	
y4	549.2829	3677	
y5	662.3493	1447	
y6	791.3621	995	
b7	797.4	188	
b7*	813.4266	128	Oxidation L (1)
b8*-H2O	942.4509	188	Oxidation L (1)
y7	954.3597	1693	
b8*	960.3894	193	Oxidation L (1)
y8	1101.4218	1982	
y9	1214.5216	649	
b10*	1252.4352	130	Oxidation L (1)
b11*-H2O	1347.5851	151	Oxidation L (1)
b11*	1365.5822	276	Oxidation L (1)
y10	1400.4668	1003	
y12	1556.4976	104	
y13	1685.7007	414	
y15*-H2O	1895.8267	1405	Oxidation L (1)
y15*	1913.8367	7165	Oxidation L (1)

Figure B.11: Tandem mass spectrum and peak list for the trypsin digest peptide 132-VLEGVWIFYELPNYR-146. The +16 Da to the b2 ion and subsequent b ions as well as the lack of mass change on the y13 ion and the addition of +16 Da to the y15 ion suggests oxidation of one of the first two residues, V132 or L133.

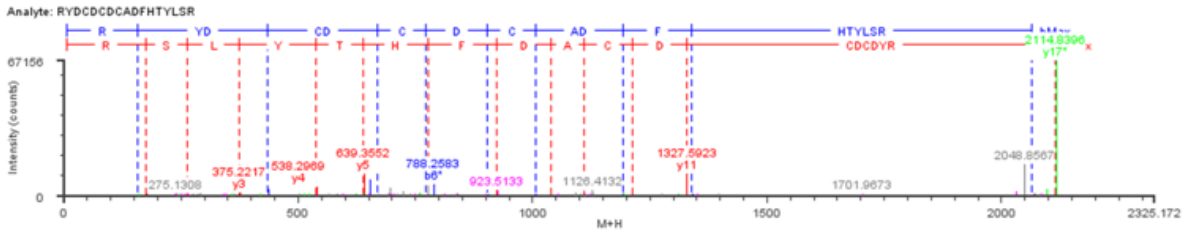

Assignment	Mass (Da)	Intensity (counts)	Modifiers
b1	157.0848	103	
y1-NH3	158.0684	177	
y1	175.0946	836	
y2-NH3	245.1042	448	
y2	262.1321	561	
a2	292.1598	270	
b2-H2O	301.8922	261	
b2-NH3	303.1271	139	
b2	320.1538	379	
y3-NH3	358.1931	264	
y3	375.2232	946	
b3-NH3	418.159	343	
b3	435.1883	1843	
y4-NH3	521.1841	147	
y4	538.298	2358	
y5-H2O	621.3363	605	
b5-H2O	635.2336	137	
b5-NH3	636.2181	621	
y5	639.3536	6649	
b5	653.2436	3430	
y6-H2O	758.421	249	
y6	776.3777	1156	
b6*	788.2567	2903	Oxidation x2 C (1)
b7*	903.297	181	Oxidation x2 C (1)
y7-H2O	905.4447	613	
y7	923.4589	1445	
y8	1038.4944	794	
y9-H2O	1091.4211	267	
y9	1109.5372	1088	
b10*	1192.3947	709	Oxidation x2 C (1)
y10-H2O	1194.543	174	
y10	1212.552	984	
y11	1327.5912	5136	
b11*	1339.4871	386	Oxidation x2 C (1)
y17*-H2O	2096.8257	1878	Oxidation x2 C (1)
y17*	2114.8364	34572	Oxidation x2 C (1)

Figure B.12: Tandem mass spectrum and peak list for the trypsin digest peptide 20-RYDCDCDCADFHTYLSR-36. The lack of mass change on the b5 ion and the addition of +32 Da to the b6 ion and subsequent b ions demonstrates oxidation of C25.

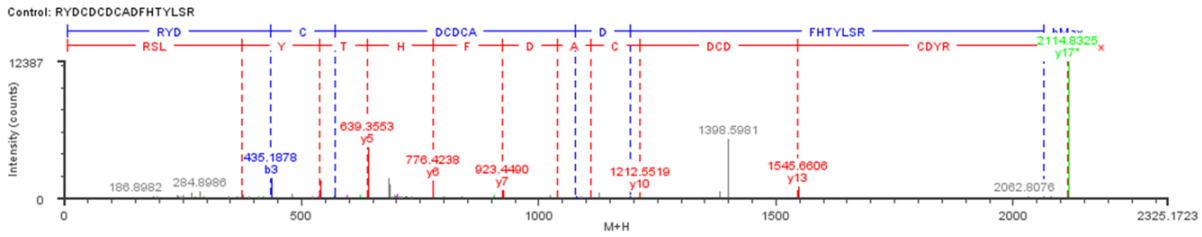

Assignment	Mass (Da)	Intensity (counts)	Modifiers
a2	292.1593	185	
y3	375.2163	305	
b3-NH3	418.1617	228	
b3	435.1878	1809	
y4	538.2961	1567	
b4*	570.1988	1021	Oxidation x2 C (1)
y5-H2O	621.341	375	
y5	639.3553	4632	
y6	776.4238	1632	
y7-H2O	905.4461	315	
y7	923.449	772	
y8	1038.5558	242	
b9*	1077.4355	134	Oxidation x2 C (1)
y9	1109.5822	332	
b10*	1192.3967	213	Oxidation x2 C (1)
y10	1212.5519	578	
y13	1545.6606	1046	
y17*	2114.8325	12387	Oxidation x2 C (1)

Figure B.13: Tandem mass spectrum and peak list for the trypsin digest peptide 20-RYDCDCDCADFHTYLSR-36. The lack of mass change on the b3 ion and the addition of +32 Da to the b4 ion and subsequent b ions demonstrates oxidation of C23.

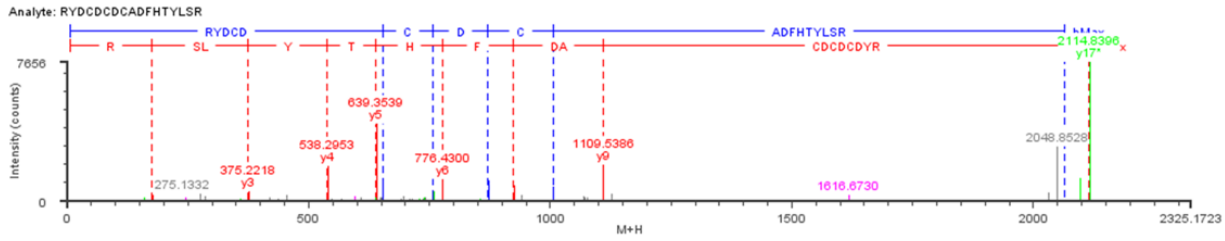

Assignment	Mass (Da)	Intensity (counts)	Modifiers
y1-NH3	158.0683	178	
y1	175.0944	359	
y3-NH3	358.1944	137	
y3	375.2218	547	
y4	538.2953	1935	
b5-NH3	636.2195	212	
y5	639.3539	4230	
b5	653.2458	905	
a6	727.9556	141	
b6-H2O	738.2752	220	
b6	756.2682	242	
y6-H2O	758.3664	507	
y6	776.43	1213	
b7-NH3	854.2782	132	
b7	871.304	1149	
y7	923.4628	835	
b8*	1006.313	801	Oxidation x2 C (1)
y9	1109.5386	1977	
y17*-H2O	2096.8279	1263	Oxidation x2 C (1)
y17*	2114.8396	7656	Oxidation x2 C (1)

Figure B.14: Tandem mass spectrum and peak list for the trypsin digest peptide 20-RYDCDCDCADFHTYLSR-36. The lack of mass change on the b7 ion and the addition of +32 Da to the b8 ion and subsequent b ions demonstrates oxidation of C27.

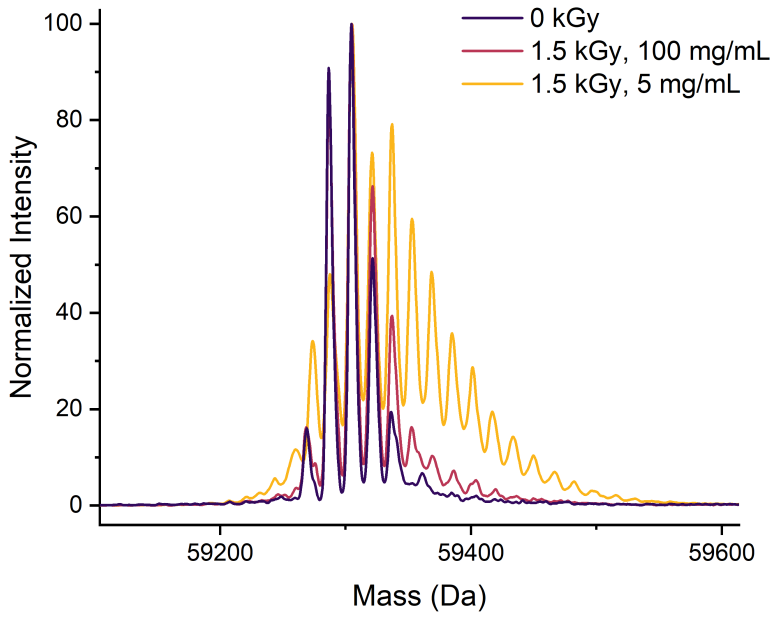

Figure B.15: Comparison of deconvoluted intact mass spectra of lysozyme non-irradiated (purple) and irradiated for 1 hr/1.5 kGy at 100 mg/mL (purple) and 5 mg/mL (yellow). Increased protein concentration appears to reduce the relative amount of modification upon γ irradiation.

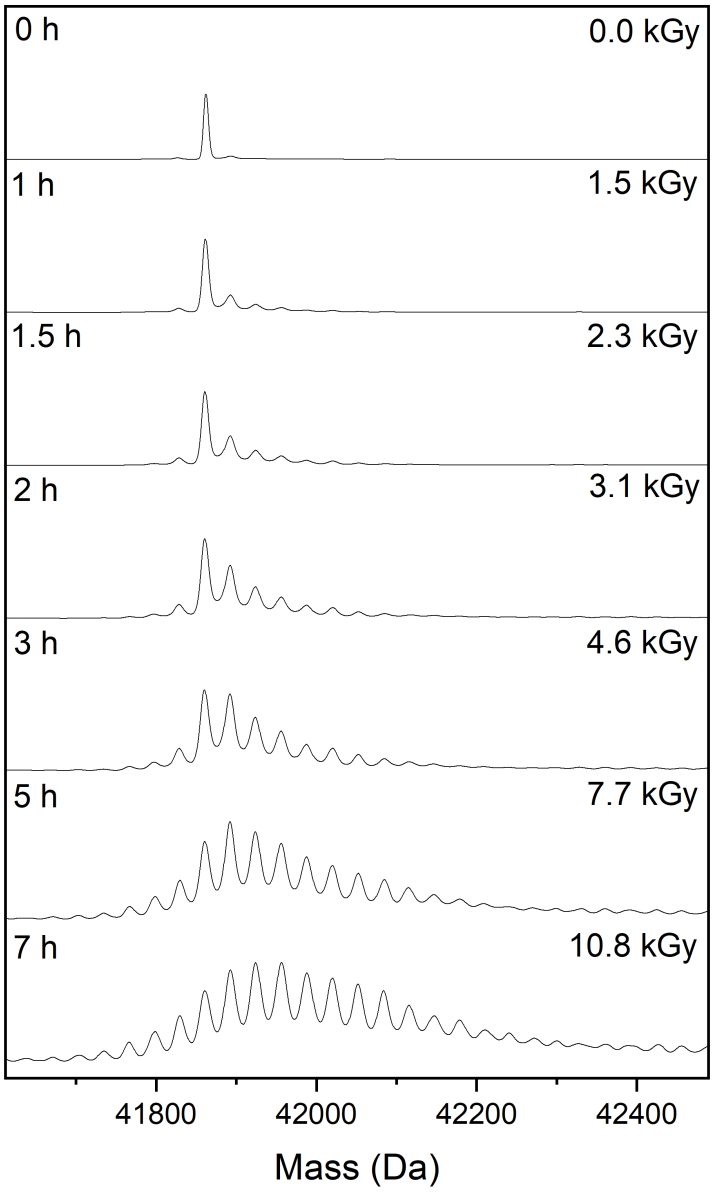

Figure B.16: Evidence of dimerization observed in mass spectra during the course of irradiation. Deconvoluted intact mass spectra of HγS samples irradiated with doses (0, 1.5, 2.3, 3.1, 4.6, 7.7, and 10.8 kGy) of γ radiation show the expected HγS dimer mass.

Appendix C

Supplementary material for *A simple vapor-diffusion method enables protein crystallization inside the HARE serial crystallography chip*

For all supplemental figures:

a)Hit-map: a blue dot on the grey outline of the chip compartments indicates a feature for which one or more protein diffraction pattern(s) could be obtained. For partially collected chips, the missing parts are indicated in yellow.

b) Resolution histogram of the diffraction patterns obtained for each chip.

c) Unit cell parameter histogram of the diffraction patterns obtained for each chip.

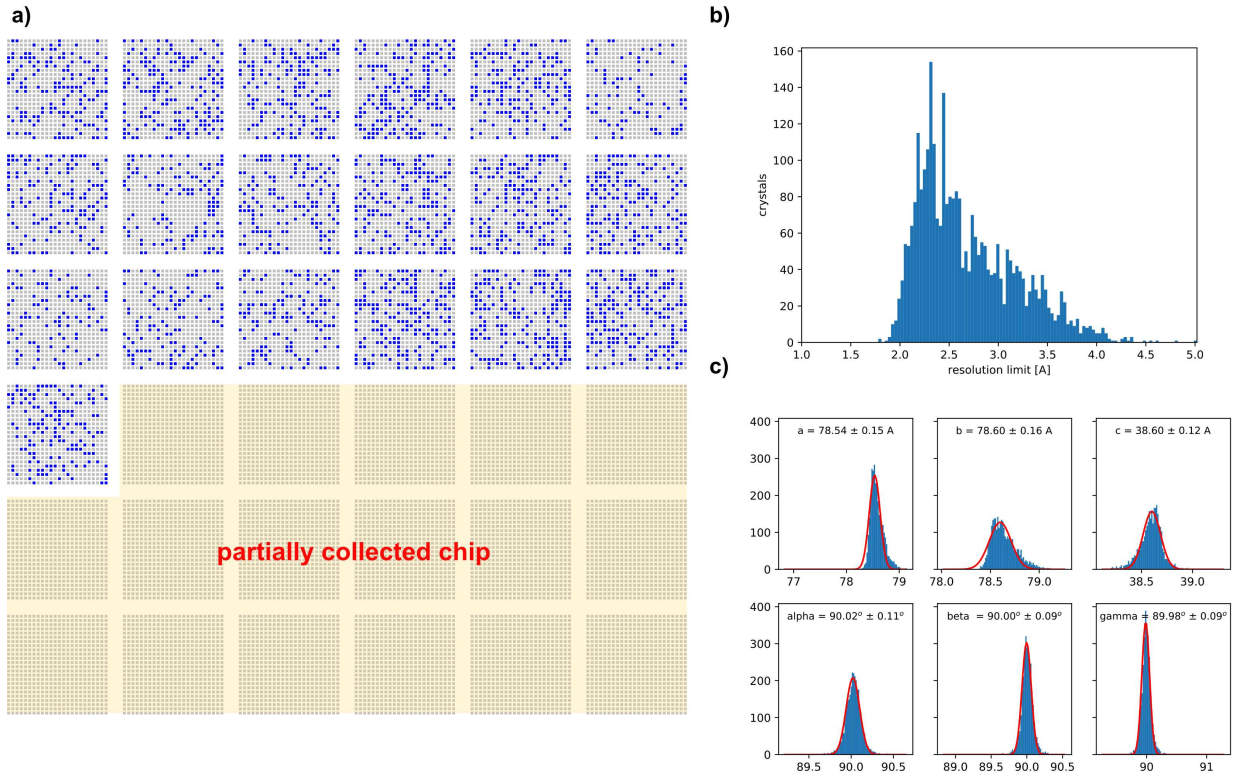

Figure C.1: Lysozyme chip 1.

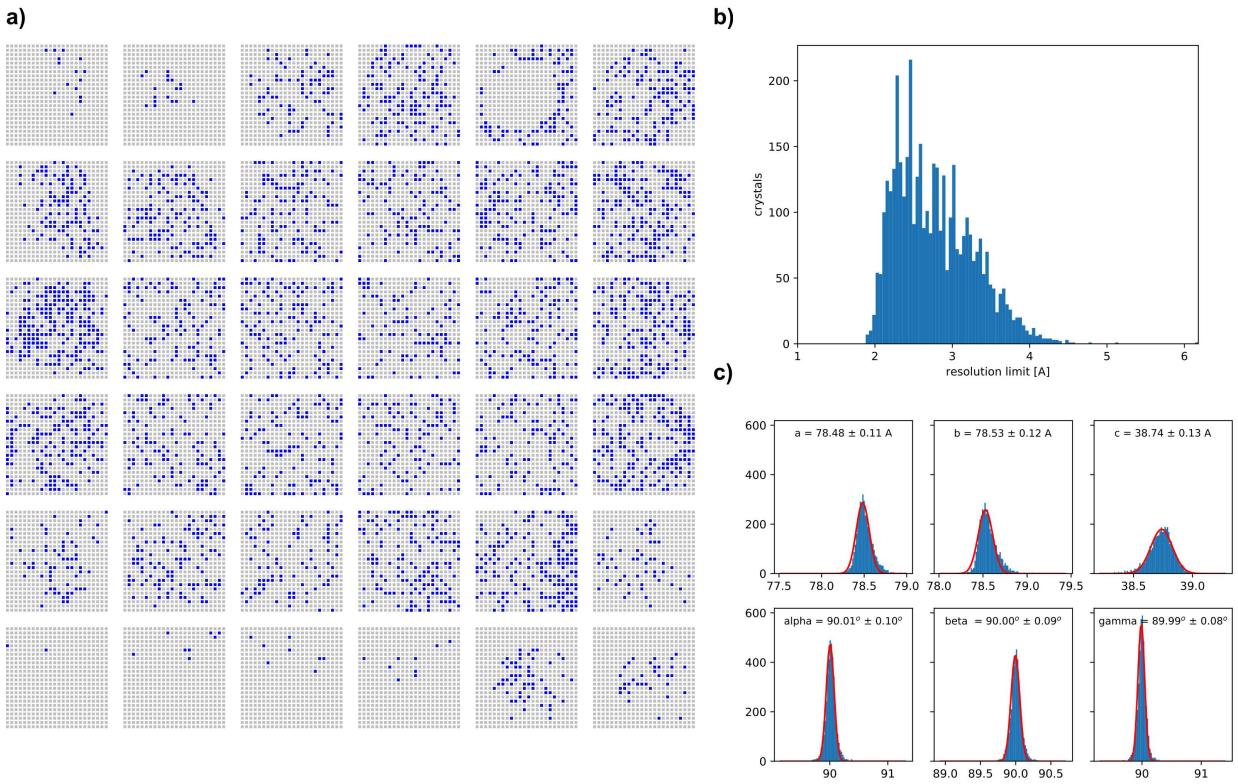

Figure C.2: Lysozyme chip 2.

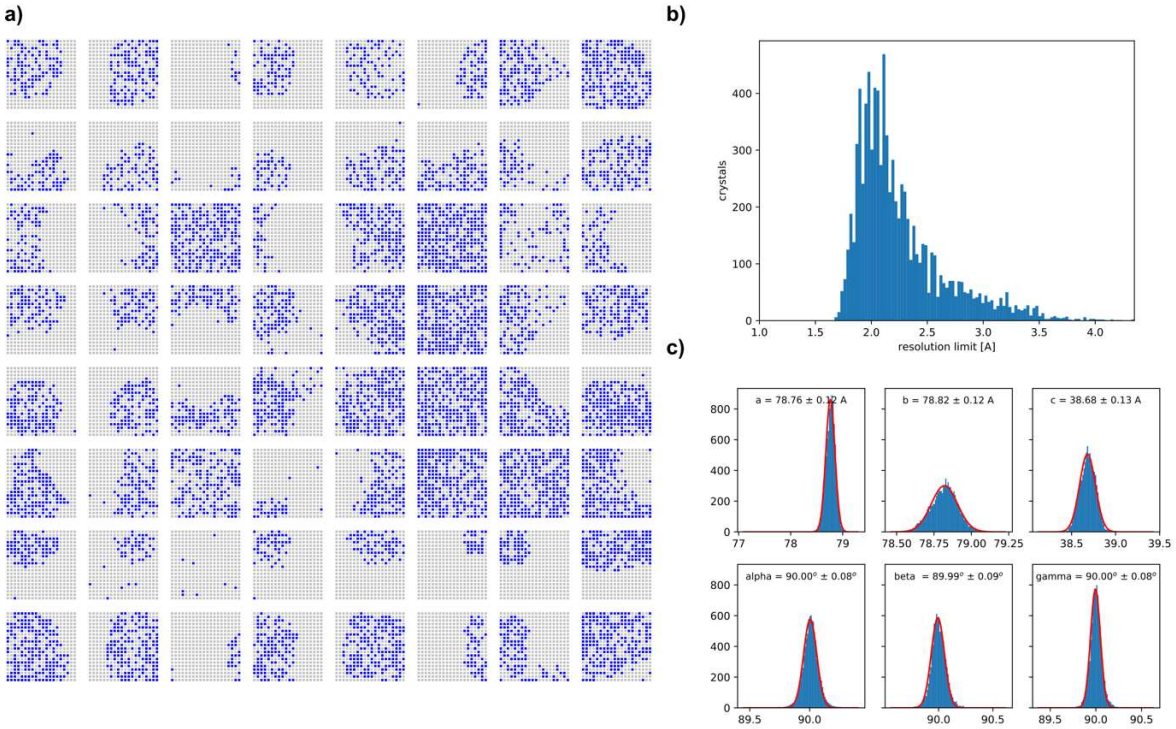

Figure C.3: Lysozyme chip 3.

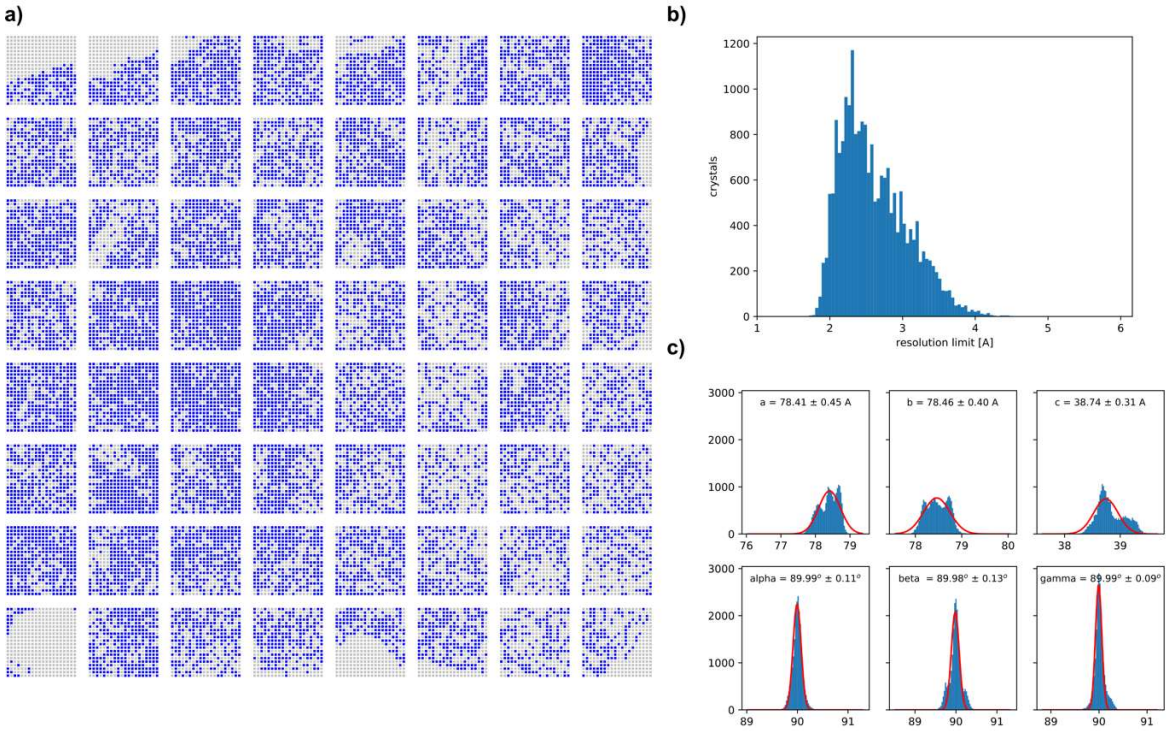

Figure C.4: Lysozyme chip 4.

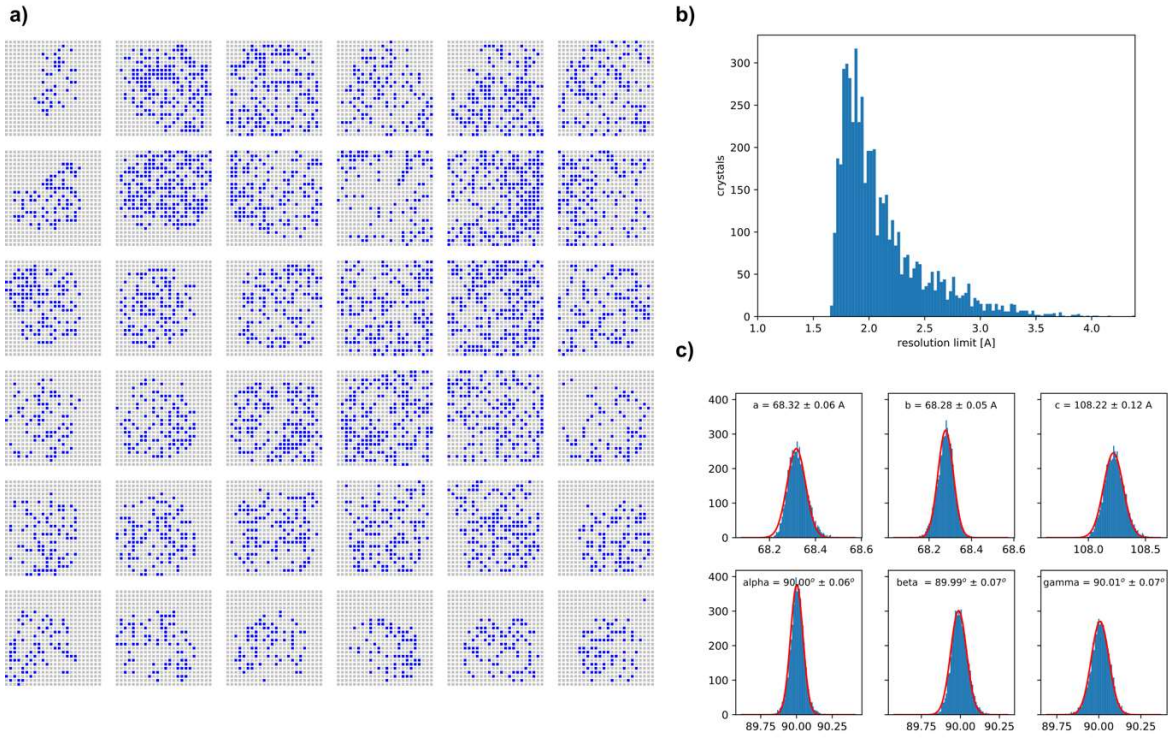

Figure C.5: Proteinase K chip 1.

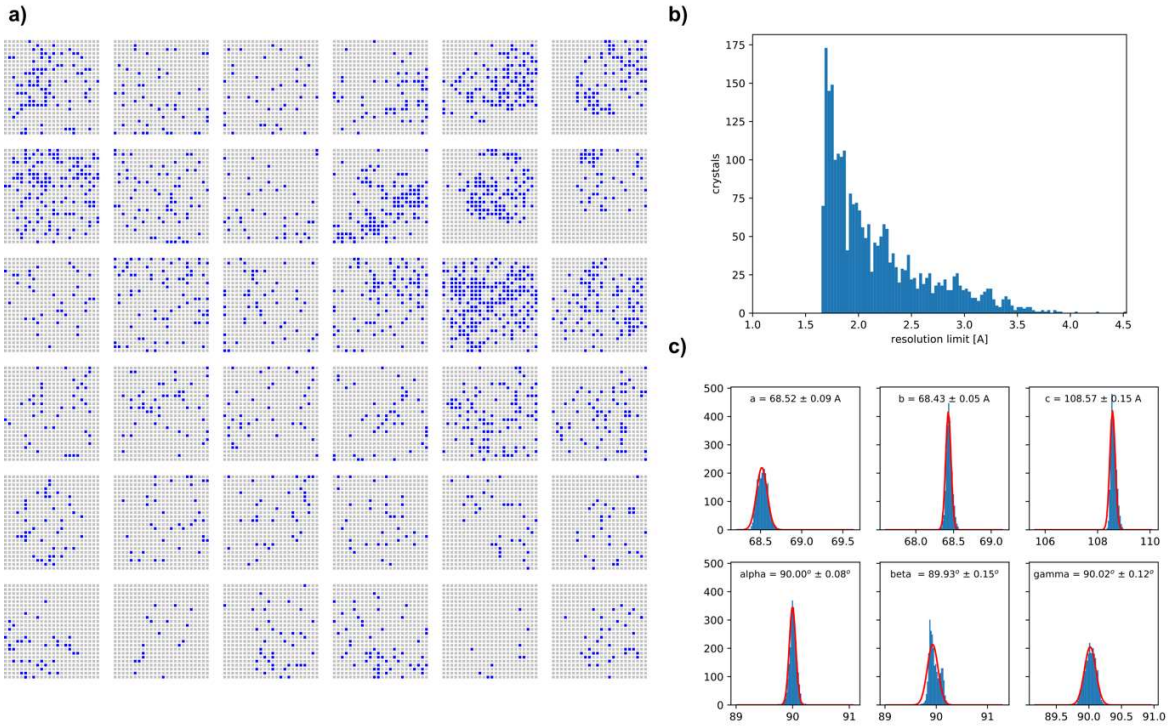

Figure C.6: Proteinase K chip 2.

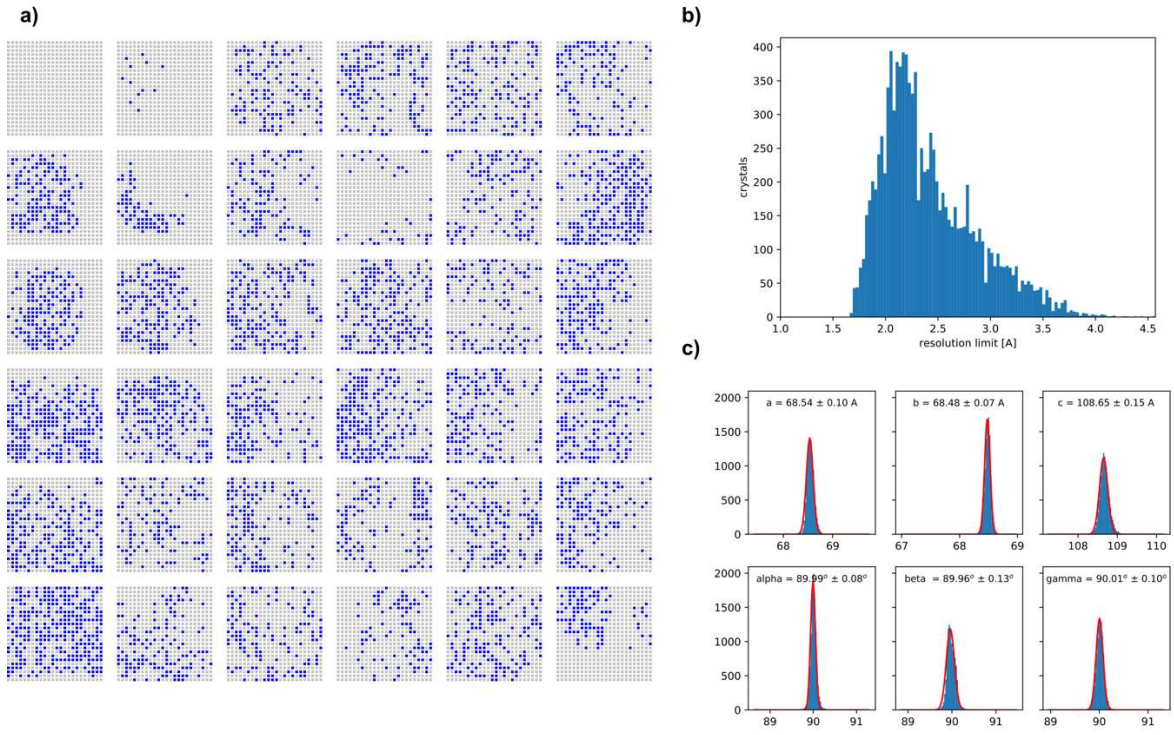

Figure C.7: Proteinase K chip 3.

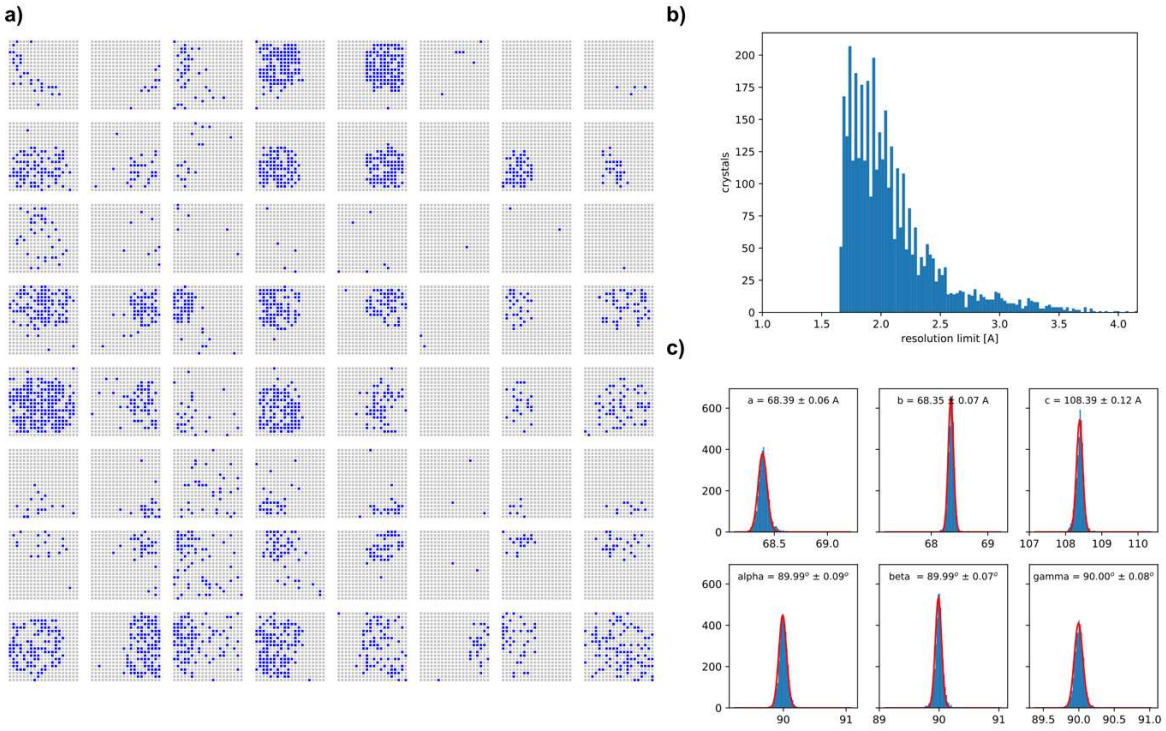

Figure C.8: Proteinase K chip 4.

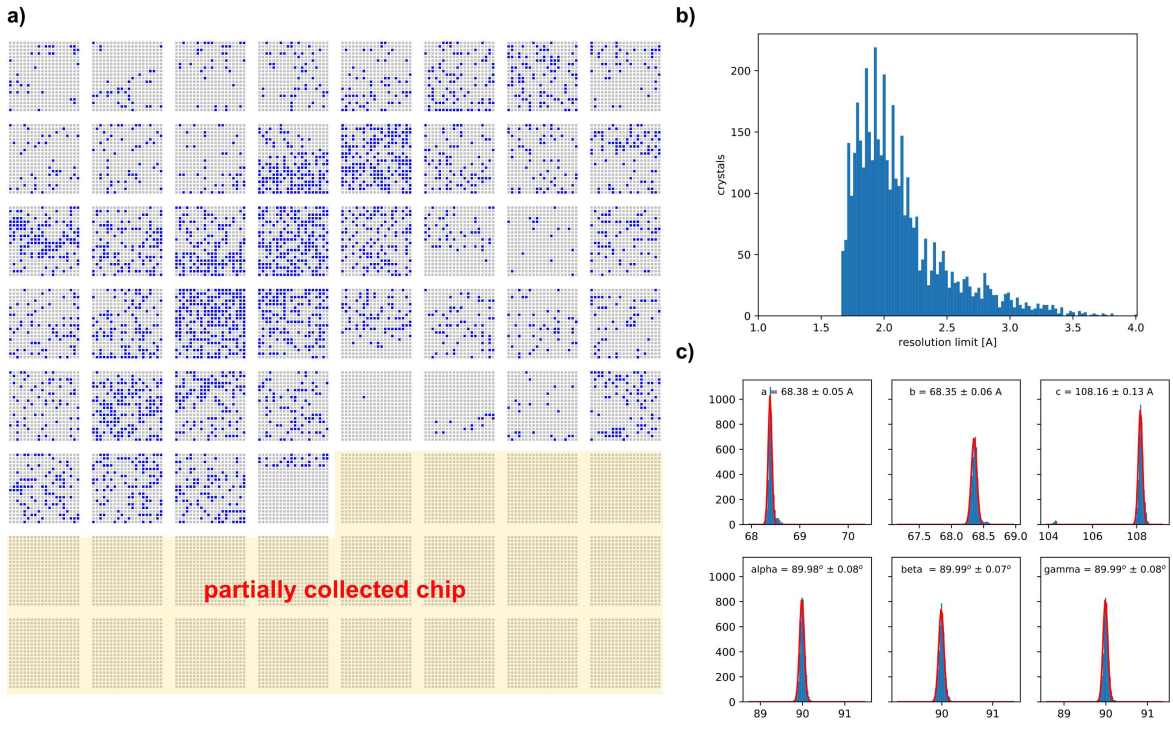

Figure C.9: Proteinase K chip 5.

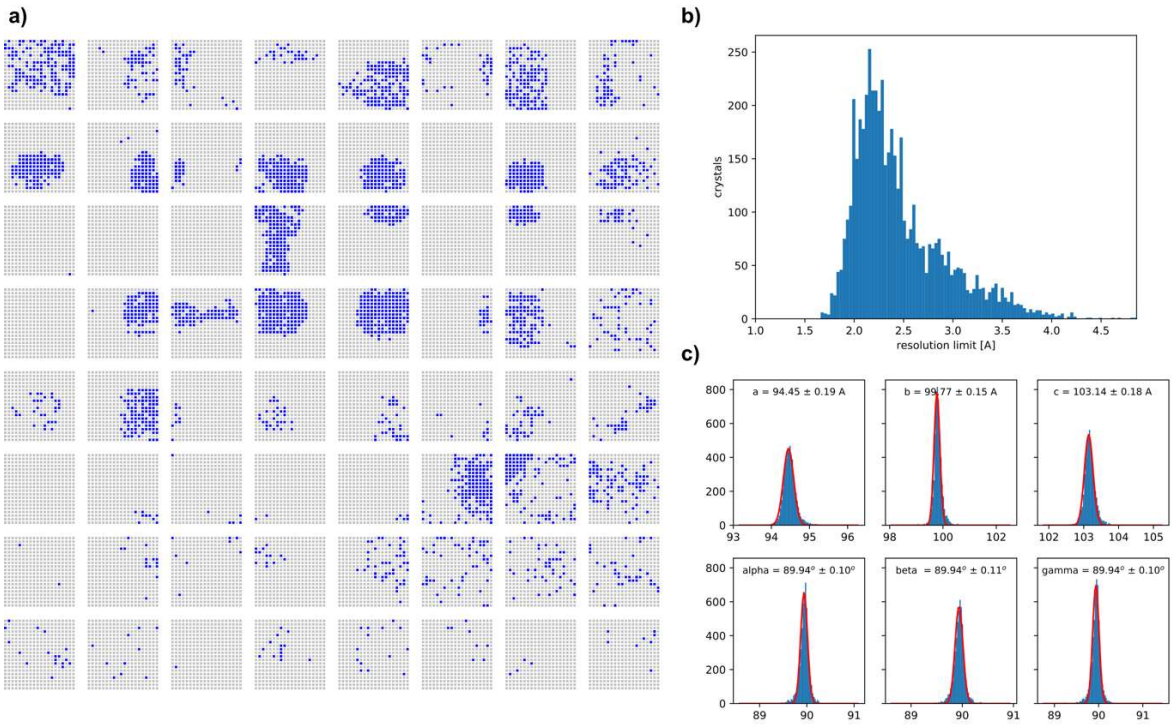

Figure C.10: Xylose isomerase chip 1.

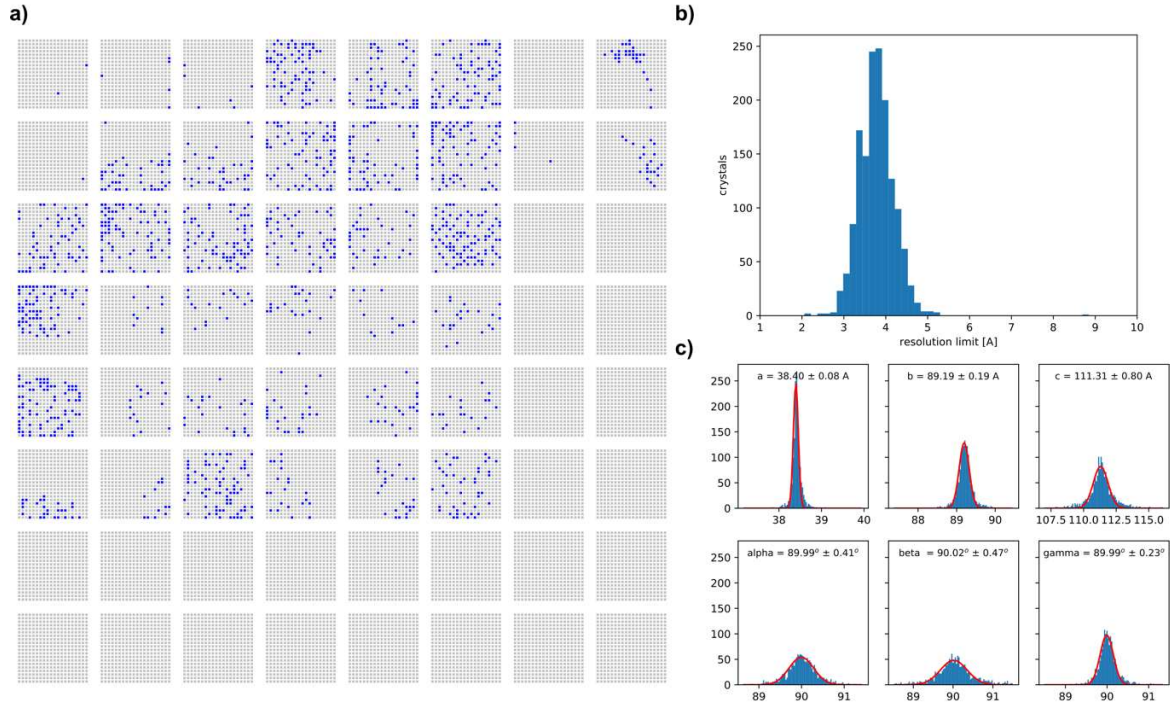

Figure C.11: Human γS-crystallin deamidation mutant chip 1.

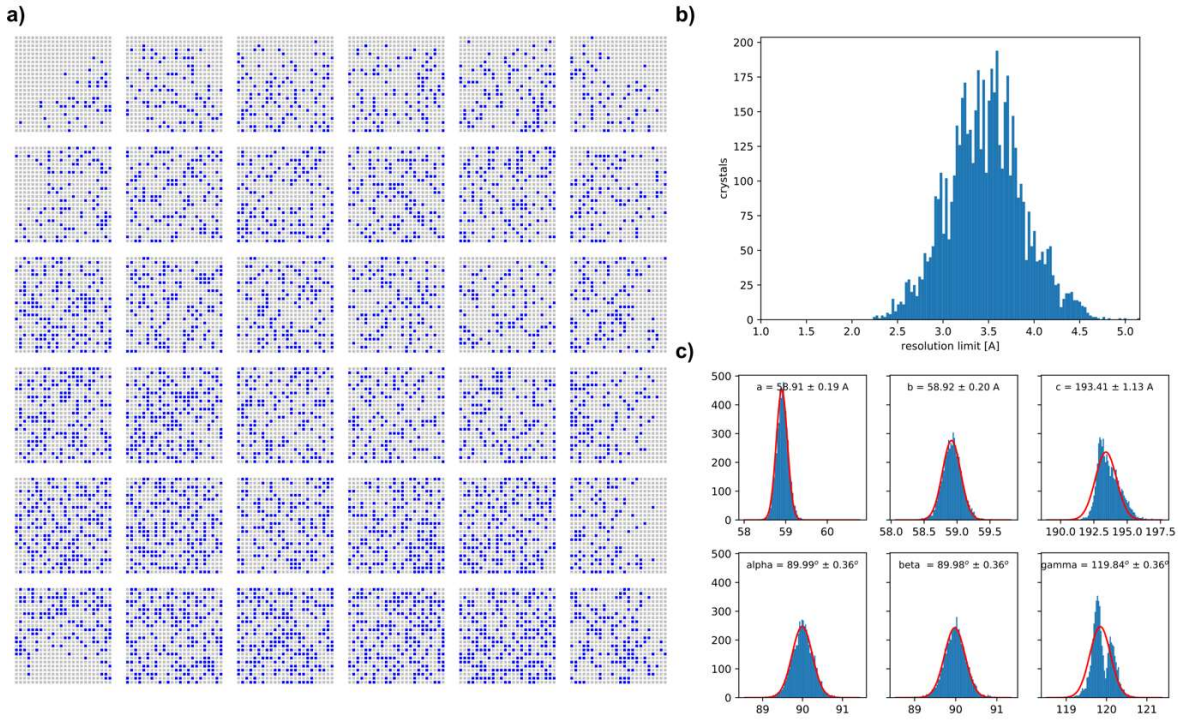

Figure C.12: HEX-1 chip 1, loaded.

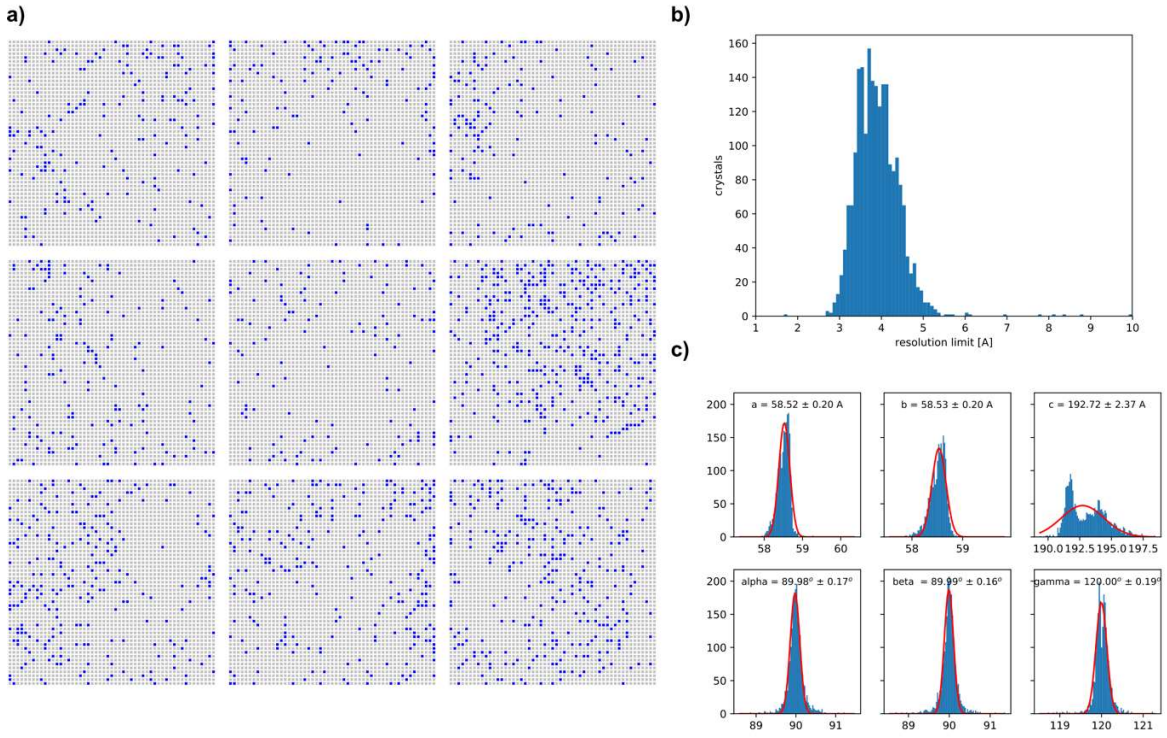

Figure C.13: HEX-1 chip 2, *in situ*.